UZBEKISTAN ACADEMY OF SCIENCES ASTRONOMICAL INSTITUTE

On the right of the manuscript
UDC: 530.12:531.51

SARIKULOV FURKAT SHERALI UGLI

Testing black hole nature in alternative gravity through astrophysical observations

01.03.01 - Astronomy

DISSERTATION OF THE DOCTOR OF PHILOSOPHY (PhD) IN PHYSICS AND MATHEMATICS

Supervisor: **Ahmedov Bobomurat Juraevich**
Doctor of Sciences in Physics and Mathematics, Academician

Tashkent-2026

Contents

Introduction **7**

1 Novel black hole solutions in extended gravity models and photon motion around them **14**
1.1 Novel charged black holes with nonlinear electrodynamics 14
1.1.1 Effective geometry for photon propagation in nonlinear electrodynamics 17
1.2 Four-dimensional Einstein-Gauss-Bonnet black hole surrounded by perfect fluid dark matter 20
1.2.1 Non-rotating black hole 22
1.2.2 Rotating black hole 24
1.2.3 Geodesics and circular photon orbits 29
1.3 Four-dimensional Einstein-Gauss-Bonnet black hole in the Power-Yang-Mills field 33
1.3.1 Static black hole 33
1.3.2 Rotating black hole 38
1.3.3 Photon motion 40
1.4 Conclusions 43

2 Black hole shadows in extended theories of gravity **45**
2.1 Shadows and observables of four-dimensional Einstein-Gauss-Bonnet black hole in perfect fluid dark matter 45
2.1.1 Nonrotating black hole shadows 45
2.1.2 Rotating black hole shadows 47
2.1.3 Parameter estimation 48
2.2 Black hole shadow in nonlinear electrodynamics 52
2.3 Shadow of four-dimensional Einstein-Gauss-Bonnet black hole in the power Yang-Mills field 55
2.3.1 Black hole shadow 55
2.3.2 Distortion 58

2.4 Conclusions 60

3 Constraints on black hole parameters using Event Horizon Telescope observations 62

3.1 Constraining with Event Horizon Telescope data 63
3.2 Four-dimensional Einstein-Gauss-Bonnet black holes in perfect fluid dark matter: constraints 64
3.3 Novel charged black holes in nonlinear electrodynamics: constraints 65
3.4 Four-dimensional Einstein-Gauss-Bonnet black holes in power Yang-Mills field: constraints 67
3.5 Conclusions 71

Conclusion 73

Abbreviations

GR	general relativity
SMBH	supermassive black hole
SgrA*	Sagittarius A*
M87	Miessner 87
EHT	Event Horizon Telescope
ngEHT	next-generation Event Horizon Telescope
LISA	Laser Interferometer Space Antenna
NED	nonlinear electrodynamics
EGB	Einstein-Gauss-Bonnet
PFDM	perfect fluid dark matter
PYM	power Yang-Mills (field)
NJA	Newman-Janis algorithm
HJ	Hamilton-Jacobi
GB	Gauss-Bonnet
4D EGB	4-dimensional Einstein-Gauss-Bonnet
DM	dark matter
YM	Yang-Mills
EH	Einstein-Hilbert
EFE	Einstein Field Equations
RN	Reissner-Nordström
EH	Event horizon
CH	Cauchy horizon

Introduction

Topicality and demand of the theme of the dissertation. The study of black holes in alternative theories of gravity is a highly relevant and rapidly evolving field in modern astrophysics and theoretical physics. With groundbreaking observations from the Event Horizon Telescope (EHT), including the first images of supermassive black holes M87* and Sgr A*, there is an urgent need to test general relativity (GR) in extreme gravitational regimes. The discovery of deviations from classical black hole solutions could provide crucial insights into quantum gravity, dark matter, and nonlinear electrodynamics (NED).

This dissertation explores novel black hole solutions in extended gravity models, such as 4D Einstein-Gauss-Bonnet (EGB) gravity, NED addressing key questions in contemporary physics. Testing GR Alternatives: Modified gravity theories (e.g., EGB, NED) predict black hole properties that differ from GR, making them testable with EHT observations. Dark Matter Influence: The interaction between black holes and perfect fluid dark matter (PFDM) affects black hole shadows, offering a new way to probe dark matter distributions near galactic centers. Method Development: The parameter estimation approach based on black hole shadow analysis has been improved and further refined to enhance the accuracy and reliability of extracting black hole and surrounding matter properties.

The demand for such research is underscored by upcoming high-resolution observatories (e.g., next-generation EHT, LISA), which will further constrain black hole parameters and gravity models. By combining shadow analysis with observational constraints, this work provides a unified framework for distinguishing between GR and alternative theories, making it essential for future astrophysical tests and theoretical advancements. Thus, this dissertation addresses pressing questions in fundamental physics while contributing to the interpretation of cutting-edge observational data.

In addition, this dissertation research is aligned with the priority scientific directions of the Republic of Uzbekistan and the broader international scientific community. The results of the research contribute, to a certain extent, to the implementation of the tasks set forth in the Law of the Republic of Uzbekistan

No. O‘RQ-576 “On Science and Scientific Activity” dated October 29, 2019; the Decree of the President of the Republic of Uzbekistan No. PF-6097 “On Approval of the Concept for the Development of Science until 2030” dated October 29, 2020; the Resolution of the President of the Republic of Uzbekistan No. PQ-5032 “On Measures to Improve the Quality of Education and Develop Scientific Research in the Field of Physics” dated March 19, 2021; as well as other regulatory and legal documents related to this area of activity.

Relevance of the research to the priority areas of science and technology development of the Republic of Uzbekistan. Dissertation research has been carried out in accordance with the priority areas of science and technology in the Republic of Uzbekistan: II. "Power, energy and resource saving."

Degree of study of the problem.

The study of black holes in alternative theories of gravity has been an active area of research since the early developments of general relativity. Classical black hole solutions, such as the Schwarzschild and Kerr metrics, have been extensively analyzed, but modifications due to higher-curvature corrections (Boulware, Glavan, Lin, Fernandes, Kumar, Ghosh, Lu, Pang, Hennigar), nonlinear electrodynamics (Born, Infeld, Ayon-Beato, Garcia, Bronnikov, Dymnikova, Balart), and dark matter (Haroon, Jusufi, Hou, Narzilloev, Atamurotov) interactions remain less explored. Recent works, including those by Glavan and Lin (2020) on 4D Einstein-Gauss-Bonnet gravity and Born-Infeld-type NED models, have expanded the theoretical framework, yet observational constraints from the Event Horizon Telescope have only recently allowed for empirical testing of these models (Synge, Bardeen, Hioki, Maeda, Johannsen, Psaltis, Event Horizon Telescope Collaboration, Vagnozzi). Although significant progress has been made in deriving black hole solutions in modified gravity, the connection between theoretical predictions and astrophysical observations—particularly regarding black hole shadows and parameter estimation methods—requires further refinement.

Despite advances, key gaps persist in the literature. Most studies focus on static or spherically symmetric black holes, whereas rotating solutions, more relevant for astrophysical black holes, are less understood in alternative gravity. Additionally, the influence of dark matter on black hole shadows has been explored in simplified scenarios, but a comprehensive analysis of black hole dynamics in perfect fluid dark matter or Power-Yang-Mills (PYM) fields remains incomplete. This dissertation addresses these gaps by systematically analyzing rotating black holes in NED, EGB, linking theoretical predictions to EHT observations, and providing new constraints on deviations from GR. Taking all of this into account, we aimed to study black holes in alternative theories of gravity, including nonlinear

electrodynamics, four-dimensional Einstein–Gauss–Bonnet gravity with perfect fluid dark matter, and in power Yang–Mills field. The work builds upon existing studies while extending them to more realistic, observationally testable scenarios.

Connection of the topic of the dissertation to the scientific works of higher education and research institutions, where the dissertation is carried out. The dissertation was carried out within the framework of scientific projects funded by the Ministry of Innovative Development. F-FA-2021-510 "Investigations of Nuclear Matter of Neutron Stars in Modified Gravity".

The aim of the research The aim of the research is to test alternative gravity theories using black hole shadows, and EHT observational constraints.

The tasks of the research:

- to derive novel black hole solutions in nonlinear electrodynamics and 4D Einstein-Gauss-Bonnet gravity;
- to extend static solutions to rotating cases using the Newman-Janis algorithm and analyze horizon structures;
- to study photon motion and effective potentials to determine unstable circular orbits and shadow boundaries.
- to calculate black hole shadows for different gravity models and compare them with EHT observations.
- to estimate black hole parameters (spin, charge, coupling constants) from shadow observables (area, oblateness).
- to confront theoretical predictions with EHT data to constrain deviations from general relativity.

The objects of the research are rotating and static black holes in nonlinear electrodynamics; 4D Einstein-Gauss-Bonnet black holes surrounded by perfect fluid dark matter; black holes in Power-Yang-Mills fields within modified gravity; Supermassive black holes M87* and Sgr A* as observational test cases.

The subjects of the research are metric solutions and horizon structures of alternative gravity black holes; photon spheres and unstable circular orbits in modified spacetimes; black hole shadow morphology and observable parameters; parameter estimation techniques using Event Horizon Telescope data; constraints on modified gravity parameters from astrophysical observations; and comparative analysis of different alternative gravity scenarios.

The methods of the research are methods of analytical modeling for application of nonlinear electrodynamics and modified gravity field equations; numerical techniques for implementation of the Newman-Janis algorithm for generating rotating black hole solutions; Hamilton-Jacobi formalism for calculation of effective potentials for test particle motion; standard methods for black hole shadow reconstruction; and comparative analysis for systematic evaluation of different gravity models.

The scientific novelty of the research is the following:

- For the first time, it has been derived previously unknown rotating black hole solutions in 4D Einstein-Gauss-Bonnet gravity coupled with perfect fluid dark matter and power Yang-Mills field, extending beyond classical Kerr metrics.
- Parameter estimations have been obtained for 4D Einstein–Gauss–Bonnet black holes surrounded by perfect fluid dark matter.
- Unique observational signatures of PFDM in black hole shadows have been identified, demonstrating that dark matter density profiles can be constrained through high-resolution imaging.

Practical results are the following:

- For the first time, quantitative constraints have been provided on black hole spin (a), NED charge (q), and Gauss-Bonnet coupling (α) using Event Horizon Telescope data, offering testable predictions for future observations.
- It has been modified to open-access numerical codes for simulating shadows and parameter estimations in alternative gravity scenarios, enabling broader community verification.
- Specific shadow distortions have been predicted for ngEHT, prioritizing observational targets to discriminate between GR and alternative theories.

Reliability of the research results provided by applying modern, proven methods of mathematical physics, computational mathematics, and relativistic astrophysics. All derived black hole solutions satisfy the fundamental field equations of their respective modified gravity theories, except for the rotating solutions obtained via the Newman–Janis algorithm, which are treated as approximate solutions and may require additional matter sources. Critical results (e.g., shadow radii, distortions) were computed using independent analytical and numerical methods, with agreement confirming robustness. Parameter constraints

align with empirical data from the Event Horizon Telescope (M87, Sgr A), and deviations from GR predictions remain within the current observational uncertainties. Assumptions (e.g., asymptotic flatness, specific dark matter profiles) and their potential impacts are explicitly addressed, defining the scope of applicability.

The scientific and practical significance of the research results.

- Obtained results provide rigorous tests of alternative gravity models (e.g., 4D EGB, NED) by comparing their black hole solutions with observational data, helping to validate or constrain extensions to general relativity.
- The results demonstrate how black hole shadows and dynamics can reveal the presence and distribution of dark matter, offering a novel astrophysical tool to study this elusive component of the universe.
- The study delivers concrete, observationally testable predictions (shadow size and shapes) for current (EHT) and future (ngEHT) instruments, guiding efforts to detect deviations from GR.
- Analysis develops open-access analytical frameworks and numerical codes for black hole shadow and parameter estimations in modified gravity, enabling broader research and collaborative verification.

Applications of the research results.

The results of the study of the dynamics of particles around black holes in modified gravity theories have been applied as follows:

The theoretical research results and methods, published in the scientific paper "Furkat Sarikulov, Farruh Atamurotov, Ahmadjon Abdujabbarov, Bobomurat Ahmedov, Shadow of the Kerr-like black hole // The European Physical Journal C, Vol. 82 (2022), 9, 771 (Web of Science: IF=4.2), https://doi.org/10.1140/epjc/s10052-022-10711-4" and presented in the Doctorate (PhD) thesis of F. Sarikulov have been used in the framework of programs supported by the Fudan University (Letter from Prof. Cosimo Bambi).

Approbation of the research results. The dissertation results have been discussed in 1 international and 1 local conference.

Volume and structure of the dissertation.

The dissertation consists of an introduction, three chapters, a conclusion, and references, all in 85 pages.

List of published papers [1–14]

Part I

1. Muhammad Ali Raza, Javlon Rayimbaev, **Furkat Sarikulov**, M. Zubair, Bobomurat Ahmedov, Zdeněk Stuchlík, Shadow of novel rotating black hole in GR coupled to nonlinear electrodynamics and constraints from EHT results // *Physics of the Dark Universe*, Vol. 44 (2024), 101488 (№ 1. Web of Science: IF=5)

2. Muhammad Zahid, **Furkat Sarikulov**, Chao Shen, Maksud Umaraliyev, Javlon Rayimbaev, Shadow and quasinormal modes of novel charged rotating black hole in Born–Infeld theory: Constraints from EHT results, // *Physics of the Dark Universe*, Vol. 46 (2024), 101616 (№ 1. Web of Science: IF=5)

3. Farruh Atamurotov, **Furkat Sarikulov**, Sushant G. Ghosh, G. Mustafa, Exploring perfect fluid dark matter with EHT results of Sgr A* through rotating 4D-EGB black holes // *Physics of the Dark Universe*, Vol. 46 (2024), 105625 (№ 1. Web of Science: IF=5)

4. Odil Yunusov, Javlon Rayimbaev, **Furkat Sarikulov**, Muhammad Zahid, Ahmadjon Abdujabbarov, Zdeněk Stuchlík, Rotating charged black holes in EMS theory: shadow studies and constraints from EHT observations // *The European Physical Journal C*, Vol. 84 (2024), 12, 1240 (№ 1. Web of Science: IF=4.2)

5. Muhammad Zahid, **Furkat Sarikulov**, Chao Shen, Javlon Rayimbaev, Kodir Badalov, Sokhibjan Muminov, Shadow and quasinormal modes of rotating charged black holes in Kalb–Ramond gravity and implications from EHT data // *Chinese Journal of Physics*, Vol. 91 (2024), Pages 45-65 (№ 1. Web of Science: IF=4.6)

6. Muhammad Zahid, **Furkat Sarikulov**, Chao Shen, Saidmuhammad Ahmedov, Javlon Rayimbaev, Shadow of rotating black holes surrounded by dark fluid with Chaplygin-like equation of state and constraints from EHT results // *Classical and Quantum Gravity*, Vol. 41 (2024), 20, 205004 (№ 1. Web of Science: IF=3.6)

7. Saeed Ullah Khan, Javlon Rayimbaev, **Furkat Sarikulov**, Ozodbek Abdurakhmonov, Optical features of rotating quintessential charged black holes in de-Sitter spacetime // *Chinese Journal of Physics*, Vol. 90 (2024), Pages 690-706 (№ 1. Web of Science: IF=4.6)

8. M. Zubair, Muhammad Ali Raza, **Furkat Sarikulov**, Javlon Rayimbaev, 4D Einstein-Gauss-Bonnet black hole in Power-Yang-Mills field: a shadow

study // *Journal of Cosmology and Astroparticle Physics*, Vol. 10 (2023), 058 (№ 1. Web of Science: IF=5.3)

9. Muhammad Zahid, Javlon Rayimbaev, **Furkat Sarikulov**, Saeed Ullah Khan, Jingli Ren, Shadow of rotating and twisting charged black holes with cloud of strings and quintessence // *The European Physical Journal C*, Vol. 83 (2023), 9, 855 (№ 1. Web of Science: IF=4.2)

10. **Furkat Sarikulov**, Farruh Atamurotov, Ahmadjon Abdujabbarov, Vokhid Khamidov, The photon motion and weak gravitational lensing in a black-bounce spacetime // *Chinese Physics C*, Vol. 47 (2023), 11, 115101 (№ 1. Web of Science: IF=3.6)

11. Javlon Rayimbaev, Konstantinos F. Dialektopoulos, **Furkat Sarikulov**, Ahmadjon Abdujabbarov, Quasiperiodic oscillations around hairy black holes in Horndeski gravity // *The European Physical Journal C*, Vol. 83 (2023), 572 (№ 1. Web of Science: IF=4.2),

12. **Furkat Sarikulov**, Farruh Atamurotov, Ahmadjon Abdujabbarov, Bobomurat Ahmedov, Shadow of the Kerr-like black hole // *The European Physical Journal C*, Vol. 82 (2022), 9, 771 (№ 1. Web of Science: IF=4.2)

13. Farruh Atamurotov, **Furkat Sarikulov**, Vokhid Khamidov, Ahmadjon Abdujabbarov, Gravitational weak lensing of Schwarzschild-like black hole in presence of plasma // *The European Physical Journal Plus*, Vol. 137 (2022), 5, 567 (№ 1. Web of Science: IF=2.8)

14. Farruh Atamurotov, **Furkat Sarikulov**, Ahmadjon Abdujabbarov, Bobomurat Ahmedov, Gravitational weak lensing by black hole in Horndeski gravity in presence of plasma // *The European Physical Journal Plus*, Vol. 137 (2022), 3, 336 (№ 1. Web of Science: IF=2.8)

Part II

15. **Sariqulov F. Sh.**, Atamurotov F. S., Sariyev U. Q. Parameter estimation of Kerr-like black hole from its shadow. O‘zbekiston Milliy universiteti “Fizika fanining rivojida iste’dodli yoshlarning o’rni” RIAK-XV, 22-23 aprel, 2022.

16. **Sariqulov F. Sh.**, Atamurotov F. S., Matniyozov Z. Effect of plasma on deflection angle by a hairy black hole in horndeski gravity. O‘zbekiston Milliy universiteti “Fizika fanining rivojida istedodli yoshlarning o’rni” RIAK-XV, 22-23 aprel, 2022.

Chapter 1

Novel black hole solutions in extended gravity models and photon motion around them

1.1 Novel charged black holes with nonlinear electrodynamics

In general relativity (GR), black holes are commonly described through parameters such as mass, electric charge, and angular momentum. Charged black hole configurations may originate from either Maxwell electrodynamics or nonlinear electrodynamics (NED) frameworks. The first electrically and magnetically charged solutions were independently obtained by H. Reissner and G. Nordström [15, 16]. Although these Einstein–Maxwell solutions contain spacetime singularities, introducing nonlinear electrodynamics coupled to general relativity allows the construction of nonsingular geometries commonly known as regular black holes [17–24].

The nonlinear electrodynamics model proposed by Born and Infeld [25] was originally developed to obtain a finite self-energy for point-like charges. A distinctive feature of this theory is the presence of the nonlinearity parameter b in the corresponding Lagrangian. In the appropriate limiting case of b, the Born-Infeld framework converges to Maxwell's linear theories. This framework inspired the development of various models within the NED domain, as noted in [26–28]. Over the years, numerous NED theories have been proposed, some closely resembling the Born-Infeld theory, while others are distinct. A major motivation behind these theories was the construction of models with a finite electric field at the origin, which could in principle lead to regular black hole geometries. Nevertheless, none of these approaches has completely achieved this goal. In this context, we consider the NED model proposed in [23] together with the corresponding

black hole solutions obtained from it. The Lagrangian indicates that Maxwell's linear electrodynamics are recovered when $b \to \infty$, a characteristic similar to Born-Infeld type theories is owing to the Lagrangian configuration. In addition, the corresponding electric field remains finite near the origin while approaching the Coulomb form at large distances, which makes this NED model particularly interesting to investigate. Although the associated black hole solution is not regular, it still possesses several noteworthy properties that will be analyzed in future studies. Unless explicitly stated otherwise, geometrized units with $c = G = 1$ are used throughout this work.

The coupling of Einstein gravity with the considered NED model is introduced through the following action: [23].

$$S = \int dx^4 \sqrt{-g} \left[\frac{R}{16\pi G} + \mathcal{L}(\mathcal{F}) \right], \tag{1.1}$$

where G corresponds to the gravitational constant, R is the Ricci scalar, and g denotes the determinant of the metric tensor. The Lagrangian associated with the NED model is given by [23]

$$\mathcal{L}(\mathcal{F}) = \frac{-4b\mathcal{F}}{\left(\sqrt{b} + \sqrt{b - 2\sqrt{-\frac{\mathcal{F}}{2}}} \right)^2}. \tag{1.2}$$

Here, $4\mathcal{F} = F_{\mu\nu}F^{\mu\nu} = 2\left(B^2 - E^2\right)$ corresponds to the Maxwell invariant, while b characterizes the nonlinearity parameter of the model. In the limit $b \to \infty$, the expansion of the Lagrangian (1.2) is given by

$$\mathcal{L}(\mathcal{F}) = -\mathcal{F} - \frac{\sqrt{-\mathcal{F}}\mathcal{F}}{\sqrt{2}b} + \frac{5\mathcal{F}^2}{8b^2} + \frac{7\sqrt{-\mathcal{F}}\mathcal{F}^2}{8\sqrt{2}b^3} + \mathcal{O}\left(\frac{1}{b^4}\right). \tag{1.3}$$

When $b \to \infty$, the standard Maxwell electrodynamics Lagrangian is recovered. By taking the magnetic field as $B = 0$ and solving the field equation $\nabla_\mu \left(F^{\mu\nu} \frac{\partial \mathcal{L}}{\partial \mathcal{F}} \right) = 0$, the electric field configuration $E(r)$ can be obtained [23]

$$E(r) = \frac{bq(2br^2 + q)}{2(br^2 + q)^2}, \tag{1.4}$$

with q the representation of the electric charge parameter. The asymptotic behavior of the electric field given in Eq. (1.4), together with its behavior near the

origin, may respectively be written as

$$E(r) = \frac{q}{r^2} - \frac{3q^2}{2br^4} + \mathcal{O}\left(\frac{1}{r^6}\right), \tag{1.5}$$

$$E(r) = \frac{b}{2} - \frac{b^3 r^4}{2q^2} + \mathcal{O}\left(r^6\right). \tag{1.6}$$

The electric field $E(r)$ decreases with increasing radial distance from the source, and unlike the case of linear Maxwell electrodynamics, it remains finite at the origin. Varying the action (1.1) and solving the corresponding field equations for a static and spherically symmetric spacetime metric gives the black hole solution given by:

$$ds^2 = -f(r)dt^2 + \frac{dr^2}{f(r)} + r^2\left(d\theta^2 + \sin^2\theta d\phi^2\right) \tag{1.7}$$

with the metric function

$$f(r) = 1 - \frac{2M}{r} + \frac{\pi q\sqrt{bq}}{2r} - \frac{q\sqrt{bq}}{r}\tan^{-1}\left(\frac{\sqrt{b}r}{\sqrt{q}}\right), \tag{1.8}$$

where M represents the mass of the black hole. The series expansion of the metric function $f(r)$ in the limit $r \to \infty$ takes the form

$$f(r) = 1 - \frac{2M}{r} + \frac{q^2}{r^2} - \frac{q^3}{3br^4} + \mathcal{O}\left(\frac{1}{r^5}\right), \tag{1.9}$$

The metric function satisfies $f(r) \to 1$ in the limit $r \to \infty$, which implies that the spacetime described by Eq. (1.7) is asymptotically flat. At sufficiently large radial distances, the obtained black hole geometry approaches the Reissner-Nordström solution. Furthermore, an expansion of $f(r)$ in the small-b regime yields:

$$f(r) = 1 - \frac{2M}{r} + \frac{\pi b^{1/2}q^{3/2}}{2r} - bq + \frac{b^2r^2}{3} - \frac{b^3r^4}{5q} + \mathcal{O}\left(b^4\right). \tag{1.10}$$

In the limit $b \to 0$, the black hole metric (1.7) reduces to the Schwarzschild solution. On the other hand, in the limit $b \to \infty$, it reduces to the Reissner-Nordström metric:

$$f(r) = 1 - \frac{2M}{r} + \frac{q^2}{r^2} - \frac{q^3}{3r^4b} + \frac{q^4}{5r^6b^2} - \frac{q^5}{7b^3r^8} + O\left(b^{-4}\right) \tag{1.11}$$

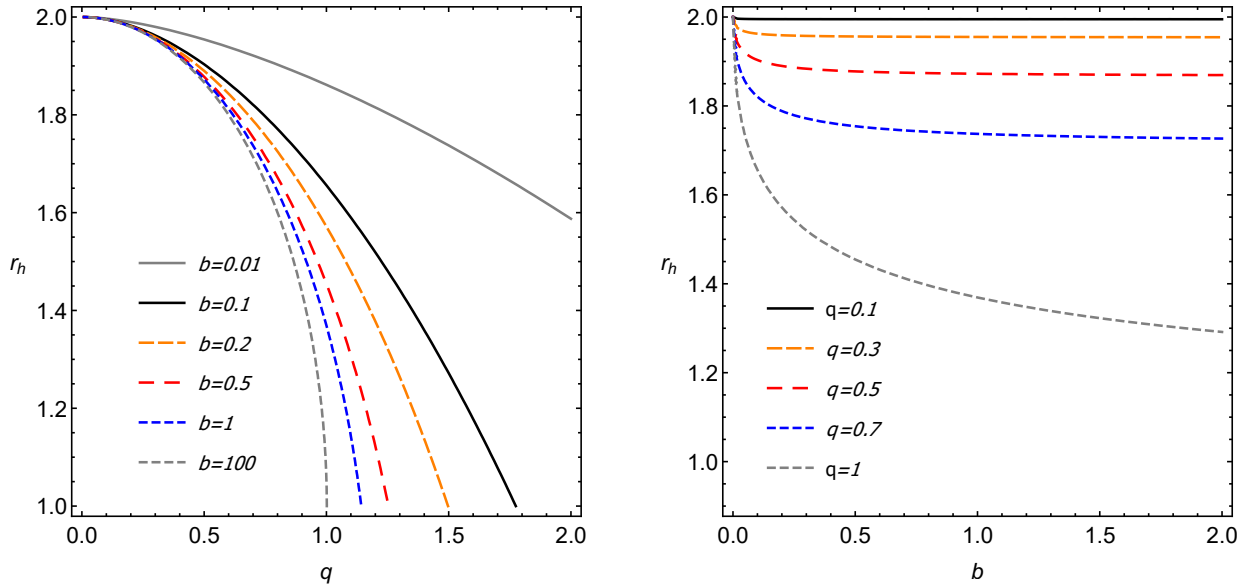


Figure 1.1: The dependencies of the event horizon radii on parameters q and b, with $M = 1$.

We now investigate the horizon structure of the spacetime 1.7 and analyze the allowed ranges of the model parameters for which black hole solutions exist. Figure 1.1 shows the dependencies of the event horizon radius on the black hole parameters, determined from the condition $f(r) = 0$. From these results, it is observed that the horizon radius gets smaller with increasing charge parameter q, whereas the effect of the parameter b becomes less significant in the regime of large parameter values. Moreover, in the large-b regime, the model approaches the behavior of linear electrodynamics. Next, we identify the parameter space in which black hole solutions are allowed. In Fig. 1.2, the allowed ranges of parameters q and b are described. As the parameter b increases, the maximum allowed value of the charge q asymptotically approaches the limit $q/M = 1$, thereby mimicking the behavior of the Reissner-Nordström black hole metric. Consequently, it is the small-b regime that captures the genuinely nonlinear features of the model and thus warrants particular attention. It is useful to note that, although the metric mathematically permits large values of q for sufficiently small b, physical consistency requires consideration that the limits $b \to 0$ and $q \to 0$ be satisfied simultaneously.

1.1.1 Effective geometry for photon propagation in nonlinear electrodynamics

Photons propagating in a nonlinear electrodynamics background can interact with the field, leading to deviations from standard null geodesics. Nevertheless, it

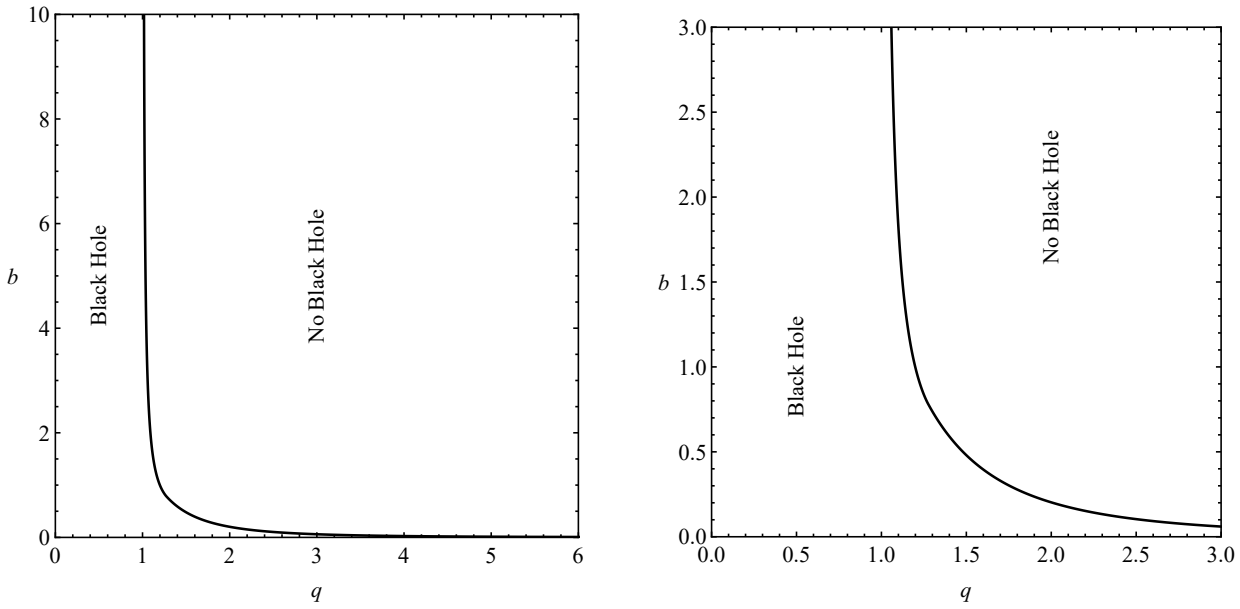


Figure 1.2: Plots illustrating the parameter space (b, q) for the existence of an event horizon for the NED black hole, with $M = 1$.

is possible to introduce an effective metric in which photon trajectories still satisfy null geodesic equations. As a result, the optical characteristics of the spacetime, in particular the black hole shadow, are determined by this effective geometry rather than the background metric itself. In this context, we study photon motion around a charged black hole in NED by constructing the corresponding effective metric.

In linear electrodynamics, electromagnetic waves do not interact with electrostatic fields. In contrast, nonlinear electrodynamics introduces self-interaction effects, so that photons can couple to the background field and deviate from standard null geodesics. Therefore, the motion of photons in black hole spacetimes described by GR coupled to NED must be reconsidered. In this framework, the relevant optical properties are governed by the lapse function in Eq. (1.8) through the so-called effective geodesics of photons propagating in the curved background, as introduced in [29–31].

$$\tilde{g}^{\mu\nu} = g^{\mu\nu} - 4\frac{\mathcal{L}_{\mathcal{F}\mathcal{F}}}{\mathcal{L}_{\mathcal{F}}}F^{\lambda}_{\mu}F^{\mu\nu}, \tag{1.12}$$

$$\tilde{g}_{\mu\nu} = 16\frac{\mathcal{L}_{\mathcal{F}\mathcal{F}}F_{\mu\eta}F^{\eta}_{\nu} - (\mathcal{L}_{\mathcal{F}} + 2\mathcal{F}\mathcal{L}_{\mathcal{F}\mathcal{F}})g_{\mu\nu}}{\mathcal{F}^2\mathcal{L}^2_{\mathcal{F}\mathcal{F}} - 16(\mathcal{L}_{\mathcal{F}} + \mathcal{F}\mathcal{L}_{\mathcal{F}\mathcal{F}})^2}, \tag{1.13}$$

where

$$\mathcal{L}_{\mathcal{F}} = \frac{\partial\mathcal{L}(\mathcal{F})}{\partial\mathcal{F}}, \qquad \mathcal{L}_{\mathcal{F}\mathcal{F}} = \frac{\partial^2\mathcal{L}(\mathcal{F})}{\partial\mathcal{F}^2}. \tag{1.14}$$

The propagation of photons in the effective spacetime associated with the black

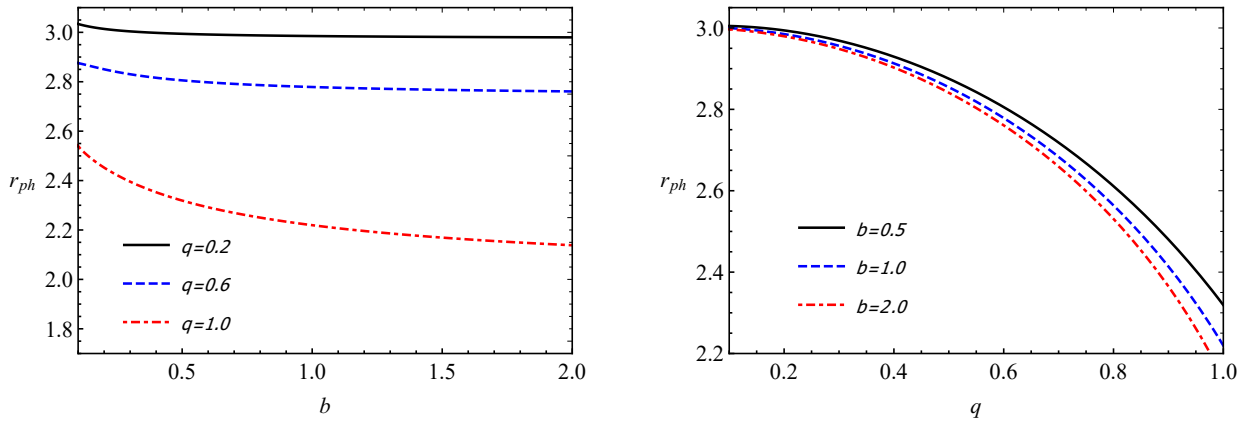


Figure 1.3: The dependencies of photon radii around black hole in NED on parameters b and q, with M=1.

hole can be described in the eikonal approximation by the following equation:

$$\tilde{g}_{\mu\nu}k^{\mu}k^{\nu} = 0, \tag{1.15}$$

Here, k^{μ} is the photon wave four-vector and is directly related to the photon four-momentum via $p^{\mu} = \hbar k^{\mu}$. Using this relation, we now implement the effective geometry formalism for photons propagating in the spacetime described by Eq. (1.7).

For a purely electric field configuration, the only nonvanishing component of the electromagnetic tensor is electric field strength and the electromagnetic invariant becomes

$$F = -\frac{1}{2}E^2(r). \tag{1.16}$$

where $E(r)$ is given by Eq. (1.4). In this case, the effective line element governing photon propagation can be written as

$$ds^2_{\text{eff}} = -\frac{f(r)}{\mathcal{L}_F}\,dt^2 + \frac{dr^2}{f(r)\mathcal{L}_F} + \frac{r^2}{\Phi(r)}\left(d\theta^2 + \sin^2\theta\,d\phi^2\right), \tag{1.17}$$

where the function $\Phi(r)$ is given by

$$\Phi(r) = \mathcal{L}_F - 2F\mathcal{L}_{FF} \tag{1.18}$$

The effective spacetime admits two constants of motion associated with its symmetries, namely the photon energy E and angular momentum L. Without loss of generality, we consider photon motion restricted to the equatorial plane $\theta = \pi/2$. Under these conditions, the radial equation governing the trajectory can be expressed as

$$\dot{r}^2 + V_{\text{eff}}(r) = 0, \tag{1.19}$$

with the effective potential

$$V_{\text{eff}}(r) = \frac{f(r)}{r^2}\frac{\Phi(r)}{\mathcal{L}_F}\,L^2 - E^2. \tag{1.20}$$

The circular photon trajectories, which define the photon sphere and play a key role in determining the black hole shadow, are obtained by imposing the conditions

$$V_{\text{eff}}(r) = 0, \qquad \frac{dV_{\text{eff}}(r)}{dr} = 0. \tag{1.21}$$

These conditions lead to the master equation

$$\frac{d}{dr}\left(\frac{r^2\mathcal{L}_F}{f(r)\Phi(r)}\right) = 0. \tag{1.22}$$

Using the above equation, one can evaluate the photon sphere radius. Figure 1.3 presents the variation of the photon sphere radius with respect to the parameters q and b. It can be seen that the radius decreases as the electric charge parameter q increases. On the other hand, the effect of the parameter b becomes appreciable only in the regime of comparatively large values of q. Overall, this behavior indicates that the photon sphere structure is primarily governed by the electric charge parameter, while nonlinear effects associated with b play a secondary role except in the strong-charge regime. This interplay between q and b provides further insight into how nonlinear electrodynamic corrections modify the optical properties of the black hole spacetime.

1.2 Four-dimensional Einstein-Gauss-Bonnet black hole surrounded by perfect fluid dark matter

Although general relativity has been highly successful in describing gravitational phenomena, it faces challenges in regimes involving strong curvature, such as those near black hole horizons. These limitations have motivated the study of extended gravitational frameworks that go beyond the Einstein-Hilbert action by including higher-curvature contributions. A well-known example of such an extension is Einstein-Gauss-Bonnet (EGB) gravity, which arises when a quadratic curvature invariant, the Gauss-Bonnet term, is added to the action. This theory is of particular interest because it appears naturally in the low-energy limit of string theory and also provides a consistent higher-dimensional generalization of general relativity. The formulation of the Gauss-Bonnet term was originally introduced by Lanczos [32] and later generalized within Lovelock gravity [33]. One of

the appealing features of EGB gravity is the absence of ghost degrees of freedom, since the resulting field equations remain second order in the metric [34]. Moreover, perturbative analyses have shown that the theory is stable when expanded around flat spacetime backgrounds [34,35]. Due to these properties, EGB gravity serves as a useful and well-defined extension of general relativity for exploring conceptual and higher-dimensional aspects of gravitational physics.

EGB gravity has attracted considerable attention, partly because it naturally appears as the low-energy effective description of string theory [36]. Another appealing feature of this framework is that it allows nontrivial gravitational self-interactions while remaining free of ghost degrees of freedom [37]. The first static and spherically symmetric black hole solution in EGB gravity was obtained by Boulware and Deser [34], and later studies have extended these results to a variety of matter sources [38–40], including configurations describing regular black holes [41]. In spacetime dimensions $D < 5$, the Gauss-Bonnet (GB) term becomes a topological invariant and does not contribute to the field equations. Nevertheless, Tomozawa [42] showed that, after an appropriate quantum-level regularization procedure, the GB contribution can become dynamically relevant even in four-dimensional static and spherically symmetric black hole spacetimes. In this setting, the modified dynamics can be expressed as:

$$ds^2 = -f(r)dt^2 + \frac{1}{f(r)}dr^2 + r^2(d\theta^2 + \sin^2\theta d\phi^2), \tag{1.23}$$

where

$$f(r) = 1 + \frac{r^2}{2\alpha}\left[1 \pm \sqrt{1 + \frac{8\alpha M}{r^3}}\right]. \tag{1.24}$$

Here, M denotes the mass of the black hole. In a later development, Cognola et al. [43] proposed a regularization scheme for EGB gravity based on an entropic dimensional reduction procedure in the limit $D \to 4$, implemented at the level of the classical Lagrangian.

In the reformulation of EGB gravity, the Gauss-Bonnet coupling constant is rescaled according to $\alpha/(D-4)$. The corresponding four-dimensional theory is then obtained by taking the limit $D \to 4$, which preserves the dynamical degrees of freedom while avoiding the Ostrogradsky instability [44]. The $D \to 4$ regularization procedure has been the subject of ongoing debate regarding its mathematical consistency, motivating several alternative formulations and regularization schemes [45–47]. Within this framework, static and spherically symmetric black hole solutions of the form (1.23) arise, characterized by the lapse function (1.24). This extension of general relativity is consistent with Lovelock's theorem [48] and

provides a way to circumvent the standard singularity issues, which has led to extensive investigations in the literature [49–53]. It is also worth emphasizing that the metric (1.23), together with the corresponding lapse function (1.24), can be interpreted as a solution emerging from various regularized four-dimensional gravity constructions proposed in recent studies [45–47]. Similar black hole solutions have been obtained through different approaches, including semi-classical modifications of Einstein's equations [54], effective theories incorporating quantum corrections [43], and extensions within Lovelock-type gravity frameworks [46].

In a subsequent work, Kumar and Ghosh extended the static spherically symmetric solution (1.23) to its rotating counterpart, with particular emphasis on rotating four-dimensional Einstein-Gauss-Bonnet black holes [55]. Their analysis focused on both the spacetime geometry and the resulting shadow structures associated with these rotating configurations. By expressing the null geodesic equations in first-order form, they obtained analytical descriptions of the photon region and investigated how the Gauss-Bonnet coupling modifies the corresponding photon trajectories.

We try to add our contribution by extending the analysis of rotating four-dimensional EGB black holes studied in [55], with particular emphasis on the impact of surrounding perfect fluid dark matter (PFDM) on the black hole shadow structure. Black holes serve not only as manifestations of the spacetime geometry but also as indicators of the surrounding matter-energy distribution, thereby providing insight into the physical properties of their environment [56–61]. Moreover, the shadow of a black hole offers an observational window to constrain the properties of otherwise inaccessible surrounding matter distributions [62–65]. This includes not only luminous matter but also dark matter, which remains one of the key open problems in modern physics and accounts for approximately 25% of the total energy density of the Universe [66]. In this context, the phenomenological dark matter model has been widely used as an effective description, in which dark matter is treated as a perfect fluid component [67–70].

1.2.1 Non-rotating black hole

The energy-momentum tensor of the perfect fluid dark matter model can be expressed as [71]

$$T_{\mu}^{\nu,DM} = \text{diag}[\rho, -p_r, -p_\theta, -p_\phi]., \tag{1.25}$$

where ρ represents the energy density of dark matter, while p_r, p_θ, and p_ϕ denote the pressures in various directions. In the PFDM framework, the energy-density profile $\rho(r) \propto r^{-3}$ follows naturally from the combined assumptions of spherical

symmetry and the radial equation of state $p_r = -\rho$. Under these conditions, the Einstein field equations admit a metric potential of the form

$$f(r) = 1 - \frac{2M}{r} + \frac{\beta}{r}\ln\left(\frac{r}{|\beta|}\right),$$

where β is a parameter controlling the amplitude of the dark-matter density. Substituting this potential into the field equations leads to the energy density, [69]

$$\rho(r) = \frac{\beta}{8\pi r^3},$$

which is fully consistent with the PFDM interpretation and automatically satisfies the covariant conservation condition $\nabla_\mu T^{\mu\nu} = 0$.

The weak energy condition requires $\rho \geq 0$, which in turn implies $\beta \geq 0$. This constraint is assumed throughout the present analysis. Under these conditions, the black hole solution in four-dimensional Einstein-Gauss-Bonnet gravity surrounded by perfect fluid dark matter can be written in the form:

$$ds^2 = -f(r)dt^2 + \frac{dr^2}{f(r)} + r^2(d\theta^2 + \sin^2\theta d\phi^2), \tag{1.26}$$

with

$$f(r) = 1 + \frac{r^2}{2\alpha}\left(1 - \sqrt{1 + \frac{4\alpha}{r^3}\left(2M - \beta\ln\left(\frac{r}{\beta}\right)\right)}\right), \tag{1.27}$$

which is a four-dimensional Einstein-Gauss-Bonnet black hole surrounded by perfect fluid dark matter. In the absence of PFDM, the metric can be recovered. In Fig. 1.4, the dependencies of the event horizon radius on the parameters α and β are illustrated. From these results, it is observed that an increase in either parameter leads to a decrease in the event horizon radius.

The motion of photons around the four-dimensional EGB black hole surrounded by PFDM is governed by null geodesics. The photon sphere radius, denoted by r_{ph}, is obtained by analyzing circular null trajectories in this spacetime. In particular, circular photon orbits are determined by the extremum condition of the effective radial potential, which requires its first derivative with respect to the radial coordinate r to vanish. Accordingly, the photon sphere is defined by the condition [64]:

$$\frac{d}{dr}(h(r)^2)\bigg|_{r=r_{ph}} = 0 \tag{1.28}$$

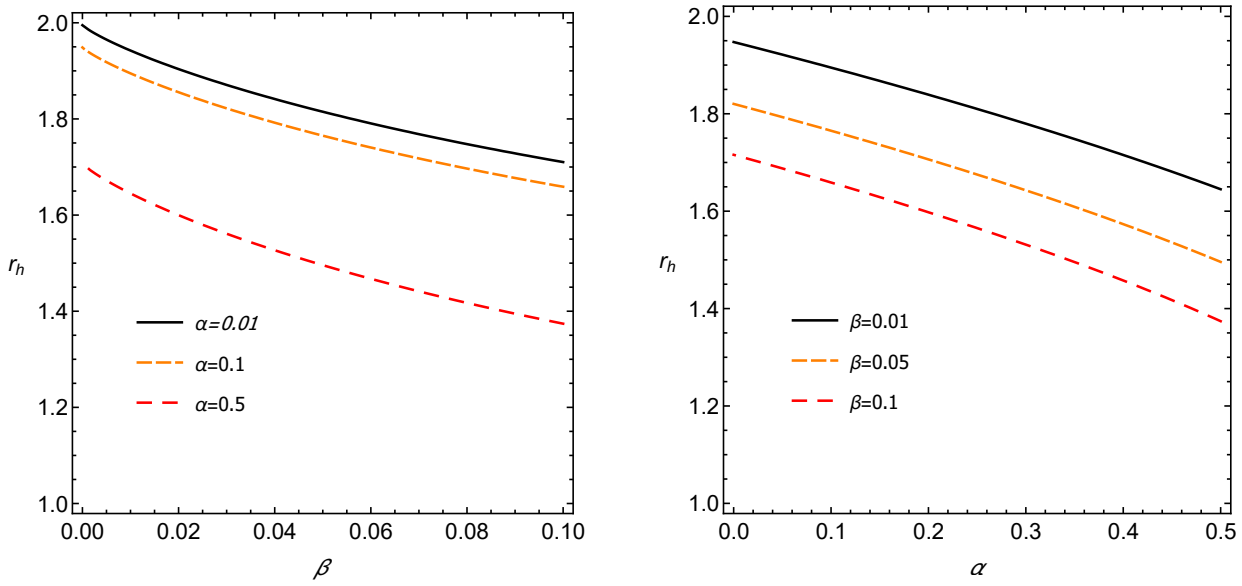


Figure 1.4: The dependencies of the event horizon radii on parameters α and β, with $M = 1$.

with [64]

$$h(r)^2 = \frac{r^2}{f(r)}. \tag{1.29}$$

Applying this condition to the spacetime metric leads to the governing equation for the photon sphere radius, which can be written as:

$$-\beta + 2r\sqrt{\frac{8\alpha + r^3 - 4\alpha\beta\log\left(\frac{r}{\beta}\right)}{r^3}} + 3\beta\log\left(\frac{r}{\beta}\right) - 6 = 0. \tag{1.30}$$

The solution to the equation elucidates the radius of the photon sphere for a non-rotating black hole. Figure 1.5 illustrates the correlation between the radius of the photon sphere and the GB and PFDM parameters. The graphs demonstrate that an increase in the α parameter results in a slight reduction in the radii of the photon sphere. Conversely, the PFDM parameter exerts a significant influence on the photon sphere radius values, also exhibiting a decreasing trend attributable to PFDM.

1.2.2 Rotating black hole

The main objective of this dissertation is to constrain the black hole parameters using Event Horizon Telescope data, and astrophysical black holes are predominantly considered to be rotating. The metric of a rotating black hole represents a fundamental extension of a static black hole, characterized by the inclusion

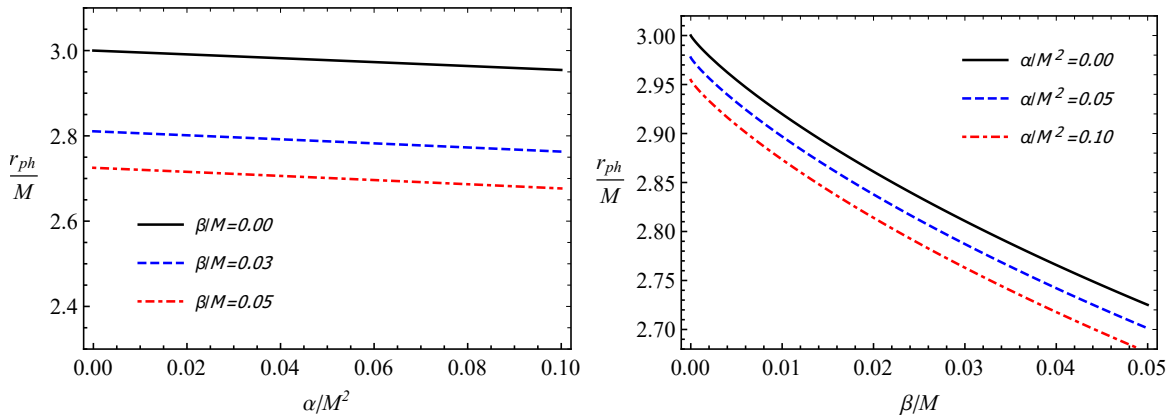


Figure 1.5: Photon sphere radius dependence on the black hole parameters for the non-rotating 4D EGB black hole.

of an additional spin parameter, typically denoted as a. The spacetime structure surrounding a rotating black hole exhibits distinct behaviors and properties compared to its static counterpart, particularly concerning photon motion. The importance of a rotating black hole can be assessed by comparing the black hole shadow with the EHT data for supermassive black holes. Given that known supermassive black holes are rotating, it is more appropriate and precise to conduct shadow comparisons using rotating black holes.

The Newman-Janis algorithm (NJA) provides a procedure for generating rotating counterparts of static black hole solutions within general relativity [72, 73]. Its first applications led to the derivation of the Kerr and Kerr-Newman metrics from the Schwarzschild and Reissner-Nordström spacetimes, respectively. While Schwarzschild and Kerr solutions describe vacuum geometries, the Reissner-Nordström and Kerr-Newman spacetimes include an electromagnetic source associated with electric charge. However, Hansen and Yunes showed that applying the NJA in modified gravity theories can introduce additional, nontrivial source terms that are not easily interpreted [74]. To address this issue, Azreg-Aïnou [75, 76] proposed a modified version of the NJA that avoids the use of complex coordinate transformations. This revised approach has been successfully applied to a variety of matter configurations, including imperfect fluids and regular black hole models [77, 78]. In the present work, we adopt this modified NJA to construct the rotating counterpart of the static metric (1.7).

Initially, we introduce the Eddington-Finkelstein coordinates (u, r, θ, ϕ) and utilize the transformation:

$$du = dt - \frac{dr}{f(r)}, \tag{1.31}$$

the static metric (1.7) becomes

$$ds^2 = -f(r)du^2 - 2dudr + r^2 d\theta^2 + r^2 \sin^2\theta d\phi^2. \tag{1.32}$$

Further, the conjugate metric tensor can be defined as

$$g^{ab} = -l^a n^b - n^a l^b + m^a \bar{m}^b + \bar{m}^a m^b \tag{1.33}$$

with the null tetrads given by

$$l^a = \delta^a_r, \tag{1.34}$$

$$n^a = \delta^a_u - \frac{f(r)}{2}\delta^a_r, \tag{1.35}$$

$$m^a = \frac{1}{\sqrt{2}r}\left(\delta^a_\theta + \frac{i}{\sin\theta}\delta^a_\phi\right). \tag{1.36}$$

In this context, $\bar{m}^a$ represents the complex conjugate of m^a. It becomes evident that the following equations are applicable to these null tetrads:

$$l_a l^a = n_a n^a = m_a m^a = \bar{m}_a \bar{m}^a = 0, \tag{1.37}$$

$$l_a m^a = l_a \bar{m}^a = n_a m^a = n_a \bar{m}^a = 0, \tag{1.38}$$

$$-l_a n^a = -l^a n_a = m_a \bar{m}^a = m^a \bar{m}_a = 1. \tag{1.39}$$

We now undertake the complex coordinate transformations in the (u, r)-plane as follows:

$$u' \to u - ia\cos\theta, \qquad r' \to r + ia\cos\theta, \tag{1.40}$$

The subsequent step in NJA involves the complexification of the radial coordinate r. However, as demonstrated by [75], this complexification is not a prerequisite. The process can be circumvented by recognizing that δ^μ_ν behaves as a vector under the transformation (1.40). Concurrently, the metric functions of the metric (1.32) are transformed into new, undetermined functions, specifically,

$$f(r) \to F(r, a, \theta), \qquad r^2 \to H(r, a, \theta), \tag{1.41}$$

such that

$$\lim_{a\to 0} F(r, a, \theta) = f(r), \qquad \lim_{a\to 0} H(r, a, \theta) = r^2, \tag{1.42}$$

Utilizing this transformation, the null tetrads are expressed as

$$l^a = \delta^a_r, \tag{1.43}$$

$$n^a = \delta^a_u - \frac{F}{2}\delta^a_r, \tag{1.44}$$

$$m^a = \frac{1}{\sqrt{2H}}\left((\delta^a_u - \delta^a_r)ia\sin\theta + \delta^a_\theta + \frac{i}{\sin\theta}\delta^a_\phi\right). \tag{1.45}$$

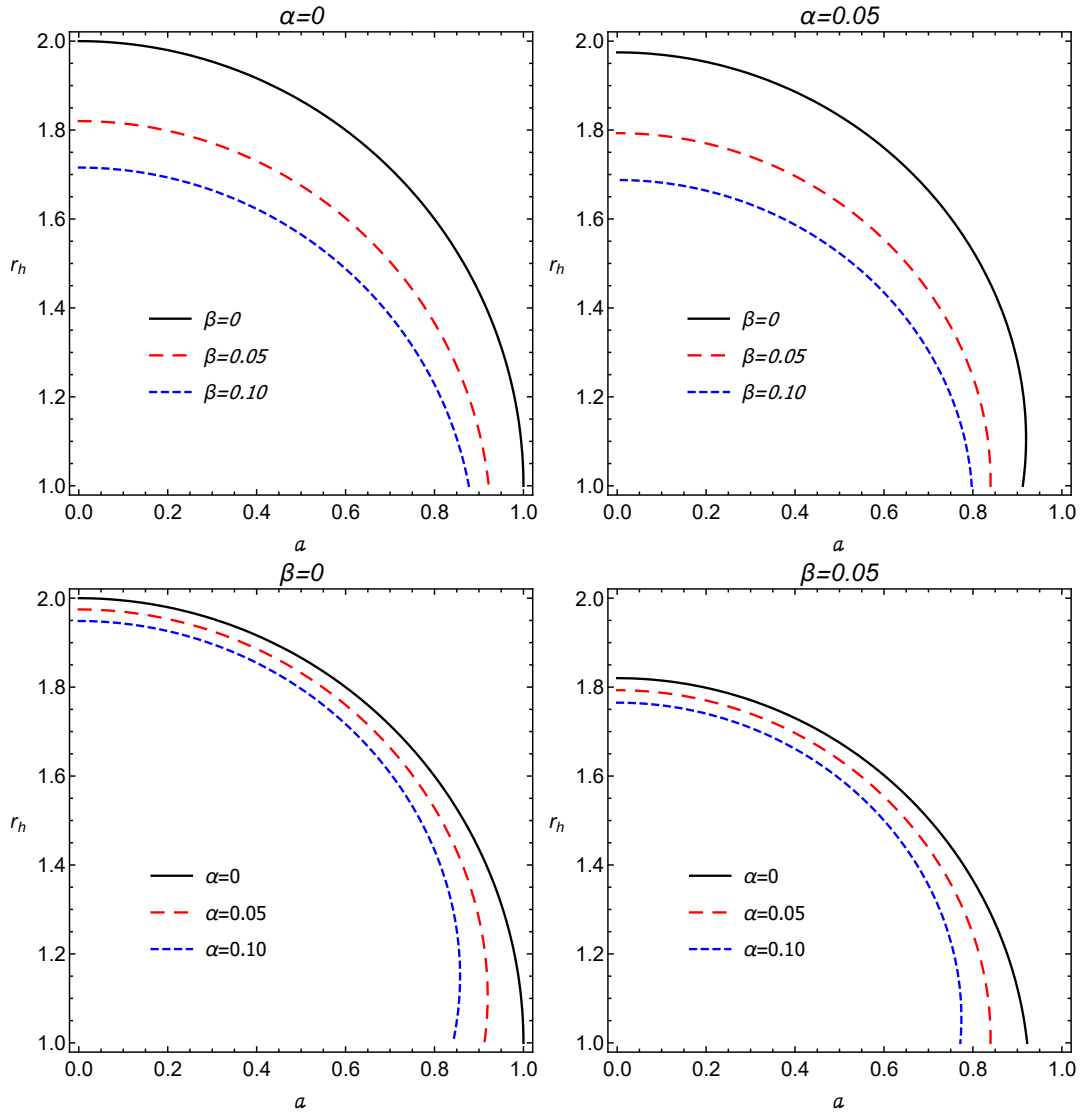


Figure 1.6: The event horizon radius as a function of parameters of rotating 4D EGB black hole in PFDM, with $M = 1$

By employing the newly defined null tetrads, the rotating metric within the framework of Eddington-Finkelstein coordinates is represented as

$$\begin{aligned} ds^2 &= -F du^2 - 2dudr + 2a\sin^2\theta(F-1)dud\phi \\ &\quad +2a\sin^2\theta dr d\phi + Hd\theta^2 \\ &\quad +\sin^2\theta\left(H + a^2\sin^2\theta(2-F)\right)d\phi^2. \end{aligned} \tag{1.46}$$

Reverting to the Boyer-Lindquist coordinates, we derive the rotating equivalent of the static black hole metric (1.7). Consequently, we propose a global coordinate transformation

$$du = dt + \lambda(r)dr, \qquad d\phi = d\phi' + \chi(r)dr, \tag{1.47}$$

where

$$\lambda(r) = -\frac{a^2 + r^2}{a^2 + r^2 f(r)}, \qquad \chi(r) = -\frac{a}{a^2 + r^2 f(r)}. \tag{1.48}$$

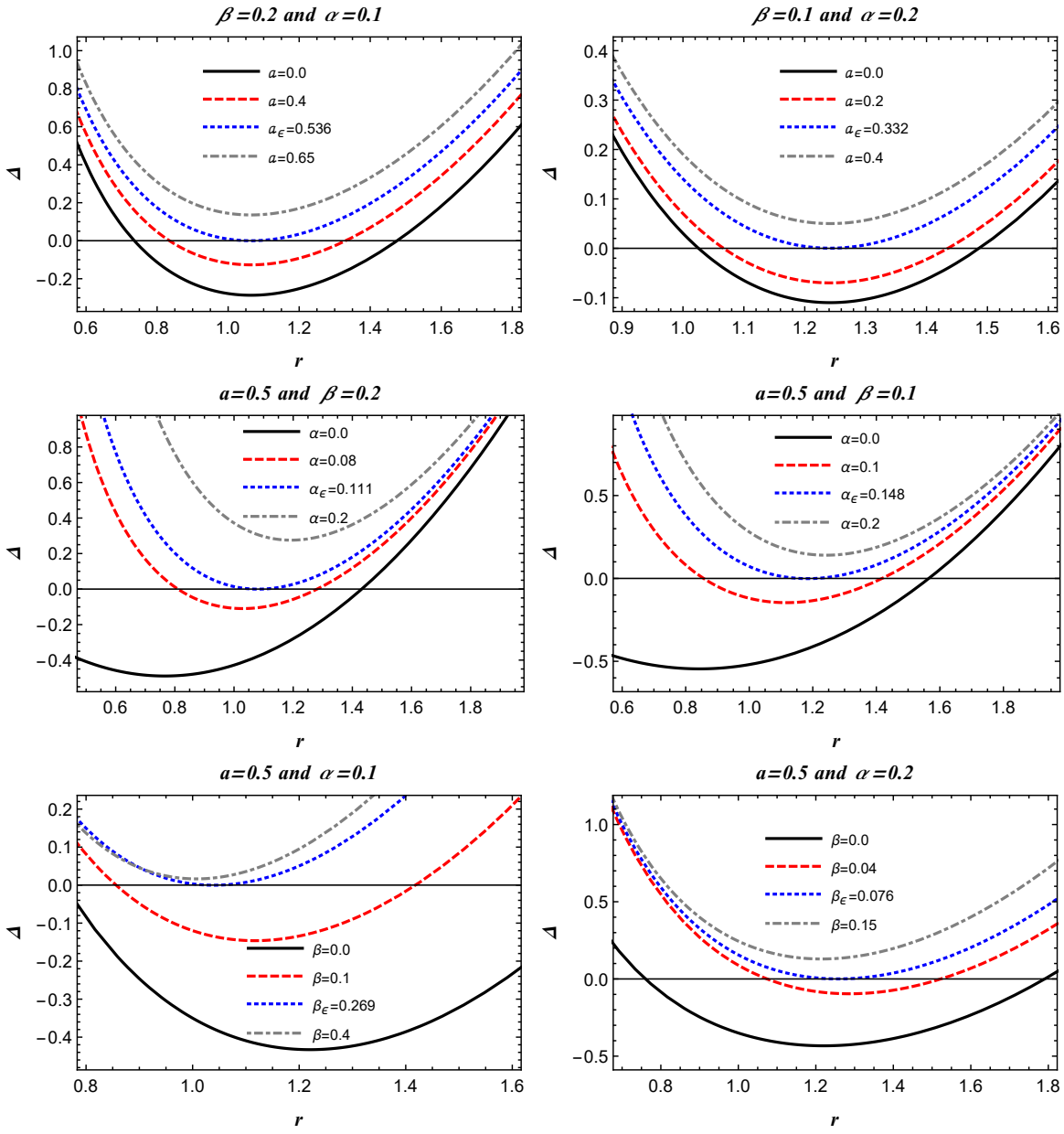


Figure 1.7: The dependencies of the metric function of the 4D EGB black hole in PFDM on the radial coordinate.

Finally, we consider

$$F = \frac{r^2 f(r) + a^2 \cos^2\theta}{H}, \qquad H = r^2 + a^2 \cos^2\theta \tag{1.49}$$

and the Kerr-like rotating black hole metric is given by

$$\begin{aligned} ds^2 &= -\frac{\Delta(r)-a^2\sin^2\theta}{\rho^2}dt^2+\frac{\rho^2}{\Delta(r)}dr^2+\rho^2 d\theta^2 \\ &\quad +\frac{\sin^2\theta}{\rho^2}\left(\left(r^2+a^2\right)^2-\Delta(r)a^2\sin^2\theta\right)d\phi^2 \\ &\quad -\frac{2a\sin^2\theta}{\rho^2}\left(a^2+r^2-\Delta(r)\right)dtd\phi, \end{aligned} \tag{1.50}$$

with the metric functions

$$\rho^2 = r^2+a^2\cos^2\theta, \tag{1.51}$$

$$\Delta = r^2+a^2+\frac{r^4}{2\alpha}\left(1-\sqrt{1+\frac{4\alpha}{r^3}\left(2M-\beta\ln\left(\frac{r}{\beta}\right)\right)}\right). \tag{1.52}$$

Here, a denotes the black hole spin parameter, defined as $a=\frac{J}{M}$, where J is the angular momentum and M is the mass of the black hole. For $a=0$, the metric (1.50) reduces to the static spherically symmetric solution (1.26), as shown in [44]. The constructed geometry (1.50) is therefore capable of describing rotating black holes in four-dimensional EGB gravity and is consistent with the parameter range relevant for black hole shadow studies motivated by EHT observations. In the limit where PFDM is absent and $\alpha\to 0$, the solution further reduces to the Kerr spacetime [79], while for $a=0$ it recovers the static metric (1.26).

The dependence of the event horizon radius on the black hole parameters is illustrated in Fig. 1.6. The results show that the horizon radius decreases as the parameters increase. In Fig. 1.7, the radial behavior of the function Δ is presented, which allows one to identify the extremal configurations for different parameter values. Finally, the region of allowed parameter space is summarized in Fig. 1.8.

1.2.3 Geodesics and circular photon orbits

We now turn to the study of particle motion in the spacetime (1.50) by analyzing its geodesic structure. In particular, our focus is on circular photon orbits, since these play a central role in determining the black hole shadow in four-dimensional EGB gravity. The trajectories of test particles can, in principle, be obtained directly from the geodesic equations; however, an equivalent and often more convenient approach is provided by the Hamilton-Jacobi (HJ) formalism. In this method, the dynamics are encoded in the HJ equation, which governs the

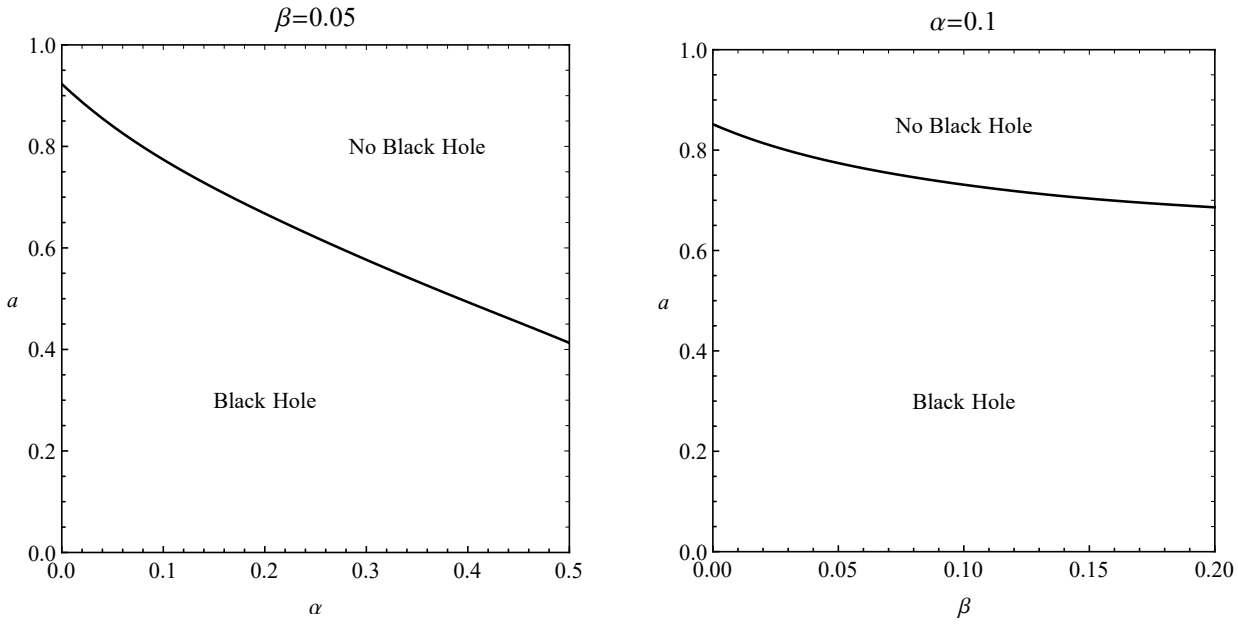


Figure 1.8: Parameter space regions indicating the existence of the event horizon for the NED black hole, with $M = 1$.

evolution of the particle action and can be written as:

$$\frac{\partial S}{\partial \lambda} = -\frac{1}{2} g^{\mu\nu} \frac{\partial S}{\partial x^{\mu}} \frac{\partial S}{\partial x^{\nu}}, \tag{1.53}$$

Similar to the Kerr geometry, the rotating black hole metric given in (1.50) possesses stationarity and axial symmetry. As a consequence of these spacetime symmetries, two constants of motion are preserved along geodesic trajectories, namely the energy E and the azimuthal angular momentum L of the particle.

$$-E = g_{t\mu}\dot{x}^{\mu}, \tag{1.54}$$

$$L = g_{\phi\mu}\dot{x}^{\mu}. \tag{1.55}$$

Subsequently, the Jacobi action can be expressed as

$$S = \frac{1}{2} m_p^2 \tau + S_r(r) + S_\theta(\theta) - Et + L\phi, \tag{1.56}$$

Here, m_p denotes the rest mass of the test particle. The functions $S_r(r)$ and $S_\theta(\theta)$ depend only on the radial coordinate r and the polar angle θ, respectively. Substituting the Jacobi action (1.56) into the Hamilton-Jacobi equation (1.53) yields

$$S_r(r) = \int^r \frac{\sqrt{\mathcal{R}(r)}}{\Delta(r)} dr, \tag{1.57}$$

$$S_\theta(\theta) = \int^\theta \sqrt{\Theta(\theta)} d\theta, \tag{1.58}$$

with

$$\mathcal{R} = \Big[(r^2+a^2)E - aL\Big]^2 - \Delta\Big[m^2r^2 + \mathcal{K} + (L-aE)^2\Big], \tag{1.59}$$

$$\Theta = \mathcal{K} + \cos^2\theta\left(a^2(E^2-m^2) - L^2\sin^{-2}\theta\right). \tag{1.60}$$

In this context, the Carter parameter $\mathcal{K}$, associated with the Killing-Yano tensor field, represents another constant of particle motion. By further integrating the relation $g_{\mu\nu}\dot{x}^\mu\dot{x}^\nu = -m_p^2$, we derive the following equation of motion for a particle within the framework of a rotating four-dimensional EGB black hole.

$$\rho^2\frac{dt}{d\lambda} = a(L - aE\sin^2\theta) + \frac{r^2+a^2}{\Delta}\Big(E(r^2+a^2) - aL\Big), \tag{1.61}$$

$$\rho^2\frac{dr}{d\lambda} = \pm\sqrt{\mathcal{R}}, \tag{1.62}$$

$$\rho^2\frac{d\theta}{d\lambda} = \pm\sqrt{\Theta}, \tag{1.63}$$

$$\rho^2\frac{d\phi}{d\lambda} = (L\csc^2\theta - aE) + \frac{a}{\Delta}\Big(E(r^2+a^2) - aL\Big). \tag{1.64}$$

We now focus on the examination of circular photon orbits by analyzing the radial motion. Considering the photon motion, we set $m_p^2 = 0$ in the subsequent analysis. The radial motion (1.62) can be reformulated as

$$\left(\rho^2\frac{dr}{d\lambda}\right)^2 + V_{eff} = 0. \tag{1.65}$$

The effective potential reads

$$V_{eff} = -\frac{((a^2+r^2)E - aL)^2 - \Delta(\mathcal{K} + (L-aE)^2)}{2r^4} \tag{1.66}$$

Here, $\xi = L/E$ and $\eta = \mathcal{K}/E^2$, while the function Δ is defined in Eq. (1.52). The plots shown in Fig. 1.9 depict the behavior of the effective potential V_{eff} as a function of the radial coordinate r for various choices of black hole parameters. By analyzing the peaks of these plotted curves, one can discern the unstable circular null orbits (Fig. 1.9).

The conditions for unstable circular photon orbits are given by

$$V_{eff} = 0, \quad \frac{\partial V_{eff}}{\partial r} = 0, \quad \frac{\partial^2 V_{eff}}{\partial r^2} < 0. \tag{1.67}$$

The last inequality guarantees the instability of the orbit. By solving these con-

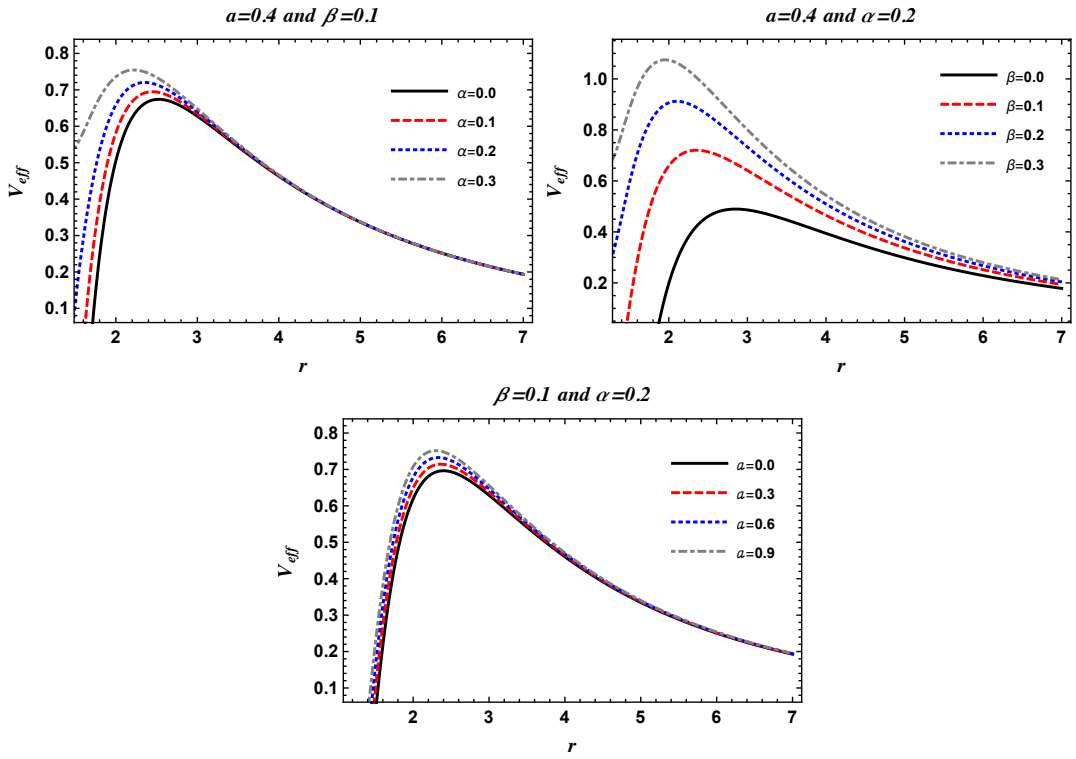


Figure 1.9: Radial behavior of the effective potential for selected values of the black hole parameters

ditions, one obtains [52]

$$\xi = \frac{\left(a^2+r^2\right)\Delta' - 4\Delta r}{a\Delta'}, \tag{1.68}$$

$$\eta = \frac{r^2\left(16\Delta\left(a^2-\Delta\right) - r^2\Delta'^2 + 8\Delta r\Delta'\right)}{a^2\Delta'^2}, \tag{1.69}$$

where the prime denotes differentiation with respect to r. Substituting these expressions into the instability condition (1.67) leads to the requirement that the radius of the unstable photon orbit satisfies

$$r + 2\frac{\Delta}{\Delta'^2}(\Delta' - r\Delta'') > 0, \tag{1.70}$$

where we have employed the condition $\Delta > 0$ beyond the event horizon. It is straightforward to check that this condition is fulfilled for the Schwarzschild black hole, obtained in the limit $a = \alpha = 0$, at the photon sphere radius $r = 3M$. Moreover, the same criterion can be verified numerically for the rotating EGB black hole in the presence of PFDM.

1.3 Four-dimensional Einstein-Gauss-Bonnet black hole in the Power-Yang-Mills field

In this section, we proceed to introduce further modifications to the Einstein-Gauss-Bonnet black hole solutions, aiming to explore new physical properties and extend the theoretical framework within dark matter contributions. Researchers across various domains of gravitational theories are particularly focused on the interaction between gravity and matter fields, with a specific emphasis on black hole physics, where black holes surrounded by different fields are examined. In four-dimensional EGB gravity, black hole solutions coupled to various matter fields have been extensively studied in the literature [80–84]. In many of these models, the resulting geometries exhibit a curvature singularity at the origin, which limits their physical applicability in describing the interior structure of black holes. To overcome this issue, nonlinear electromagnetic fields coupled to gravity have been introduced as a possible regularizing mechanism [85, 86]. Within this framework, a variety of black hole solutions have been obtained in four-dimensional EGB gravity sourced by nonlinear electrodynamics [87–90]. A well-known example is the static spherically symmetric EGB black hole coupled to the Born-Infeld nonlinear electromagnetic field [91]. In addition, couplings between non-Abelian Yang-Mills fields and both general relativity and Gauss-Bonnet gravity have also been explored in earlier works [92, 93]. For instance, within a nonlinear Yang-Mills framework characterized by the power-law invariant $(F^{(a)}_{\mu\nu}F^{\mu\nu(a)})^q$, Mazharimousavi and Halilsoy obtained higher-dimensional black hole solutions in Gauss-Bonnet gravity [94].

1.3.1 Static black hole

We provide a concise examination of the four-dimensional EGB black hole within the context of the power-Yang-Mills field. The action for Gauss-Bonnet gravity in D dimensions, when coupled with the PYM field, is expressed as [94,95]

$$S_G = \frac{1}{2}\int\left[R - \frac{\Lambda(D-2)(D-1)}{3} + \alpha\mathcal{L}_{GB} - \mathcal{F}^q\right]\sqrt{g}d^Dx. \tag{1.71}$$

In this context, Λ denotes the cosmological constant, R represents the scalar curvature and α is the Gauss-Bonnet parameter. In action (1.71) the GB Lagrangian is defined as

$$\mathcal{L}_{GB} = R^2 - 4R_{\gamma\zeta}R^{\gamma\zeta} + R_{\gamma\zeta\pi\sigma}R^{\gamma\zeta\pi\sigma}, \tag{1.72}$$

where $R_{\gamma\zeta\pi\sigma}$ and $R_{\gamma\zeta}$ represent the Riemann and Ricci tensors, respectively. Furthermore, in the action (1.71), the notation $\mathcal{F}$ denotes the YM invariant, which is articulated

$$\mathcal{F} = \sum_{a=1}^{\frac{(D-1)(D-2)}{2}} Tr\big(F^{(a)}_{\lambda\sigma} F^{\lambda\sigma(a)}\big), \tag{1.73}$$

with the parameter $q \in (0, \infty)$, which functions as the exponent of the YM charge. The expression for the YM field is represented as

$$F^{(a)}_{\gamma\zeta} = \partial_\gamma A^{(a)}_\zeta - \partial_\zeta A^{(a)}_\gamma + \frac{1}{2\sigma} C^{(a)}_{(b)(c)} A^{(b)}_\gamma A^{(c)}_\zeta, \tag{1.74}$$

The symbols $A^{(a)}_\zeta$ denote the Yang-Mills potentials associated with the gauge group $SO(D-1)$, while σ represents a constant value, and $C^{(a)}_{(b)(c)}$ are the structure constants of a Lie group G with $\frac{(D-2)(D-1)}{2}$ parameters. The action described in equation (1.71) delineates the potential interaction between modified gravity and the Yang-Mills field, incorporating power, within the context of a cosmological constant. Instead of employing a four-dimensional integral, a D-dimensional integral is utilized, as the black hole solution required is derived through a dimensional regularization process from the existing method for D-dimensional Gauss-Bonnet black holes. The equations of motion for the potentials $A^{(a)}_\mu$ and the metric tensor $g_{\mu\nu}$ can be expressed as

$$d\big({}^*\mathbf{F}^{(a)}\mathcal{F}^{q-1}\big) + \frac{1}{\sigma} C^{(a)}_{(b)(c)} \mathcal{F}^{q-1}\big(\mathbf{A}^{(b)} \wedge \mathbf{F}^{(c)}\big) = 0, \tag{1.75}$$

$$G_{\mu\nu} + \frac{(D-2)(D-1)}{3}\Lambda g_{\mu\nu} + \alpha H_{\mu\nu} = T_{\mu\nu}, \tag{1.76}$$

the symbols * and $\wedge$ denote duality and the wedge product, respectively. Furthermore, $G_{\mu\nu}$, $H_{\mu\nu}$, and $T_{\mu\nu}$ represent the Einstein, Lanczos, and energy-momentum tensors, respectively. The specific formulations for these tensors are as follows:

$$G_{\mu\nu} = R_{\mu\nu} - \frac{1}{2} g_{\mu\nu} R, \tag{1.77}$$

$$H_{\mu\nu} = 2\big(RR_{\mu\nu} - 2R_{\mu\sigma}R^\sigma_\nu - 2R^{\sigma\delta}R_{\mu\sigma\nu\delta} + R^{\sigma\delta\lambda}_\mu R_{\nu\sigma\delta\lambda}\big) - \frac{1}{2} g_{\mu\nu}\mathcal{L}_{\mathcal{GB}}, \tag{1.78}$$

$$T^\mu_\nu = 2q\mathcal{F}^{q-1} Tr\big(F^{(a)}_{\nu\delta} F^{\mu\delta(a)}\big) - \frac{1}{2}\delta^\mu_\nu \mathcal{F}^q. \tag{1.79}$$

The magnetic Wu-Yang ansatz [92,93,96] can be applied to the YM field, allowing the one-forms for the YM magnetic potential to be expressed as

$$\mathbf{A}^{(a)} = \frac{Q}{r^2}\big(x_i dx_j - x_j dx_i\big), \tag{1.80}$$

where $r^2 = \sum_{p=1}^{D-1} x_p^2$. The variables a, i, and j are defined within the ranges $2 \leq 2a \leq (D-1)(D-2)$ and $1 \leq j \leq i-1 \leq D-2$. Additionally, the YM magnetic charge is denoted by Q. The general metric in D dimensions is

$$g_{\gamma\zeta}dx^{\gamma}dx^{\zeta} = -f(r)dt^2 + f(r)^{-1}dr^2 + r^2\big(h_{rs}dx^r dx^s\big), \tag{1.81}$$

The expression $h_{rs}dx^r dx^s$ denotes the geodesic distance between two points on a $(D-2)$-dimensional hypersphere. By modifying α to $\frac{\alpha}{D-4}$ and examining the limit as D approaches 4, the black hole solution is obtained, with the metric function articulated as

$$f(r) = 1 + \frac{r^2\left[1 \pm \sqrt{1 + 2\alpha\left(\frac{4M}{r^3} - \frac{(2Q^2)^q}{(4q-3)r^{4q}}\right)}\right]}{2\alpha}. \tag{1.82}$$

In the BH solution (1.82), it is crucial to observe that we have set $\Lambda = 0$. The metric function (1.82) presents two solution branches. However, we concentrate exclusively on the $-$ branch, as the solution corresponding to the $+$ sign lacks a physical interpretation. Furthermore, when $q = 1$, the black hole solution transforms into

$$f(r) = 1 + \frac{r^2\left[1 \pm \sqrt{1 + \frac{4\alpha}{r^3}\left(2M - \frac{Q^2}{r}\right)}\right]}{2\alpha}. \tag{1.83}$$

The solution given in (1.83) coincides with the black hole geometry obtained by Fernandes [97], except that in the present case the parameter Q represents the electric charge rather than the Yang-Mills magnetic charge. In the limit $Q = 0$, the metric naturally reduces to the four-dimensional EGB black hole solution introduced by Glavan and Lin [44].

$$f(r) = 1 + \frac{r^2}{2\alpha}\left[1 \pm \sqrt{1 + \frac{8\alpha M}{r^3}}\right]. \tag{1.84}$$

For $\alpha \to 0$, we obtain the standard BH solution [94]

$$f(r) = 1 - \frac{2M}{r} + \frac{2^{q-1}Q^{2q}}{(4q-3)r^{4q-2}}, \tag{1.85}$$

We can confirm that the metric (1.82) becomes asymptotically flat when $q > \frac{1}{2}$ and $q \neq \frac{3}{4}$. Therefore, we focus on those q values where the black hole solution

in question is asymptotically flat. Following this, we conduct an analysis of the photon sphere's radius. To do so, we require the condition

$$\left[\frac{d}{dr}\big(\varrho(r)\big)\right]_{r=r_{ph}} = 0, \tag{1.86}$$

with

$$\varrho(r) = \frac{g_{22}}{g_{00}} = \frac{r^2}{f(r)}. \tag{1.87}$$

The variation in the radius r_{ph} of the photon sphere is illustrated in relation to the GB parameter α, power q, and YM charge Q in Fig. 1.10. The upper panel presents the graphs of photon radius as a function of α, where Q varies for each curve in the left and middle plots with a constant q. Conversely, the right plot maintains a constant Q while varying q for each curve. The graphs demonstrate that as α increases, the size of the photon sphere decreases across all curves in the panel. Notably, in the middle plot, the reduction in the photon sphere's size occurs more rapidly compared to the other plots. In the middle panel, the graphs for r_{ph} versus Q are shown, with α variation for different curves in the left and middle plots while q remains fixed. In the right plot, both q and α are constant. It is evident that in the left plot, the photon sphere enlarges as Q increases, whereas in the middle plot, its size decreases with an increase in Q. As the parameter α grows, the curves in the left plot expand, while those in the right plot contract. The right plot stands out from the others observed so far. For $q < \frac{3}{4}$, the photon sphere's size increases, and for $q > \frac{3}{4}$, it decreases as Q rises. Furthermore, when $Q = 0$, the curves intersect at a constant r_{ph} value, it is indicative of the uncharged EGB black hole. For $q < \frac{3}{4}$, the size of the photon sphere increases more rapidly as q rises, with Q held constant. Conversely, for $q > \frac{3}{4}$, the size of the photon sphere diminishes more swiftly as q increases, again with Q fixed. In the lower panel, r_{ph} is plotted against q for curves associated with the parameter α with fixed Q on the left plot and for curves associated with the parameter Q with fixed α on the right plot. A discontinuity is observed in the r_{ph} curves as q approaches $\frac{3}{4}$ across the entire panel. However, moving away from the value of $q = \frac{3}{4}$, the radius stabilizes and remains nearly constant. In the left plot, r_{ph} increases sharply as q approaches $\frac{3}{4}^-$, while r_{ph} approaches zero as q nears $\frac{3}{4}^+$ for all α values.

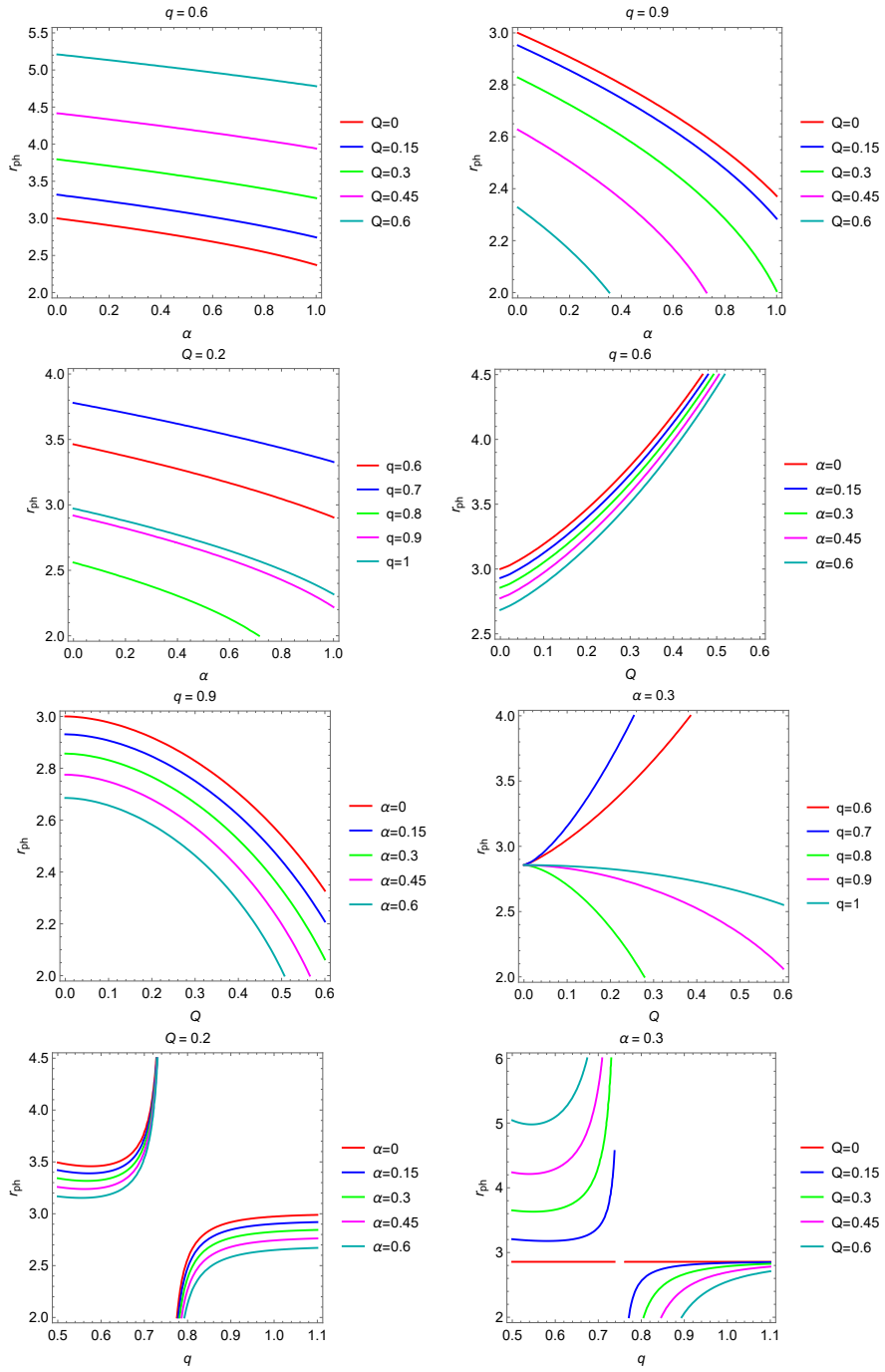


Figure 1.10: Plots illustrating the dependencies of the photon sphere radius on the black hole parameters q, Q, and α.

1.3.2 Rotating black hole

We applied the Newman-Janis algorithm [72, 73] and obtained the following spacetime metric for a rotating black hole:

$$\begin{aligned} ds^2 &= \frac{a^2\sin^2\theta-\Delta(r)}{\rho^2}dt^2+\frac{\rho^2}{\Delta(r)}dr^2+\rho^2d\theta^2-\frac{\Delta(r)a^2\sin^4\theta-\left(r^2+a^2\right)^2\sin^2\theta}{\rho^2}d\phi^2 \\ &\quad -\frac{2a\sin^2\theta\left(a^2+r^2-\Delta(r)\right)}{\rho^2}dtd\phi, \end{aligned} \tag{1.88}$$

where

$$\Delta(r) = a^2+r^2f(r) = a^2+r^2+\frac{r^4\left[1\pm\sqrt{1+2\alpha\left(\frac{4M}{r^3}-\frac{(2Q^2)^q}{(4q-3)r^{4q}}\right.}\right]}{2\alpha}, \tag{1.89}$$

$$\rho^2 = r^2+a^2\cos^2\theta. \tag{1.90}$$

It is crucial to acknowledge that the rotating black hole solution (1.88) may not entirely conform to the original Einstein Field Equations due to the possible emergence of additional sources. However, the black hole solution (1.88) can be interpreted as a regularized four-dimensional EGB black hole solution with a power-Yang-Mills field associated with an unknown field equations (1.76). Furthermore, in the absence of spin, the metric (1.88) is reduced to its static form (1.82). As in $\alpha \to 0$, the Kerr black hole solution is derived analogously to the Schwarzschild black hole solution for non-rotating cases. Therefore, the metric solution (1.88) can be interpreted as a viable rotating black hole metric.

We next analyze the horizon structure of the rotating black hole metric (1.88) by determining the roots of the equation $\Delta(r) = 0$. To study the behavior of the horizon radius r_h as a function of the spin parameter a, the equation is solved. The results are presented in Fig. 1.11. The plots indicate that increasing the rotation parameter causes the event horizon (EH) to shrink, whereas the Cauchy horizon (CH) moves outward for all parameter configurations considered. In the upper panel, the curves correspond to different values of the charge parameter Q while keeping q and α fixed. In the left panel, larger values of Q shift the curves toward larger radii, whereas the opposite behavior is observed in the right panel, where the curves move inward as Q increases. As a consequence, the extremal value of the spin parameter a increases with Q in the left plot, while it decreases with Q in the right plot. Furthermore, in the context of slow rotation, the CH exhibits minimal variation within Q the plot on the left. The curves in the middle panel represent α for the constant Q and q. It is observed that as α increases, the

size of the EH decreases while the CH enlarges in both plots. Thus, the extremal spin values decrease with respect to α in both plots. This illustrates how the curves for $q < \frac{3}{4}$ are distinguished from those for $q > \frac{3}{4}$. The lower panel plot displays curves for different q values with fixed Q and α. It is evident that the curves expand as q approaches $\frac{3}{4}$ and for $q > \frac{3}{4}$.

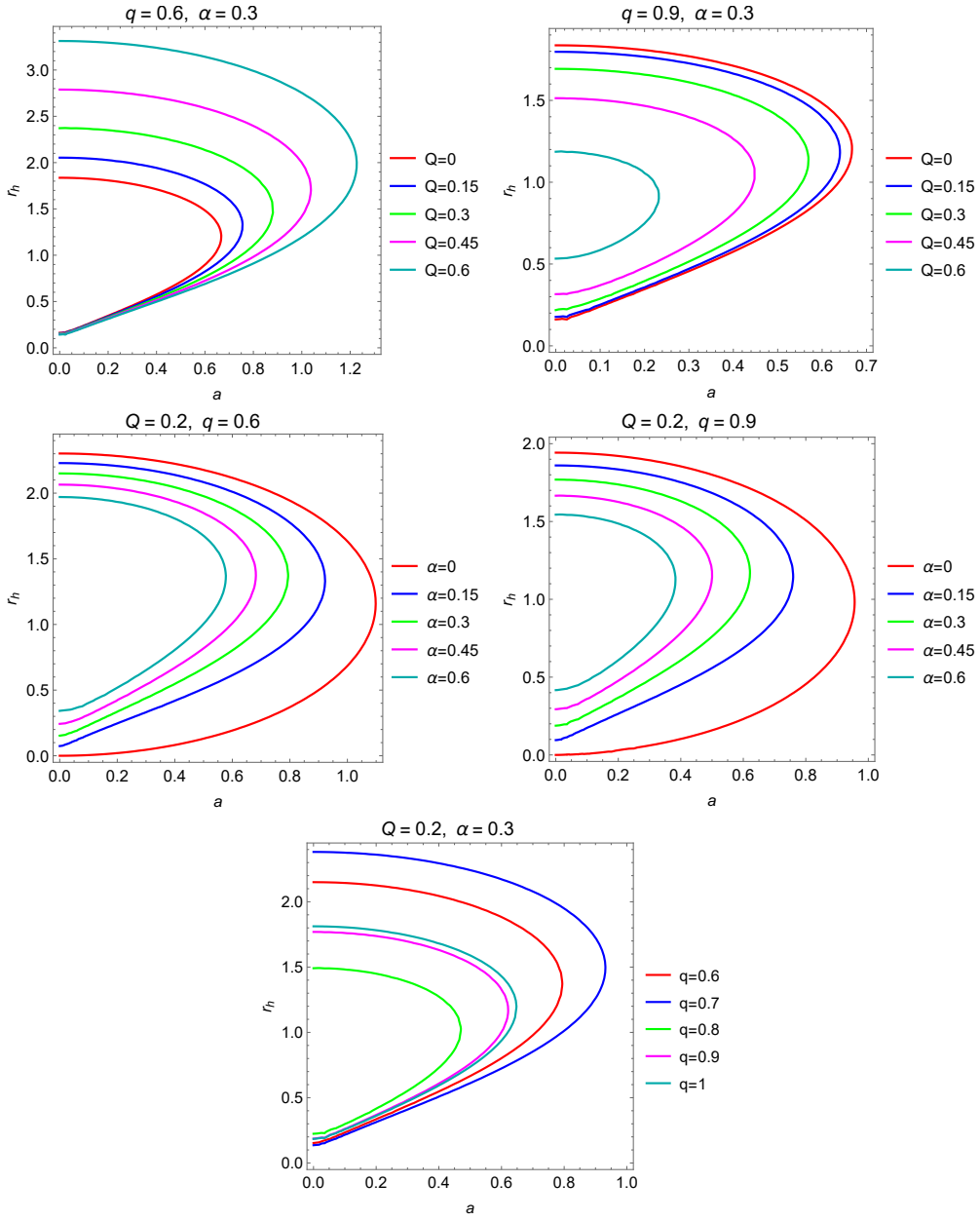


Figure 1.11: Variation of the horizon radius with the spin parameter a for different values of q, Q, and α.

1.3.3 Photon motion

We now proceed to analyze the effective potential associated with rotating black holes in four-dimensional EGB gravity coupled to the power Yang-Mills field. To carry out this study, it is necessary to obtain the corresponding geodesic equations, which can be derived through the HJ formalism [98]. Within this framework, the particle dynamics are described by the following tensorial form of the Lagrangian:

$$\mathcal{L} = \frac{1}{2} g_{\mu\nu} \dot{x}^{\mu} \dot{x}^{\nu}. \tag{1.91}$$

The generalized canonical momenta associated with the spacetime coordinates are defined as

$$p_{\mu} = g_{\mu\nu} \dot{x}^{\nu}. \tag{1.92}$$

Using the Lagrangian, the generalized momenta, and the metric coefficients from Eqs. (1.91), (1.92), and (1.89), one obtains two conserved quantities which are E and L. Their explicit forms are given by

$$E = -\frac{\partial \mathcal{L}}{\partial \dot{t}} = p_t, \tag{1.93}$$

$$L = \frac{\partial \mathcal{L}}{\partial \dot{\phi}} = p_{\phi}, \tag{1.94}$$

Here, $\dot{x} = \frac{\partial x}{\partial \tau}$, with τ denoting the affine parameter along the particle trajectory. The corresponding Hamilton-Jacobi equation can be written

$$2\frac{\partial \mathcal{S}}{\partial \tau} + g^{\mu\nu} \frac{\partial \mathcal{S}}{\partial x^{\mu}} \frac{\partial \mathcal{S}}{\partial x^{\nu}} = 0, \tag{1.95}$$

such that $\mathcal{S}$ can be taken as

$$\mathcal{S} = \frac{1}{2} m_p \tau - Et + L\phi + \mathcal{S}_r(r) + \mathcal{S}_{\theta}(\theta), \tag{1.96}$$

Here, m_p represents the mass of the test particle, while $\mathcal{S}_r(r)$ and $\mathcal{S}_{\theta}(\theta)$ are functions depending only on r and θ, respectively. Substituting Eq. (1.96) into Eq. (1.95) and applying the standard separation of variables procedure [98], one obtains the equations governing null geodesics ($m_p = 0$) in the following form:

$$\rho^4 \dot{t}^2 = \left[\frac{E\left(r^2 + a^2\right)^2 - aL\left(r^2 + a^2\right)}{\Delta} + a \sin^2\theta \left(L \csc^2\theta - aE \right) \right]^2, \tag{1.97}$$

$$\rho^4 \dot{r}^2 = \mathcal{R}, \tag{1.98}$$

$$\rho^4 \dot{\theta}^2 = \Theta, \tag{1.99}$$

$$\rho^4 \dot{\phi}^2 = \left[\frac{aE\left(r^2 + a^2\right) - La^2}{\Delta} + \left(L \csc^2\theta - aE \right) \right]^2, \tag{1.100}$$

where

$$\mathcal{R}(r) = \big(aL - (a^2 + r^2)E\big)^2 - \Delta\mathcal{K} - \Delta(aE - L)^2, \tag{1.101}$$

$$\Theta(\theta) = \cot^2\theta\big(a^2E^2\sin^2\theta - L^2\big) + \mathcal{K}, \tag{1.102}$$

where $\mathcal{K}$ denotes the Carter constant, while the combination $\mathcal{K} + (aE - L)^2$ corresponds to the modified Carter constant. For an observer located in the equatorial plane $\big(\theta = \frac{\pi}{2}\big)$, the effective potential can be obtained from the radial geodesic equation, which takes the form

$$V_{eff} = -\frac{\mathcal{R}(r)}{2r^4}. \tag{1.103}$$

Figure 1.12 presents the radial behavior of the effective potential V_{eff} for several choices of the parameters α, q, and Q. The upper panel illustrates the influence of the charge parameter Q while keeping a, q, and α fixed. In the left plot, increasing Q lowers the maximum of the effective potential and simultaneously shifts the peak away from the event horizon. This indicates that the corresponding unstable circular photon orbits occur at larger radii and lower potential values. In contrast, the right plot exhibits the opposite tendency, where larger values of Q move the unstable orbits closer to the black hole and increase the corresponding peak values of the potential. The middle panel displays the effect of varying the Gauss–Bonnet coupling parameter α for fixed values of a, q, and Q. In both cases, increasing α causes the unstable circular orbits to move inward while the associated peaks of the effective potential become higher. A noticeable distinction appears between the left and right plots: in the right plot, the minima of the peaks remain above $V_{eff} = 2$, whereas in the left plot the peaks approach this value. This behavior naturally separates the parameter regimes corresponding to $q < \frac{3}{4}$ and $q > \frac{3}{4}$. A qualitatively similar behavior is observed in the third panel when the spin parameter a is varied. As the black hole rotation increases, the unstable circular orbits shift toward the horizon and occur at larger values of the effective potential. The distinction between the two intervals $q < \frac{3}{4}$ and $q > \frac{3}{4}$ remains clearly visible in this case as well. Finally, the bottom panel shows the dependence of the effective potential on the parameter q while the remaining parameters are held fixed. Increasing q within the intervals $(0.5, 0.75)$ and $(0.75, \infty)$ decreases the height of the potential peaks, leading to smaller unstable circular orbits. Owing to the singular behavior of the metric function at $q = 0.75$, the corresponding curves in these two regions remain disconnected from one another.

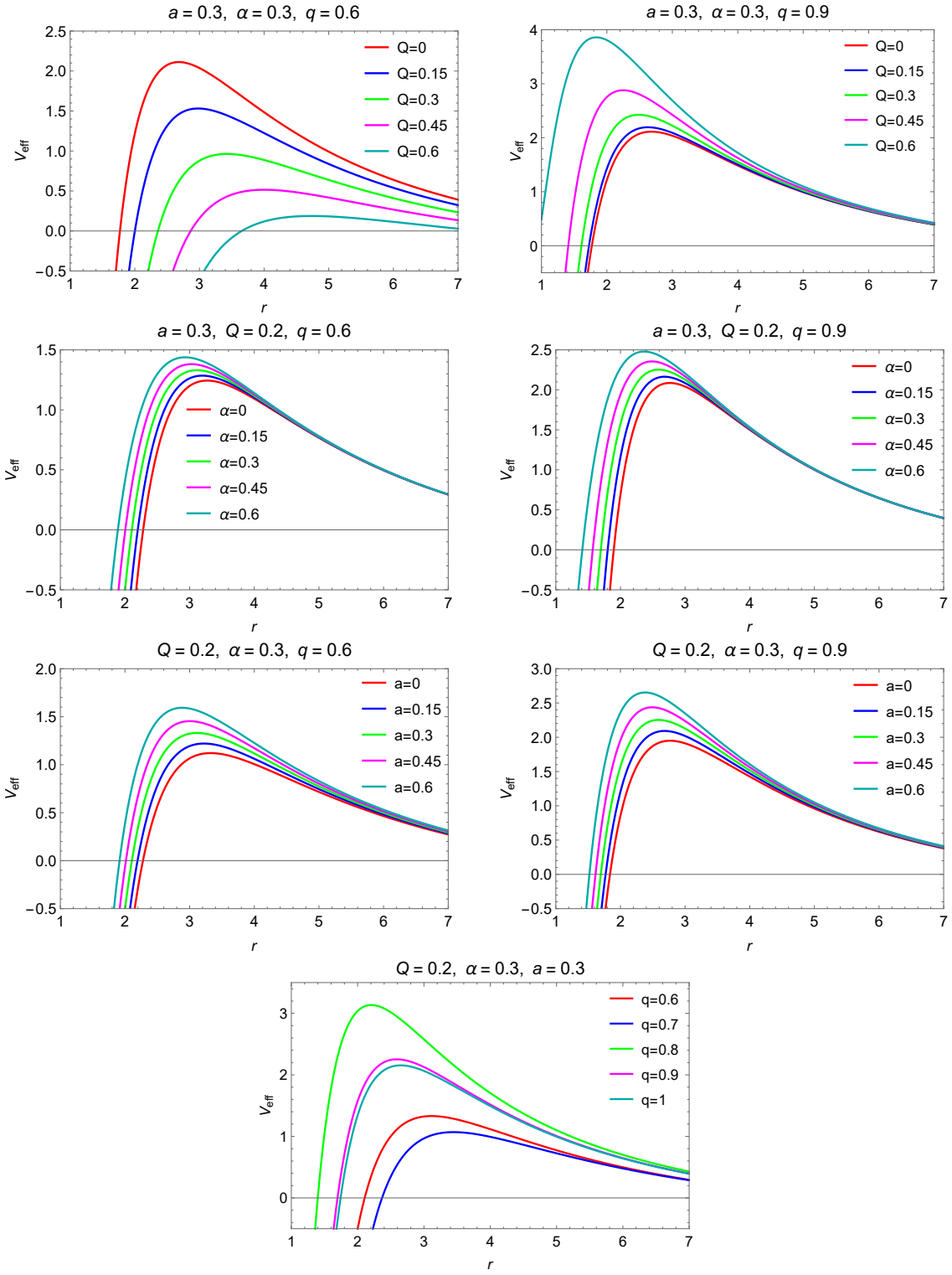


Figure 1.12: Radial profiles of the effective potential $V_{\text{eff}}(r)$ illustrating how it changes under variations of the black hole parameters q, Q, and α.

1.4 Conclusions

In this chapter, new classes of black hole solutions were obtained and analyzed within the framework of extended gravitational theories.

- Firstly, we reviewed a novel class of charged black hole solutions arising from Einstein gravity coupled to a nonlinear electrodynamics model that smoothly interpolates between Maxwell theory and genuinely nonlinear regimes through the parameter b. Although the solution is not regular, its horizon structure and parameter space reveal rich phenomenology, with the charge q playing a dominant role in shrinking the event horizon and the nonlinear effects becoming prominent in the small-b regime. Furthermore, by employing the effective geometry formalism for photon propagation in NED, we showed that nonlinear electromagnetic interactions modify the photon sphere and, consequently, observable optical properties such as the black hole shadow. In particular, increasing q leads to a decrease in the photon sphere radius, while the influence of b becomes appreciable only at sufficiently large charge.

- Secondly, rotating black hole solutions were obtained for a 4D EGB gravity model surrounded by perfect fluid dark matter. The influence of additional parameters introduced by these extended theories on the black hole geometry and photon dynamics was examined in detail. The geometry of a rotating black hole in four-dimensional EGB gravity is modified by the presence of both the Gauss-Bonnet coupling parameter α and the dark matter parameter β, leading to deviations from the standard Kerr spacetime. As a consequence, the corresponding horizon structure becomes considerably richer and allows one to investigate the combined effects of higher-curvature corrections and surrounding dark matter on rotating black holes. The analysis shows that increasing either α or β tends to decrease the horizon radius, thereby altering the overall black hole geometry.

- Then, the modified Newman-Janis algorithm was employed to extend the static black hole solution in 4D EGB gravity coupled to the PYM field into its rotating counterpart. After constructing the rotating geometry, we analyzed the properties of the photon sphere for the static configuration and examined the behavior of the horizon radius in the rotating case. As the spin increases toward its extremal value, the event horizon decreases while the CH increases for all cases. The effect of the total charge Q varies with the parameter q: for $q < 0.75$, increasing Q causes EH to grow; for $q > 0.75$, EH decreases. The CH remains nearly constant for $q < 0.75$ but increases for $q > 0.75$.

Increasing the GB parameter α shifts the horizons inward, reducing the EH and enlarging the CH. The parameter q has a stronger influence on the EH than on the CH. In all scenarios, no central singularity is observed. From the effective potential plots, it is observed that unstable circular orbits expand with increasing Q when $q < 0.75$, but shrink when $q > 0.75$, due to the dependence of Q on the power parameter q. Additionally, an overall enlargement of the unstable orbits is seen in both intervals of q.

Chapter 2

Black hole shadows in extended theories of gravity

2.1 Shadows and observables of four-dimensional Einstein-Gauss-Bonnet black hole in perfect fluid dark matter

2.1.1 Nonrotating black hole shadows

The shadow of a black hole appears as a dark silhouette produced by photons that are captured by the event horizon, surrounded by a luminous ring generated by strongly lensed photons escaping toward distant observers [99–101]. Observations of this shadow carry important information about the gravitational field in the vicinity of the black hole and the structure of the surrounding spacetime. In the present study, we investigate how PFDM modifies the shadow properties of black holes in four-dimensional Einstein-Gauss-Bonnet gravity. Early studies of black hole shadows were initiated by Synge [100] and later extended by Luminet [101]. Their analyses established a method for evaluating the angular size of the photon capture region around a Schwarzschild black hole by identifying the divergence of the light deflection angle. In particular, the Synge approach determines the photon sphere from null trajectories and relates the corresponding impact parameter to the angular radius of the shadow [100, 102], which can be expressed as

$$\sin^2 X_s = \frac{h(r_{ph})^2}{h(r_o)^2}, \tag{2.1}$$

Here, the function $h(r)$ is defined as $h(r) = r^2/f(r)$, where X_s denotes the angular radius of the black hole shadow, r_o is the radial position of the observer, and r_{ph} represents the radius of the photon sphere. In the limit of a distant observer,

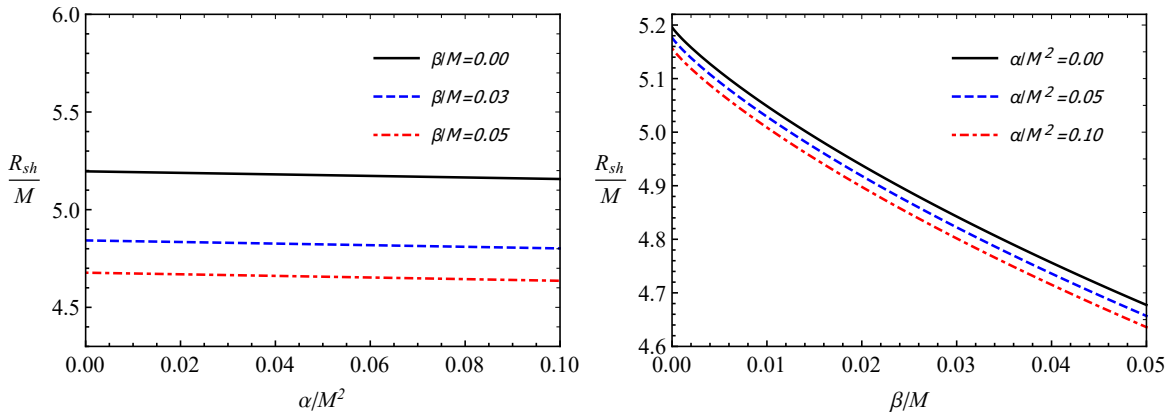


Figure 2.1: The shadow radius of 4D EGB black hole in PFDM in the case of static metric.

Eq. (2.1) reduces to the following simplified form:

$$\sin^2 X_s = \frac{r_{ph}^2}{f(r_{ph})}\frac{f(r_o)}{r_o^2}. \tag{2.2}$$

In the limit of a distant observer, the linear (or physical) radius of the black hole shadow can be determined from Eq. (2.2) as

$$R_{sh} = r_o \sin X_s = \frac{r_{ph}}{\sqrt{f(r_{ph})}}, \tag{2.3}$$

Finally, Eq. (2.3) provides the expression for the black hole shadow in the non-rotating case.

For the static, spherically symmetric four-dimensional EGB black hole immersed in PFDM, the resulting shadow remains perfectly circular. However, its size is affected by the PFDM parameter β, with larger values of β leading to a reduction in the shadow radius. Consequently, non-rotating EGB black holes surrounded by PFDM cast smaller shadows compared to the case without PFDM, as shown in Fig. 2.1. For rotating configurations, the shadow structure becomes dependent on the parameters a, α, and β. As illustrated in Fig. 2.1, the presence of rotation breaks the circular symmetry, producing a distorted shadow shape. In this case as well, the PFDM parameter β plays a dominant role, reducing both the size and symmetry of the shadow as its value increases. The same figure further demonstrates the dependence of the shadow radius on both the Gauss-Bonnet coupling and PFDM parameters. While variations in α produce only mild changes in the shadow size, the influence of β is significantly more pronounced, leading to a clear decrease in the observed radius. Overall, the Synge-based approach provides a transparent framework for analyzing how PFDM and higher-curvature corrections modify black hole shadow observables, as summarized in Fig. 2.1.

2.1.2 Rotating black hole shadows

In his seminal work, Bardeen [99] first studied the shadow of the Kerr black hole and showed that rotation leads to a deformation of its otherwise circular shape. The surrounding photon ring is determined by the underlying spacetime geometry, making both the size and distortion of the shadow valuable probes of black hole parameters and the gravitational field near the event horizon. Over the years, a large body of analytical, numerical, and observational research has been devoted to black hole shadows [103–111], including studies aimed at constraining black hole parameters and testing alternative theories of gravity [12, 112–114]. In this work, we focus on how perfect fluid dark matter influences the shadow of rotating EGB black holes. We assume that the radiation sources are uniformly distributed at spatial infinity in all directions and that the observer is also located at infinity, which simplifies the analysis of the shadow geometry.

The shadow of a black hole is commonly characterized in terms of two celestial coordinates, denoted by μ and λ [99–101, 108]. These coordinates are defined on the observer's sky and describe the apparent position of the photon trajectories forming the shadow on the celestial sphere. In particular, μ represents the horizontal displacement of the shadow image, corresponding to variations in the azimuthal direction ϕ, and is measured from the center of the shadow. Similarly, λ describes the vertical displacement, associated with changes in the polar angle θ, and also measured relative to the shadow center. In order to analyze the shadow within the present framework, it is convenient to introduce these two celestial coordinates [108]:

$$\mu = \lim_{r\to\infty}\left(-r^2\sin\theta\frac{d\phi}{dr}\bigg|_{\theta\to\theta_0}\right) = -\xi\csc\theta_0, \tag{2.4}$$

$$\lambda = \lim_{r\to\infty}\left(r^2\frac{d\theta}{dr}\bigg|_{\theta\to\theta_0}\right) = \pm\sqrt{\eta + a^2\cos^2\theta_0 - \xi^2\cot^2\theta_0}, \tag{2.5}$$

Here, the equations of motion (1.61)-(1.64) have been used, and θ_0 denotes the inclination angle of the observer. In the special case where the observer is located on the equatorial plane, these celestial coordinates reduce to:

$$\mu = -\xi \tag{2.6}$$

$$\lambda = \pm\sqrt{\eta}. \tag{2.7}$$

The black hole shadow is obtained by constructing a parametric curve in the celestial plane (μ, λ) using the relations (1.68) and (1.69). In this representation, the radial coordinate r serves as the parameter that traces the trajectory of photon

orbits. The resulting region corresponds to the absence of light rays reaching the observer, thereby forming the shadow. Consequently, the boundary of the shadow is fully determined by the properties of circular photon orbits and, in particular, by the photon sphere radius.

The shadow profiles of four-dimensional EGB black holes for different parameter values are presented in Fig. 2.2. From these results, it is observed that both the Gauss-Bonnet coupling and the dark matter parameter lead to a reduction in the overall size of the shadow. In addition, when the spin parameter takes larger values, the shadow deviates from circularity and exhibits noticeable distortions, as expected for rotating metrics.

2.1.3 Parameter estimation

The physical properties of black holes can, in principle, be inferred from the analysis of their shadows. For this purpose, one needs to identify suitable observables that quantify both the size and shape of the shadow image. In general, spherically symmetric black holes produce perfectly circular shadows, whereas axially symmetric spacetimes typically lead to deformed, non-circular silhouettes due to rotation. A commonly used characterization was introduced by Hioki and Maeda [108], who defined two quantities describing the shadow: a characteristic radius encoding its overall size and a distortion parameter measuring deviations from circularity. In addition to this approach, alternative coordinate-independent methods have also been developed, where the shadow is described using quantities such as its area and oblateness [112, 115]. These observables provide a practical way to quantify deviations in the shadow geometry. In this context, the shadow area A and the oblateness D are directly related to the deformation and anisotropy of the shadow boundary [112].

$$A = 2\int_{r_-}^{r_+}\left(\lambda(r)\frac{d\mu(r)}{dr}\right)dr, \tag{2.8}$$

$$D = \frac{\Delta\mu}{\Delta\lambda}, \tag{2.9}$$

Here, $r_\pm$ denote the radii of the circular photon orbits, which are obtained by solving the condition $\eta_c = 0$.

We now turn to the analysis of shadow observables associated with the rotating four-dimensional EGB black hole. To simplify the investigation, one of the black hole parameters is kept fixed. Accordingly, we consider three distinct cases in order to study the behavior of the shadow characteristics under different parameter choices:

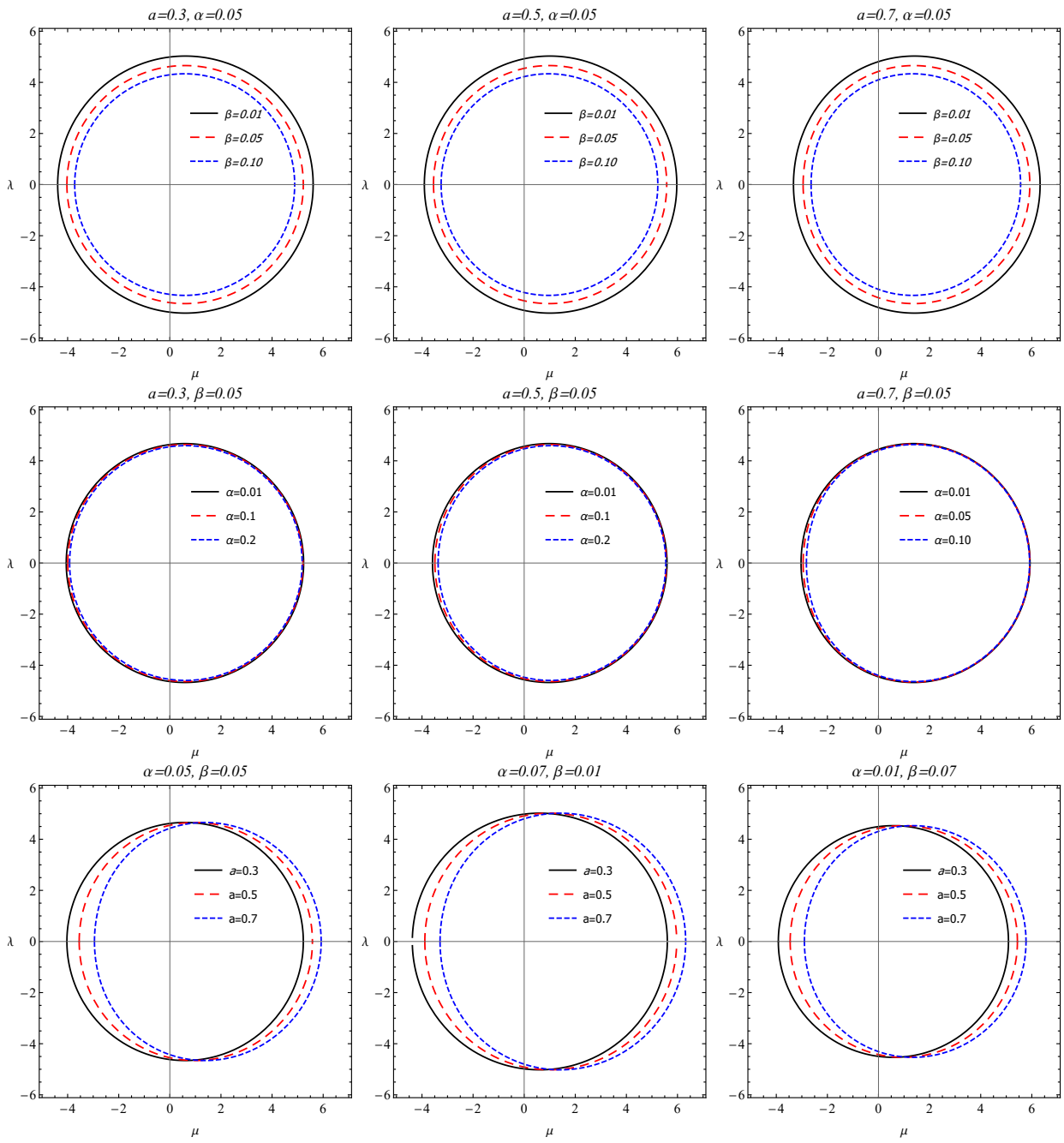


Figure 2.2: Shadow images of the rotating 4D EGB black hole in PFDM corresponding to different parameter cases.

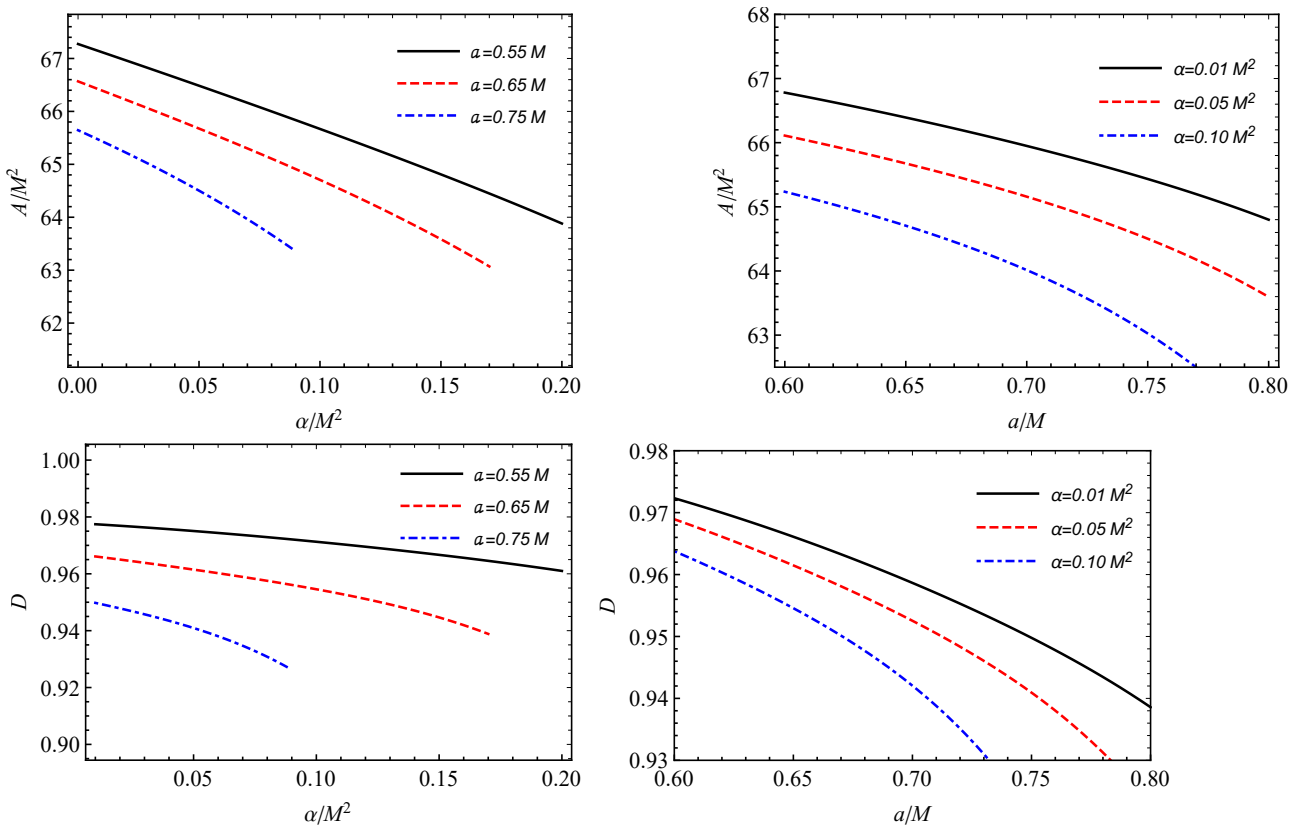


Figure 2.3: Case 1, area and oblateness, $\beta = 0.05M$

- Case 1: $\beta = 0.05M$,
- Case 2: $\alpha = 0.1M^2$,
- Case 3: $a = 0.6M$.

The shadow area and oblateness were evaluated numerically for each case, allowing us to estimate the dependence of these observables on the black hole parameters. The corresponding results are presented in Figs. 2.3–2.5, which illustrate how the shadow characteristics vary with the parameters of the rotating four-dimensional EGB black hole. From these figures, it is observed that increasing the values of a, α, and β generally leads to a reduction in both the shadow area and the oblateness across all considered scenarios. In particular, the PFDM parameter β has a more pronounced effect on the shadow area compared to the Gauss-Bonnet parameter α and the spin parameter a. It is also noted that as the ratio a/M approaches unity, the oblateness decreases, indicating a more pronounced deviation from circular symmetry and thus a stronger deformation of the shadow shape.

The parameter estimation for each case is illustrated through contour plots of the black hole parameters in Fig. 2.6. These plots indicate that the intersection

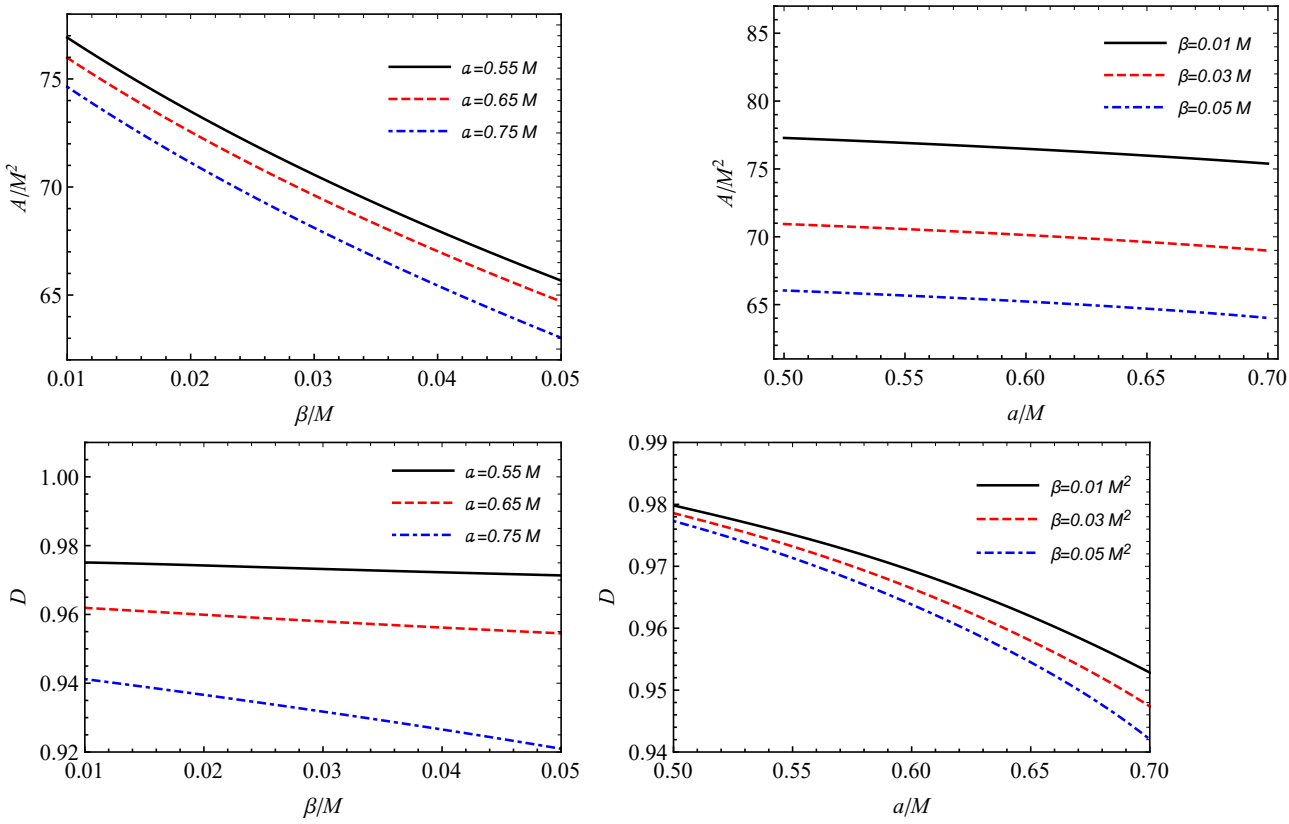


Figure 2.4: Case 2, area and oblateness, $\alpha = 0.1M^2$

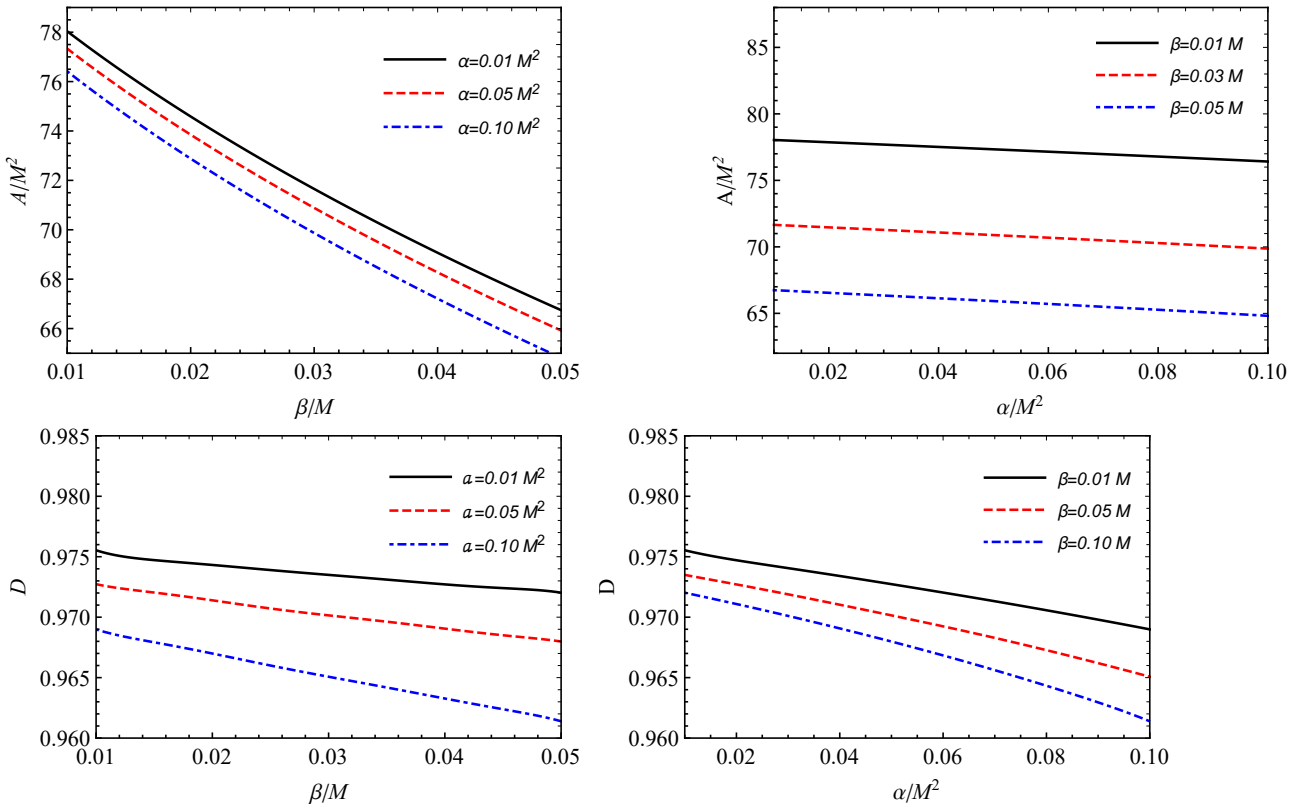


Figure 2.5: Case 3, area and oblateness, $a = 0.6M$

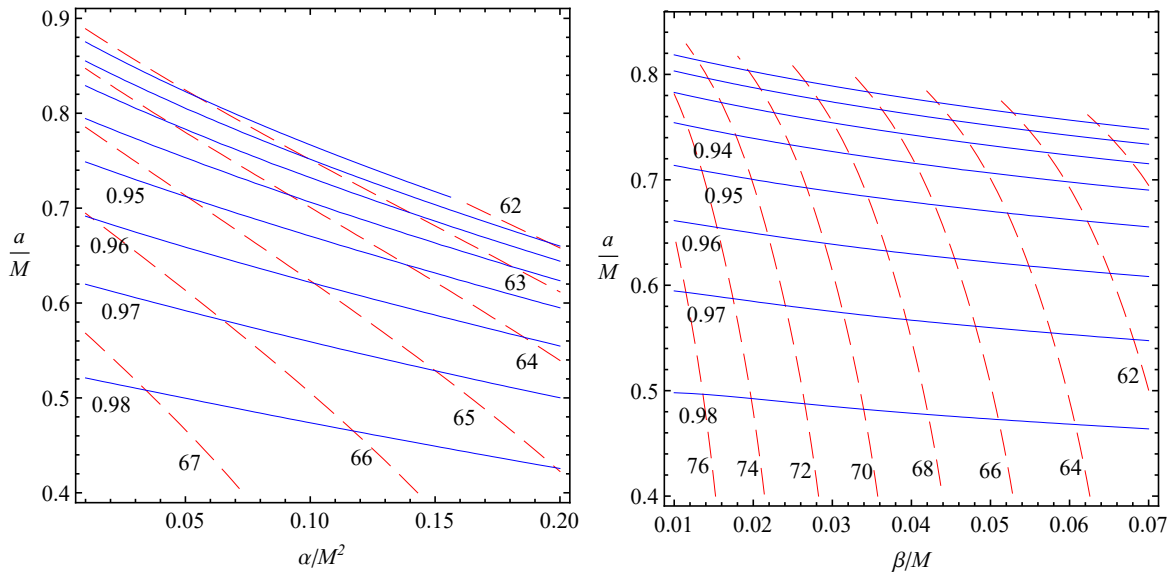


Figure 2.6: The contour plots of the observables A/M^2 and D for the rotating 4D EGB BH surrounded by PFDM in selected parameter ranges. $\beta = 0.05M$ on the left panel and $\alpha = 0.1M^2$ on the right panel. The dashed red and solid blue curves correspond to the constant values of the shadow area and oblateness parameters, respectively.

points of the contour lines provide a unique mapping to the corresponding pairs of black hole parameters in each scenario. In this way, the shadow observables can be used as an effective tool to infer the underlying black hole parameters. To support these results, numerical values are also summarized in Tables 2.1 and 2.2, which further clarify the accuracy of the proposed estimation procedure. Overall, the findings suggest that shadow-based measurements can serve as a powerful diagnostic for extracting information about black hole parameters from observational data. In a broader context, this approach may also be useful for studying black hole properties such as their formation, evolution, and interaction with surrounding matter fields. Beyond astrophysical applications, the method may additionally provide insights into testing general relativity and exploring possible deviations from standard gravitational theory.

2.2 Black hole shadow in nonlinear electrodynamics

The black hole shadow refers to the dark region seen against a bright background, which arises from the strong gravitational deflection and capture of photons in the vicinity of the event horizon. Within general relativity combined with linear electrodynamics, the boundary of this shadow is determined by the unstable circular photon orbits of the underlying spacetime geometry. However, in the presence of NED, photon propagation is modified and must be analyzed using the

A/M^2	D	a/M	α/M^2	R_a
68	0.99	0.3868	0.0028	4.6524
67	0.98	0.5081	0.0342	4.6180
66	0.97	0.5819	0.0651	4.5835
65	0.96	0.6207	0.1016	4.5486
64	0.95	0.6404	0.1386	4.5135
63	0.94	0.6384	0.1810	4.4781

Table 2.1: Numerical values of the black hole parameters a/M and α/M^2 estimated from the shadow observables A/M^2 and D, for the case 1.

A/M^2	D	a/M	β/M	R_a
74	0.98	0.4926	0.0197	4.8533
72	0.97	0.5807	0.0241	4.7873
70	0.96	0.6399	0.0290	4.7203
68	0.96	0.6325	0.0369	4.6524
66	0.95	0.6763	0.0429	4.5835
64	0.95	0.6684	0.0522	4.5135

Table 2.2: Numerical values of the black hole parameters a/M and β/M estimated from the shadow observables A/M^2 and D, for the case 2.

effective geometry introduced in the previous chapter.

Having determined the photon sphere radius from Eq. (1.22), we now proceed to calculate the black hole shadow radius in nonlinear electrodynamics. Since photon trajectories follow null geodesics of the effective metric, the boundary of the shadow is governed by unstable circular photon orbits defined within this effective geometry, rather than those associated with the background spacetime metric.

Using the null condition in the effective geometry and the effective potential defined in the first chapter (1.1.1), the condition $V_{\text{eff}}(r) = 0$ yields the critical impact parameter for photon motion:

$$\xi^2(r) = \frac{r^2\,\mathcal{L}_F}{f(r)\,\Phi(r)}. \tag{2.10}$$

The shadow radius corresponds to the critical value of the impact parameter evaluated at the photon sphere radius r_{ph}. Therefore, the shadow radius for a distant observer is given by

$$R_{\text{sh}} = \xi(r_{\text{ph}}) = \sqrt{\frac{r_{\text{ph}}^2\,\mathcal{L}_F(r_{\text{ph}})}{f(r_{\text{ph}})\,\Phi(r_{\text{ph}})}}. \tag{2.11}$$

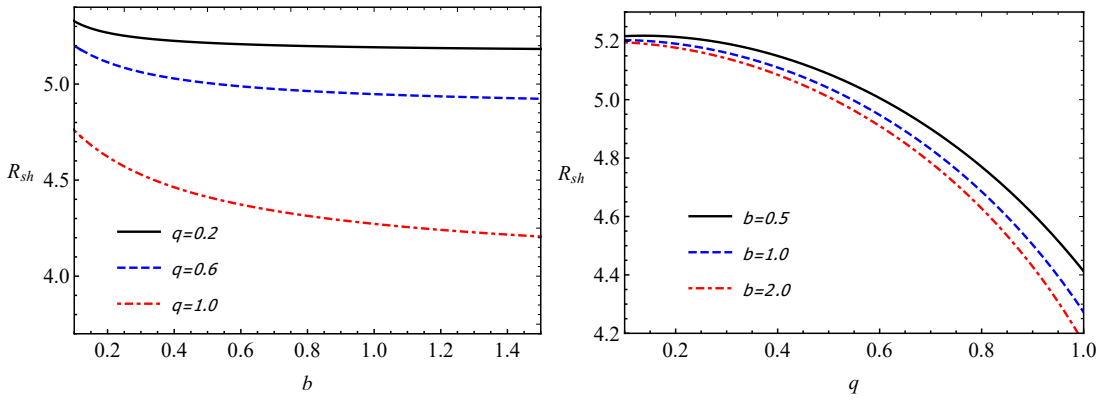


Figure 2.7: The shadow radii of black hole in NED as functions of parameters b and q, with M=1.

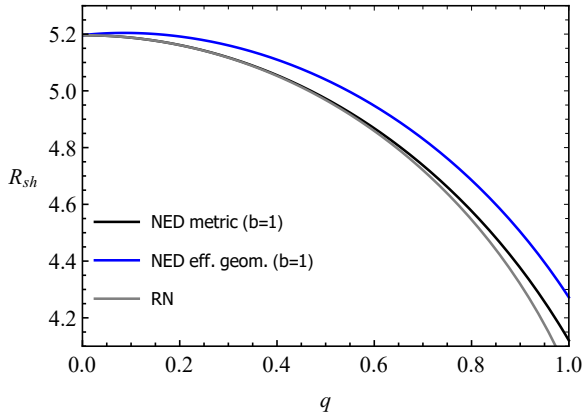


Figure 2.8: Comparison of the black hole shadow radii with (blue) and without (black) the effects of nonlinear electrodynamics on photon motion, for $M = 1$.

Equation (2.11) explicitly demonstrates that the black hole shadow in nonlinear electrodynamics is affected not only by the spacetime geometry encoded in the metric function $f(r)$, but also by the nonlinear electromagnetic corrections through the functions $\mathcal{L}_F$ and $\Phi(r)$. Consequently, deviations from the shadow predicted by linear electrodynamics arise due to the interaction between photons and the nonlinear electromagnetic field.

The dependencies of shadow radius on the black hole parameters q and b are shown in Fig. 2.7. From these plots, we observe that an increase in the electric charge q leads to a decrease in the black hole shadow radius. In contrast, the nonlinear electrodynamics parameter b has a noticeable impact on the shadow only in the small-b regime ($0.1 \lesssim b \lesssim 1.5$), where nonlinear effects become significant; for larger values of b, its influence gradually diminishes as the system approaches the linear electrodynamics limit.

To demonstrate the influence of nonlinear electrodynamics on photon propagation, we present a comparative analysis of the black hole shadow radii calculated using the original spacetime metric and the effective geometry governing photon motion (Fig. 2.8). We find that the shadow radius obtained within the effective geometry is systematically larger than that derived from the original metric. This indicates that nonlinear electrodynamic effects effectively enlarge the black hole shadow by modifying the photon trajectories through their interaction with the background electromagnetic field. Consequently, neglecting the effective geometry may lead to an underestimation of the shadow size, highlighting the importance of incorporating NED-induced corrections when modeling optical signatures of charged black holes.

2.3 Shadow of four-dimensional Einstein-Gauss-Bonnet black hole in the power Yang-Mills field

2.3.1 Black hole shadow

Photons can follow circular trajectories around the black hole, and the unstable ones among these orbits play a key role in shaping the black hole shadow. In such configurations, the radial motion remains fixed so that photons are effectively confined to a spherical photon surface. This requirement translates into a set of consistency conditions that ensure both the radial velocity and acceleration vanish. Equivalently, these conditions can be written using the radial function or, in an alternative description, through the effective potential formalism, where the potential and its radial derivative both vanish. Applying these criteria, one obtains

$$K_E = \frac{16r^2\Delta(r)}{(\Delta'(r))^2}, \qquad L_E = \frac{a^2+r^2}{a} - \frac{4r\Delta(r)}{a\Delta'(r)}, \tag{2.12}$$

Here, the quantities $L_E = l/E$ and $K_E = \big(\mathcal{K} + (l-aE)^2\big)/E^2$ are introduced to facilitate the analysis of shadow formation for static black hole configurations. In terms of the modified Carter constant, these expressions simplify to $\xi = l/E$ and $\eta = \mathcal{K}/E^2$, which are commonly referred to as Bardeen's impact parameters. For unstable circular photon orbits, these impact parameters take the form

$$\xi = \frac{r^2+a^2}{a} - \frac{4r\Delta(r)}{a\Delta'(r)}, \tag{2.13}$$

$$\eta = \frac{r^2\big(8r\Delta(r)\Delta'(r) - 16\Delta(r)\big(\Delta(r)-a^2\big) - r^2(\Delta'(r))^2\big)}{a^2(\Delta'(r))^2}. \tag{2.14}$$

For a rotating black hole, the photon region does not reduce to a single radius but instead forms a finite shell characterized by a variable photon orbit radius r_p. In this case, null geodesics approach the photon region asymptotically in a spiral motion. Consequently, the shadow boundary is described parametrically in terms of $r_p \in [r_{p,\min}, r_{p,\max}]$, where the endpoints correspond to the extremal values of the photon region. These limiting values are determined by the real positive roots of the condition $\eta = 0$. In contrast, for a non-rotating black hole, the photon region collapses to a single spherical surface, and r_p no longer acts as a free parameter. In this situation, $K_E(r_p)$ is uniquely determined for a fixed r_p, whereas $L_E(r_p)$ cannot be directly evaluated since setting $a = 0$ in Eq. (2.12) leads to an indeterminate expression. Therefore, $L_E(r_p)$ is treated as a parameter whose admissible range is determined from the condition $\Theta(\theta_0) = 0$, with endpoints defined by the corresponding solutions. Since the shadow corresponds to a two-dimensional projection, it is constructed on the celestial plane using the coordinates μ and λ, which are defined as follows:

$$\mu = -\lim_{r\to\infty}\left[\frac{d\phi}{dr}r^2\sin\theta\right]_{\theta\to\theta_0}, \tag{2.15}$$

$$\lambda = \lim_{r\to\infty}\left[\frac{d\theta}{dr}r^2\right]_{\theta\to\theta_0}, \tag{2.16}$$

Here, θ_0 denotes the inclination angle of the observer. By using the equations of motion for θ and ϕ, and evaluating the corresponding limits, the celestial coordinates can be expressed in terms of impact parameters.

The shadow profiles observed in the equatorial plane for an observer at infinity are presented in Fig. 2.9. In the upper panel, the parameters q, a, and α are kept fixed, while the different curves correspond to varying values of Q. It is found that increasing Q leads to opposite trends in the two plots: in the left panel the shadow size increases, whereas in the right panel it decreases. This contrasting behavior is attributed to the fact that the parameter q lies in different regimes, namely $(0.5, 0.75)$ and $(0.75, \infty)$, which modifies the underlying photon dynamics. This behavior is consistent with the structure of the effective potential, since the boundary of the shadow is determined by unstable circular photon orbits forming the photon sphere. In the second panel, the shadow contours are shown for different values of α while keeping Q, q, and a fixed. The influence of q is comparatively weaker, producing only minor variations, although a slight reduction in the shadow size is still visible in the right panel. Additionally, an increase in α enhances the flattening of the shadow profile on both sides. The shadow curves shown in the third panel correspond to both static and rotating

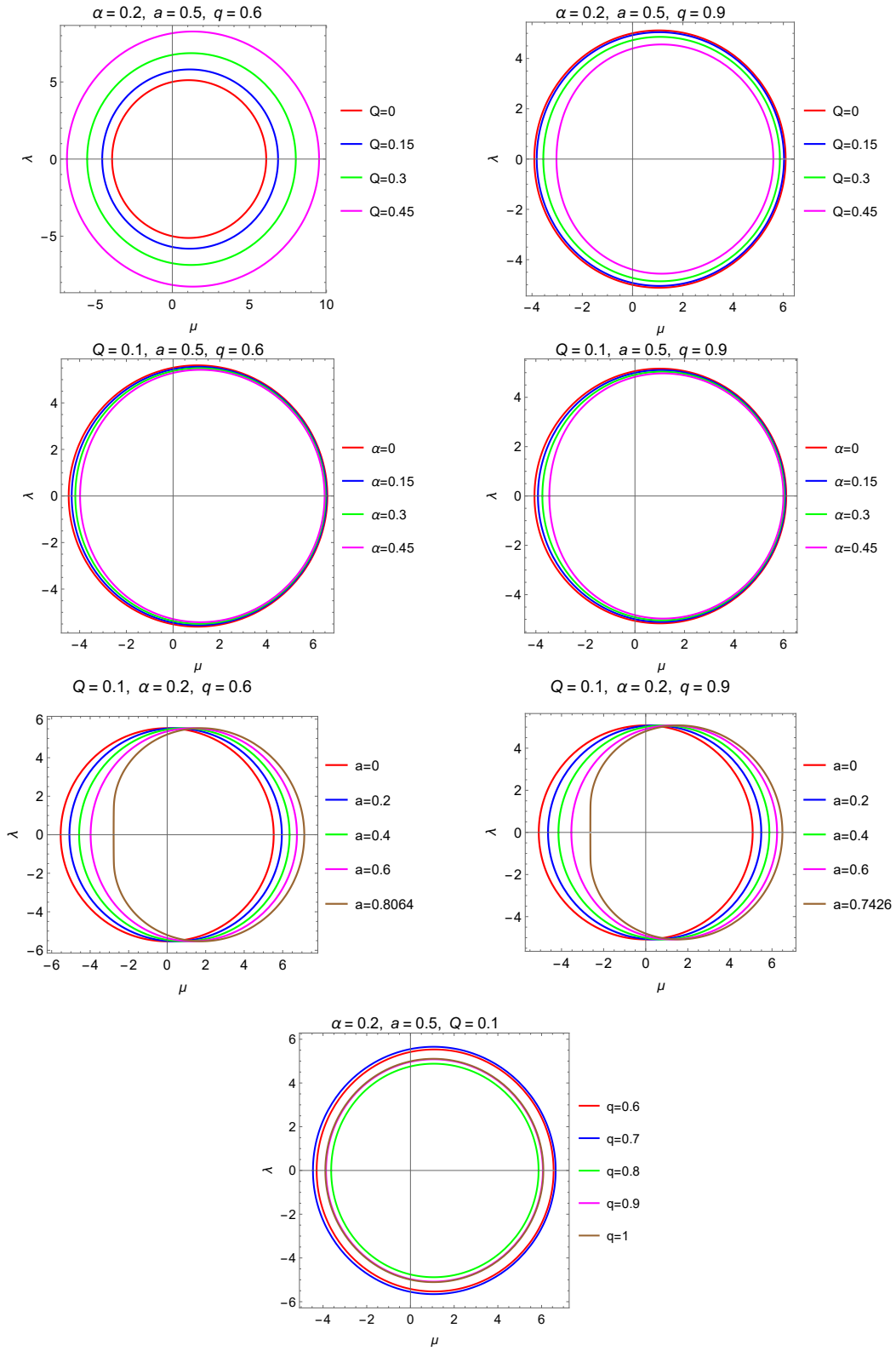


Figure 2.9: Black hole shadow profiles for different values of the parameters a, q, Q, and α.

configurations. In the static case, the shadow appears as a perfect circle in both

plots, whereas the introduction of rotation leads to a noticeable distortion, with the shadow shifted toward the right due to frame-dragging effects. For $a = 0.8064$ in the left panel and $a = 0.7426$ in the right panel, the corresponding curves represent extremal black hole configurations, exhibiting a pronounced flattening that closely resembles the characteristic deformation observed in extremal Kerr black hole shadows. It is also observed that the shadow size in the right panel is slightly smaller than that in the left panel, which can be attributed to the influence of the parameter q. The bottom panel illustrates the behavior of the shadow for fixed values of a, α, and Q, with different curves corresponding to varying q. It is evident that increasing q within the intervals $(0.5, 0.75)$ and $(0.75, \infty)$ leads to an enlargement of the shadow size. However, the two parameter regimes produce clearly separated families of curves, as reflected in the distinct branches observed in the plot.

2.3.2 Distortion

The distortion quantifies the deviation of the shadow shape from that of a non-rotating black hole by comparing differences in its size and degree of flattening. In practice, this deviation can be characterized using an observable known as the linear radius of the shadow [108], which is defined as

$$R_{sh} = \frac{(\mu_t - \mu_r)^2 + \lambda_t^2}{2|\mu_t - \mu_r|}. \tag{2.17}$$

The linear radius corresponds to the radius of a hypothetical reference circle that best fits the shadow boundary by passing through three characteristic points on the curve, namely the top point (μ_t, λ_t), the bottom point (μ_b, λ_b), and the right-most point $(\mu_r, 0)$. It is worth noting that relation (2.17) is applicable only to rotating black holes. In the static case, the symmetry of the spacetime ensures that the corresponding hypothetical circle also passes through the additional point $(-\mu_r, 0)$, resulting in a perfectly circular shadow centered at the origin. Consequently, the shadow boundary coincides exactly with this reference circle, and both share the same radius.

Using the linear shadow radius R_{sh} obtained from Eq. (2.17), one can further quantify the deformation of the shadow. The distortion parameter is then defined through the relation

$$\delta_s = \frac{|\bar{\mu}_l - \mu_l|}{R_{sh}}, \tag{2.18}$$

Here, $(\mu_l, 0)$ and $(\bar{\mu}_l, 0)$ denote the intersection points of the shadow boundary and the reference circle with the negative μ-axis, respectively. The subscript l is

used to indicate the point on the actual shadow curve lying along the $-\mu$ direction, while the overbar $\bar{\mu}_l$ corresponds to the analogous point on the hypothetical circular reference geometry.

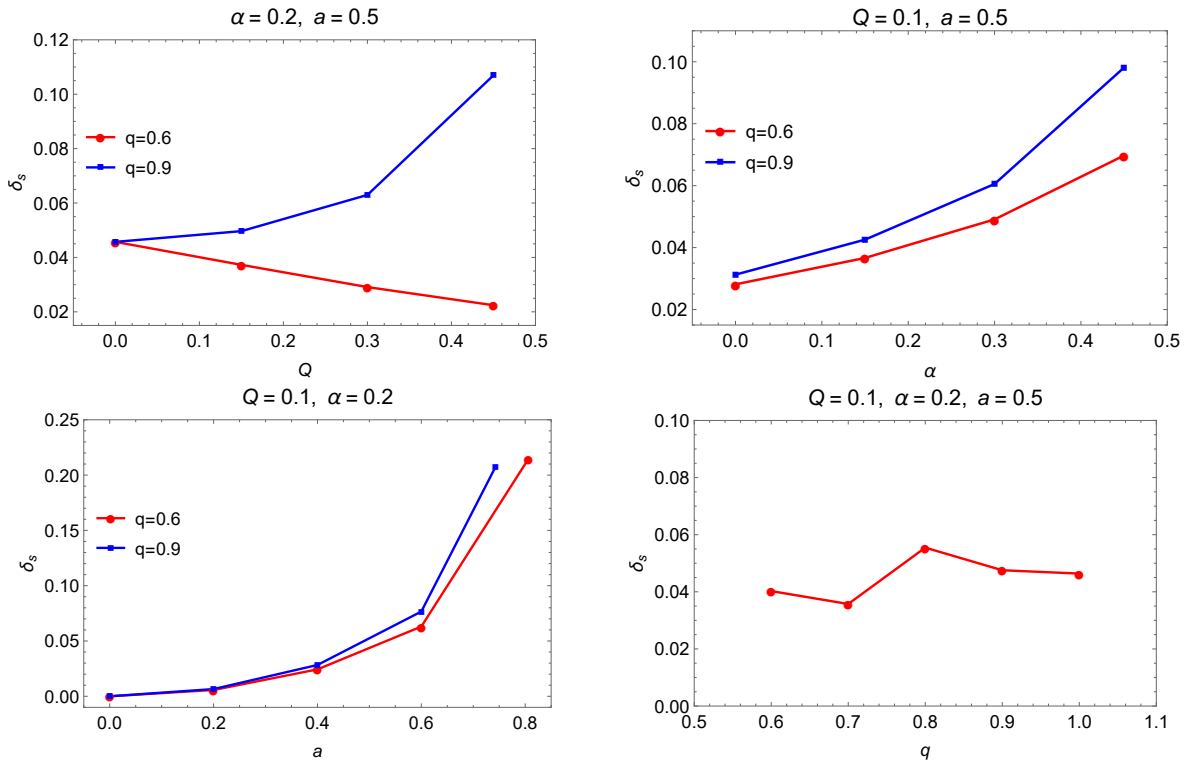


Figure 2.10: Black hole shadow distortion as a function of the parameters a, q, Q, and α.

The distortion parameter is illustrated in Fig. 2.10. In the upper panel, the left plot shows the variation of the distortion δ_s with respect to Q for different values of q, while keeping a and α fixed. In this context, the red and blue curves correspond to the left and right shadow configurations shown in the upper panel, respectively. It is observed that for $q = 0.6$, the distortion decreases approximately linearly as Q increases. In contrast, for $q = 0.9$, the distortion exhibits a rapid increase with respect to Q. The right plot in the upper panel depicts the dependence of distortion on α for fixed Q and a. For $q = 0.6$, the distortion grows nearly linearly with increasing α, whereas for $q = 0.9$, it is consistently larger and increases more sharply as α becomes larger. In the lower panel, the left plot illustrates the behavior of distortion as a function of a for fixed values of Q and α. In this case, both $q = 0.6$ and $q = 0.9$ exhibit similar qualitative behavior with respect to a, although the distortion for $q = 0.9$ remains slightly higher throughout. Since the analysis extends up to extremal values of a, a sharp increase in distortion is observed near the extremal regime due to the pronounced flattening of the shadow boundary. Finally, the right plot in the lower panel shows

the dependence of distortion on q for fixed a, α, and Q. This corresponds to the shadow configurations presented in the bottom panel. It is found that the distortion decreases with increasing q in both intervals $q < \frac{3}{4}$ and $q > \frac{3}{4}$. However, the distortion remains systematically larger in the regime $q > \frac{3}{4}$ compared to $q < \frac{3}{4}$.

2.4 Conclusions

In this chapter, the shadow structures of rotating and non-rotating black holes in various extended gravity models were analyzed. For each case, shadow observables such as the shadow radius and distortion parameter were computed. Furthermore, a modified approach was used to estimate black hole parameters from shadow profiles. The results demonstrate that shadow characteristics can serve as effective probes for detecting deviations from general relativity and for constraining parameters of alternative gravitational models. Our analysis reveals several significant findings:

- For a 4D EGB black hole surrounded by PFDM, we observe that increasing the parameters a and β results in a smaller shadow size while making the shadow more elongated. To determine the black hole parameters α and β, the shadow characteristics are quantified through the observables area A and oblateness D, which are expressed as functions of α and β for several fixed values of a. The corresponding contour plots consist of level curves of constant A and constant D, and the intersection of these curves uniquely fixes the values of α and β. This provides a systematic way to connect the black hole parameters to shadow observations.

- We analyzed the black hole shadow in the framework of nonlinear electrodynamics by employing the effective geometry that governs photon propagation. Our results show that increasing the electric charge q consistently reduces the shadow size, while the nonlinear electrodynamics parameter b significantly influences the shadow only in the small-b regime, where nonlinear effects are strongest. Moreover, a direct comparison between shadows computed in the background spacetime and in the effective geometry reveals that nonlinear electrodynamic interactions enlarge the black hole shadow.

- The analysis of black hole shadows for the EGB spacetime in the presence of a PYM field shows that the response of the shadow size depends sensitively on the parameter regimes. In particular, the shadow radius increases with Q when $q < 0.75$, whereas it decreases for $q > 0.75$ as Q is increased. On

the other hand, increasing the GB α consistently reduces the shadow size for all values of q, while simultaneously enhancing the shadow distortion. However, the influence of α remains relatively weak, indicating that it acts as a less sensitive parameter in modifying the shadow structure. Additionally, increasing q within both parameter intervals leads to a growth in the shadow size, further highlighting its role in controlling the photon dynamics.

Chapter 3

Constraints on black hole parameters using Event Horizon Telescope observations

Testing gravitational theories has become an increasingly active area of relativistic astrophysics, particularly in light of recent high-resolution observations related to black hole phenomena. black holes are among the most intriguing predictions of general relativity, originally arising as exact solutions of the Einstein field equations. Observational evidence over the past decades has strongly supported the existence of supermassive black holes at the centers of both elliptical and spiral galaxies. In addition, intermediate-mass black holes are inferred in distant, low-luminosity galaxies through high-redshift observations, further broadening the range of confirmed black hole candidates.

In 2019, the Event Horizon Telescope collaboration reported the first direct image of a black hole shadow, corresponding to the supermassive black hole located at the center of the M87 galaxy [116]. This milestone significantly strengthened interest in black hole shadow studies, as it provided an observational window into the strong-field regime of gravity. One of the earliest quantitative proposals for testing the Kerr geometry using shadow measurements was put forward by Johannsen and Psaltis [117]. Since strong gravitational lensing effects near the event horizon represent one of the few available probes of the near-horizon region [118], black hole shadows play a crucial role in testing general relativity [100]. Following the EHT observations, the M87* shadow was established as a horizon-scale astrophysical image, enabling constraints on its geometric properties. In particular, the observed shadow corresponds to a central flux-depleted region with a contrast factor of $\gtrsim 10$, and an inferred angular diameter of $\theta_d = 42 \pm 3\,\mu$as. [119–122].

Later, the EHT Collaboration also released the first image of the supermassive black hole Sgr A* at the center of the Milky Way in 2022, using stellar-dynamical

priors for its mass and distance [123–125]. The reported angular shadow diameter is $d_{sh} = 48.7 \pm 7\,\mu$as. Within general relativity, the observed properties of both M87* and Sgr A* are broadly consistent with the predictions for a Kerr black hole [116, 123]. Although alternative or modified gravity models can also produce Kerr-like geometries, current observational uncertainties in parameters such as the spin and quadrupole moment do not yet rule out such deviations entirely [126]. In particular, the consistency of Sgr A* with GR extends over a wide range of mass scales, spanning several orders of magnitude when compared with M87* [123]. As a result, one of the key challenges in modern astrophysics is to test modified and alternative theories of gravity using observational data provided by the EHT collaboration.

3.1 Constraining with Event Horizon Telescope data

In this chapter, we aim to constrain the properties of the supermassive black holes Sgr A* and M87* using the latest observational results reported by the EHT Collaboration. To this end, we first introduce the set of observables used to characterize the size and morphology of the black hole shadow. It is well established that the shadow of a spherically symmetric black hole appears as a perfect circle, whereas axially symmetric spacetimes generally produce deformed shadow structures due to rotational effects. Originally, Hioki and Maeda introduced two key observables for shadow characterization: a shadow radius, describing its overall size, and a distortion parameter, quantifying deviations from circularity [108]. In addition to this approach, alternative coordinate-independent methods have been developed, in which the shadow is described in terms of its area A and oblateness D [112, 115].

Using Eqs. (2.8) and (2.9), the shadow observables can be expressed numerically as functions of the black hole parameters. These relations provide a practical way to extract constraints on the parameter space of different gravitational theories by comparing theoretical predictions with the observational data from the EHT shadow measurements. Furthermore, the angular diameter of the shadow as measured by an observer located at a distance d from the black hole can be written as [127]

$$\theta_d = 2\frac{R_a}{d}, \qquad R_a = \sqrt{\frac{A}{\pi}}, \tag{3.1}$$

Here, R_a denotes the areal radius of the black hole shadow. From Eq. (2.8), it follows that the angular diameter of the shadow is generally a function of the black

hole parameters as well as the inclination angle of the observer. In addition, it has an implicit dependence on the black hole mass, which enters the expression through the spacetime geometry.

We use the following EHT data sets for constraints:

- Messier 87*
  $M \simeq 6.5 \times 10^9 M_\odot$, $d \simeq 16.8$Mpc, $\theta_d = 42 \pm 3\mu$as, $\theta_o \simeq 17^\circ$ [116, 121, 122]
- Sagittarius A*
  $M \simeq 4 \times 10^6 M_\odot$, $d \simeq 8$kpc, $\theta_d = 48.7 \pm 7\mu$as, $\theta_o \simeq 20^\circ - 50^\circ$ [123–125]

3.2 Four-dimensional Einstein-Gauss-Bonnet black holes in perfect fluid dark matter: constraints

In the present analysis, we derive constraints on the Gauss-Bonnet and dark matter parameters using the observational data of Sgr A* reported by the EHT collaboration. We restrict ourselves to Sgr A* in this study, since the corresponding parameter space shows better consistency with the observational bounds, whereas the results obtained from M87* do not lead to compatible constraints within the same framework. It is also worth noting that both α and β act to reduce the shadow radius; therefore, in the limit $\alpha, \beta \to 0$, the model smoothly approaches the general relativistic case, for which consistent constraints can be recovered from M87* observations.

The EHT Collaboration (2022) did not publish a single best-fit inclination such as 17° for Sgr A*. Instead, they found that low-inclination models are generally preferred, but the inclination remains model-dependent. A number of GRMHD and radiative-transfer studies before the EHT favored moderate inclinations around 50° [128, 129], which is why many shadow papers use 50°. Since this value was widely used in earlier modeling, it allows comparison across different gravity models. We can choose 20° as a representative low-inclination case chosen to investigate how the shadow observables depend on the observer's viewing angle, and it is also broadly consistent with the preference for low inclinations found in some EHT-based analyses [130, 131]. Consequently, we selected the inclination angles for Sgr A* as 20° and 50° in order to sample the low-to-moderate inclination regime compatible with the EHT observations.

We now investigate the rotating black hole model for Sgr A* within the four-dimensional EGB framework. The main goal is to compare the theoretical predictions of the shadow properties with the observational results reported by the Event Horizon Telescope. In this study, we assume that Sgr A* can be effectively

described as a 4D EGB black hole. For simplicity, we neglect the uncertainties associated with the measured mass and distance of the supermassive black hole. Nevertheless, the analysis still carries an inherent uncertainty arising from the observational error in the angular diameter of Sgr A* provided by the EHT data. Despite this limitation, the approach enables a clear assessment of how the black hole and dark matter parameters influence the shadow observables.

In Fig. 3.1, we present the constraints obtained from Sgr A* for different parameter configurations. The resulting density distributions of the predicted angular diameter of the black hole lie within the observational bounds of Sgr A*, $\theta_d = 48.7 \pm 7\,\mu$as. This agreement indicates that the theoretical predictions of the four-dimensional EGB black hole immersed in PFDM are consistent with the observations.

In contemporary black hole physics, a wide variety of black hole solutions arise from modified and alternative theories of gravity. As new gravitational models are proposed, their physical viability must be assessed against observational evidence, among which black hole shadow measurements from EHT play a crucial role. Our results indicate that shadow-based parameter estimation provides an effective framework for testing alternative gravity models. In particular, this approach can be extended to other modified gravity scenarios, offering a systematic way to confront theoretical predictions with observations. Moreover, it also provides a useful tool to investigate the influence of dark matter on black hole properties through their observable shadow signatures.

3.3 Novel charged black holes in nonlinear electrodynamics: constraints

In this section, we confront the theoretical predictions of the novel nonrotating charged black hole solution in nonlinear electrodynamics with current observational constraints obtained from black hole shadow measurements. In particular, we focus on the observable angular diameter of the shadow and employ the Event Horizon Telescope observations of the supermassive black holes M87* and Sgr A* to constrain the parameter space of the model.

Figure 3.2 shows contour plots of the angular diameter θ_d in the (b, q) plane for M87* (left panel) and Sgr A* (right panel). The spacetime is characterized by two dimensionless parameters: the charge parameter q, associated with the NED field, and the nonlinear coupling parameter b, which encodes deviations from standard Maxwell electrodynamics. The color scale represents the magnitude

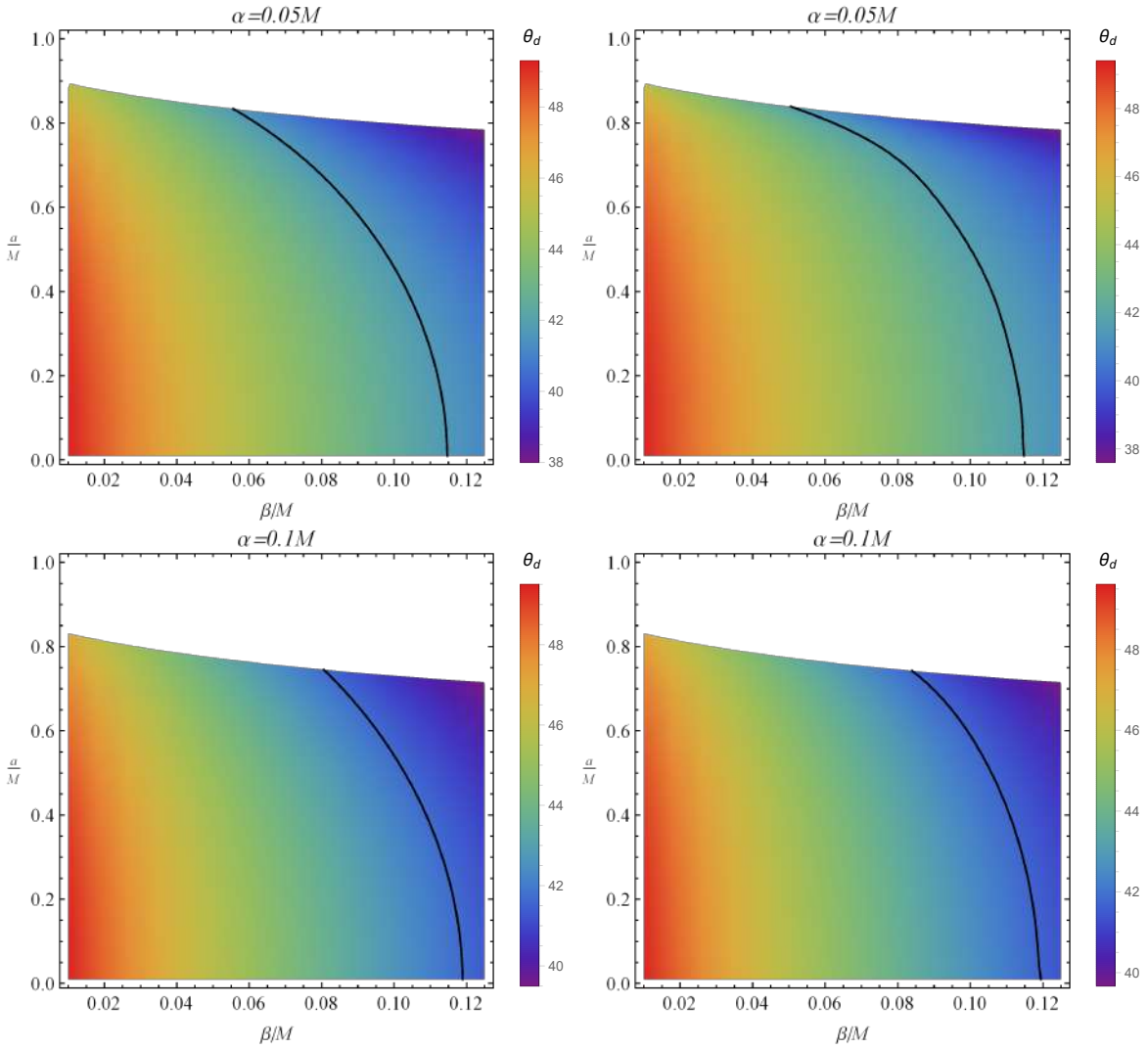


Figure 3.1: Angular diameter θ_d for rotating 4D EGB black holes in PFDM in $(a/M,\ \beta/M^2)$ parameter space at inclination angles 20° (left) and 50°(right).

of θ_d, while the solid black curves correspond to the lower observational bounds inferred from the EHT measurements. Regions of the parameter space lying below these curves are excluded, as they predict shadow sizes smaller than those allowed by observations.

From the left panel corresponding to M87*, it is evident that the angular diameter decreases monotonically with increasing charge parameter q for fixed values of b. This behavior can be understood as a consequence of the effective weakening of the gravitational attraction near the black hole due to the presence of the NED charge, which leads to a reduction in the photon sphere radius and, consequently, a smaller shadow. The nonlinear parameter b further modulates this effect, with larger values of b enhancing the deviation from the Schwarzschild limit and thus tightening the constraints on q.

A similar qualitative behavior is observed for Sgr A*, as shown in the right panel of Fig. 3.2. However, the corresponding constraints are comparatively weaker, reflecting the larger observational uncertainties associated with the shadow measurement of Sgr A*. Nevertheless, the exclusion curve still imposes an upper bound on the charge parameter across a broad range of b, ruling out configurations with sufficiently large q that would otherwise yield an unacceptably small shadow.

Overall, these results demonstrate that EHT shadow observations provide a powerful probe of nonlinear electrodynamics effects in charged black hole spacetimes. In particular, they significantly restrict the allowed values of the NED charge and coupling parameters, favoring solutions close to the Schwarzschild limit. Future high-precision shadow measurements are expected to further tighten these bounds and may allow one to discriminate between different NED models.

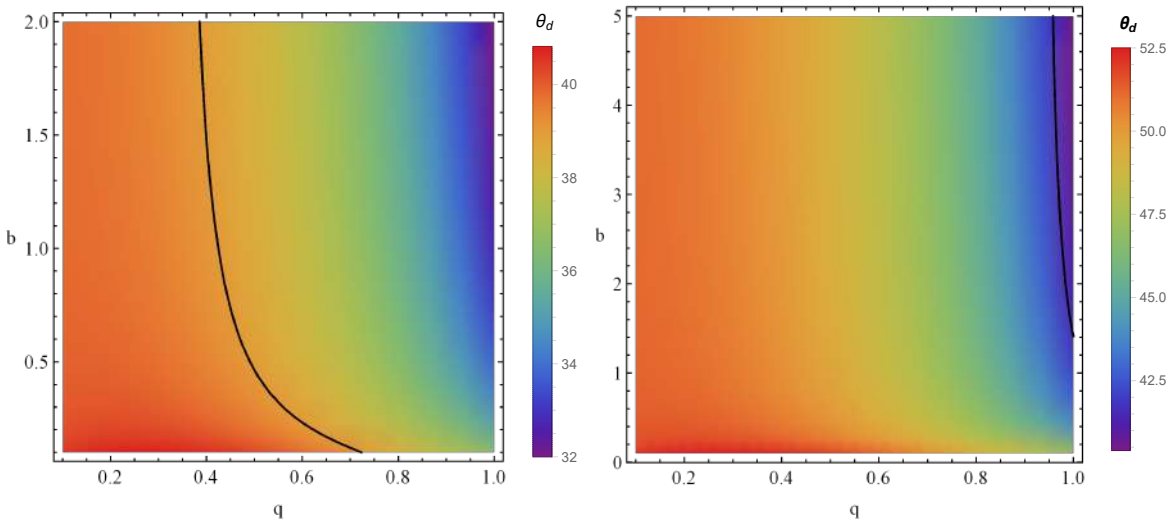


Figure 3.2: Observable angular diameter of a charged black hole in NED in the b-q parameter space for M87* (left) and Sgr A* (right). The black curves represent the lower bounds of the measured angular diameter of the supermassive black holes M87* and Sgr A*.

3.4 Four-dimensional Einstein-Gauss-Bonnet black holes in power Yang-Mills field: constraints

We now proceed to determine constraints on the parameters of the supermassive black hole M87*, assuming it can be modeled as a four-dimensional EGB black hole immersed in a PYM field. Using Eq. (2.8), the angular diameter of the shadow can be expressed as a function of the black hole parameters and the inclination angle of the observer. In addition, it carries an implicit dependence

on the black hole mass through the underlying spacetime geometry. The angular diameter can then be computed from Eq. (3.1) for the 4D EGB black hole in the PYM framework. By comparing the resulting theoretical predictions with the observed angular diameter of the M87* shadow, one can place constraints on the corresponding black hole parameters.

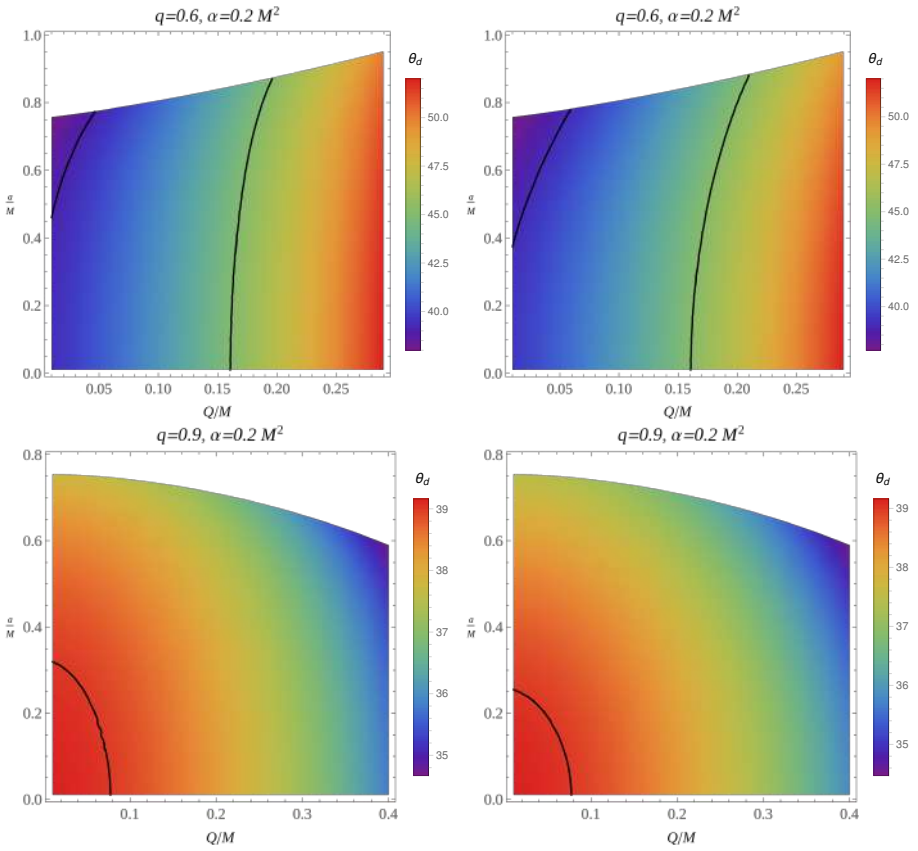


Figure 3.3: Angular diameter observable θ_d of the black hole shadow as a function of the parameters a/M and Q/M for inclination angles of 90° (left panels) and 17° (right panels). The black curves indicate the boundaries corresponding to the observed angular diameter $\theta_d = 42 \pm 3\,\mu$as of the supermassive black hole M87* reported by the EHT.

Figure 3.3 presents the density distributions of the angular diameter θ_d in the a–Q parameter space for inclination angles of 90° (left panel) and 17° (right panel), while keeping q and α fixed. The black curves indicate the observational bounds of the angular diameter of the M87* shadow obtained from EHT measurements. These contours therefore delineate the regions of parameter space that are consistent with the observed shadow size of the supermassive black hole M87*. A notable feature of these results is the clear separation between the cases $q = 0.6$ and $q = 0.9$, which arises from the opposite dependence of the shadow size on the parameter q. In particular, for $q = 0.6$ and $\alpha = 0.2M^2$, both upper and lower bounds can be placed on the spin and charge parameters. In contrast, for $q = 0.9$

and the same value of α, only lower bounds on the black hole spin and charge parameters can be obtained.

Moreover, it is also observed from the figure that the black curves representing the observational bounds shift slightly towards the right, accompanied by a reduction in the allowed range of the spin parameter when the inclination angle is changed from 90° to 17°. In Fig. 3.4, we present additional constraints derived

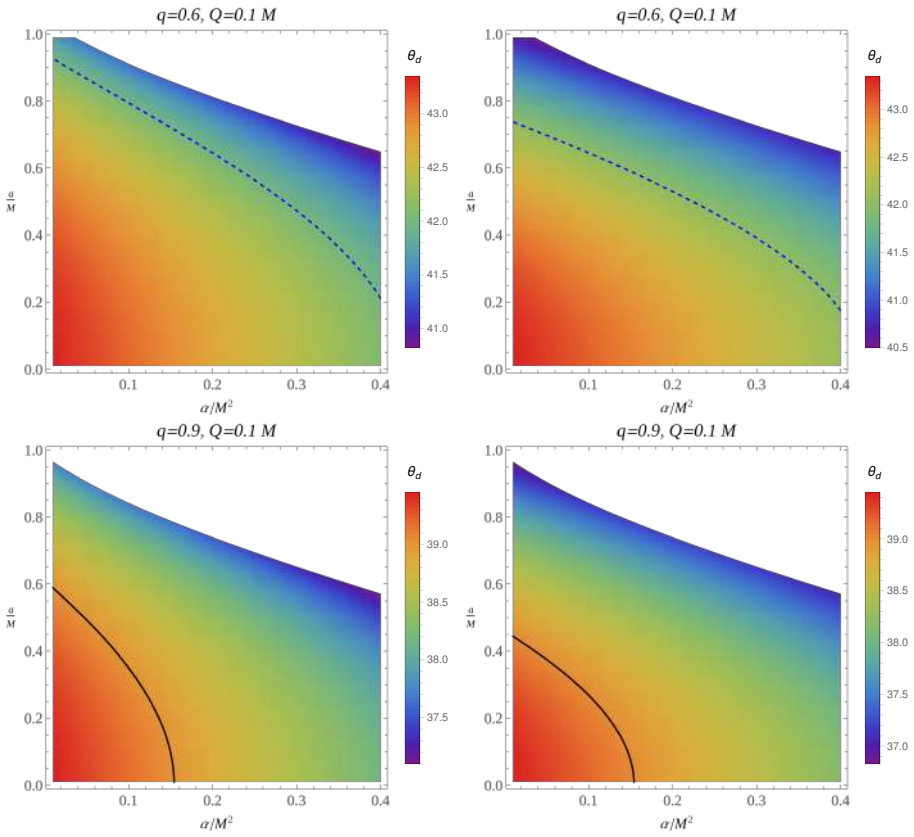


Figure 3.4: Same as Fig. 3.3, but showing the constraints on the black hole spin and Gauss-Bonnet parameter for fixed values of $q = 0.6$ (top panel) and $q = 0.9$ (bottom panel) at $Q = 0.1M$.

from the EHT observations of the M87* shadow. Here, the angular diameter of the black hole shadow is expressed as a function of the spin and GB coupling parameter. In the upper panel corresponding to $q = 0.6$, which is consistent with the M87* configuration, we illustrate the relation between the spin parameter and the GB coupling for the mean observed angular diameter of $42\,\mu$as. The blue dashed curves represent the distribution of the observable in the parameter space in a clear and systematic manner. In contrast, for $q = 0.9$ (lower panel), only lower bounds on both the spin and GB coupling parameters can be obtained. Overall, the results show only minor variations with respect to the inclination angle. It is also evident that increasing q leads to a reduction in the allowed range of the

spin parameter under observational constraints.

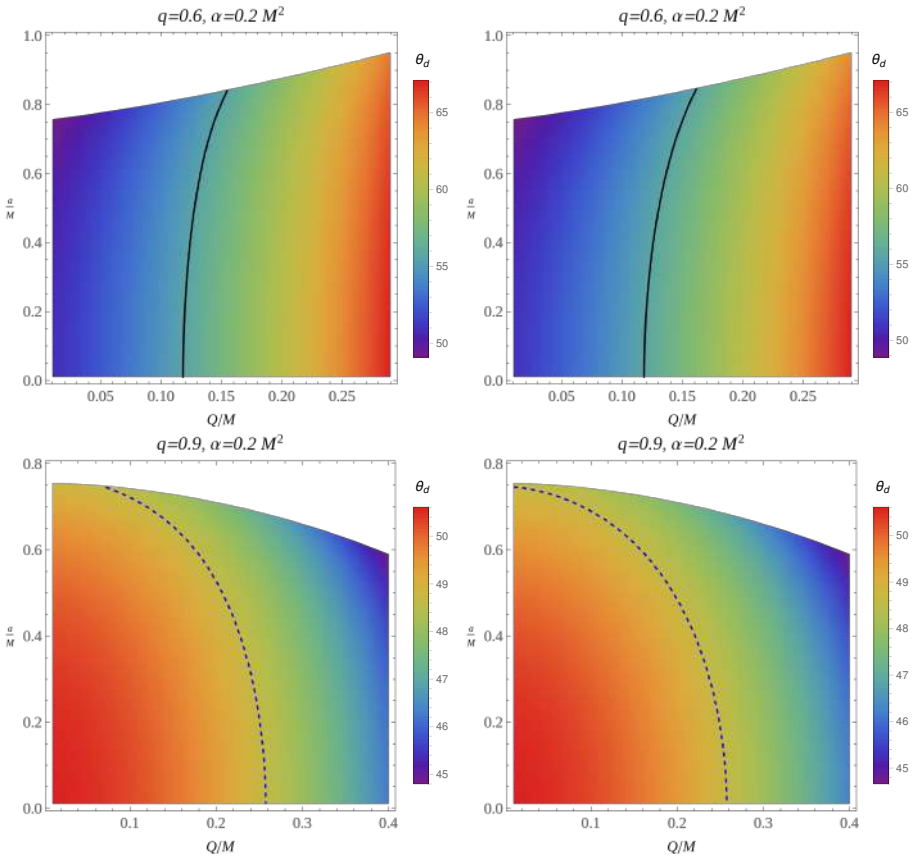


Figure 3.5: Angular diameter θ_d of the black hole shadow as a function of the parameters a/M and Q/M for inclination angles of 90° (left panels) and 50° (right panels). The black curves correspond to the observational bounds of $\theta_d = 48.7 \pm 7\,\mu$as, while the blue dashed curves represent the mean value $\theta_d = 48.7\,\mu$as of the Sgr A* shadow reported by the EHT.

Similarly, Figs. 3.5 and 3.6 present the constraints on the spin and charge parameters for Sgr A*. In these figures, the angular diameter of the shadow is plotted against the black hole parameters for two different inclination angles, 90° (left panels) and 50° (right panels). Because each parameter influences the shadow observables in a different way, the resulting constraint regions vary accordingly for different parameter sets. In the upper panel of Fig. 3.5, for $q = 0.6$ and $\alpha = 0.2M^2$, upper bounds on both the spin and charge parameters are obtained. However, when $q = 0.9$, these bounds shift and no simultaneous upper and lower constraints can be imposed, with the parameter space remains consistent with the observational range due to the relatively large uncertainty in the data. In the upper panel of Fig. 3.6, lower bounds on the spin and Gauss-Bonnet parameters are obtained for Sgr A* at $q = 0.6$ and $Q = 0.1M$. In contrast, for $q = 0.9$, no meaningful constraints are obtained, consistent with the behavior observed in Fig. 3.5. Overall, these results indicate that shadow-based observables can

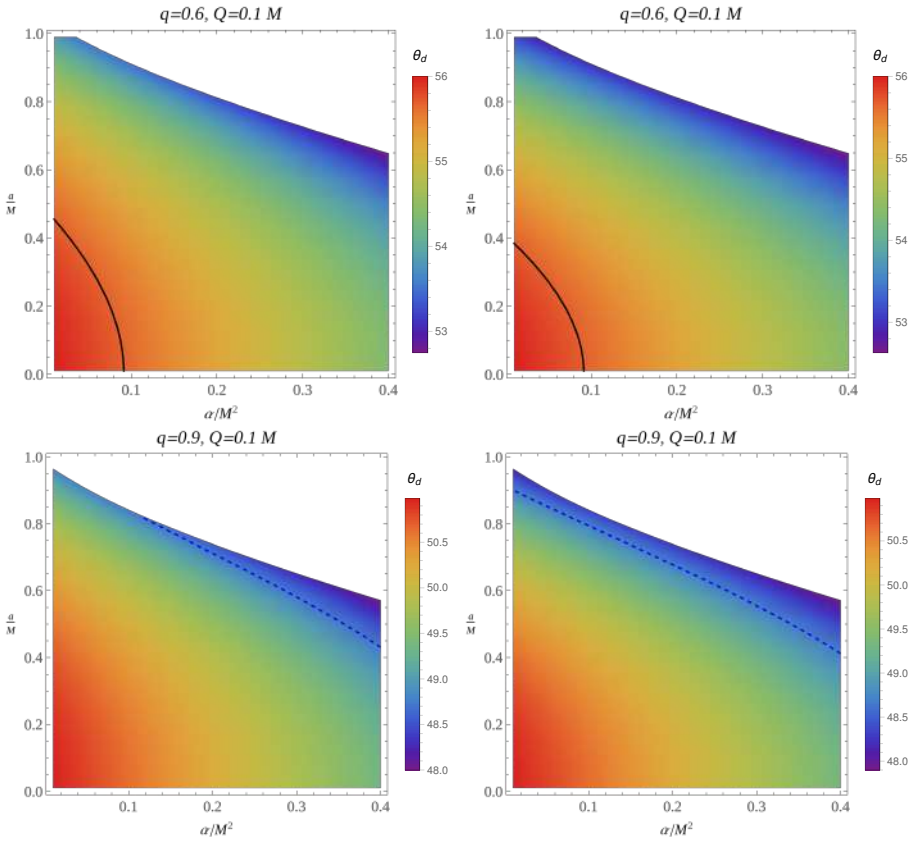


Figure 3.6: Angular diameter θ_d of the black hole shadow as a function of the parameters a/M and α/M^2 for inclination angles of 90° (left panels) and 50° (right panels). The black curves correspond to the observational bounds $\theta_d = 48.7 \pm 7\,\mu$as of the Sgr A* shadow reported by the EHT, while the blue dashed curves represent the average value $\theta_d = 48.7\,\mu$as.

provide useful estimates of black hole parameters using astrophysical observations, helping to delimit their physically allowed ranges. In this context, the shadow of the considered black hole can be directly compared with the observed images of M87* and Sgr A*.

3.5 Conclusions

In this chapter, black hole shadow-based constraints were obtained using observational data from the EHT for the supermassive black holes M87* and Sgr A*. The analysis was performed within the framework of alternative gravity models, including charged black holes in nonlinear electrodynamics and 4D Einstein-Gauss-Bonnet black holes in perfect fluid dark matter and power-Yang-Mills fields. By comparing the theoretical shadow radii with the EHT data, parameter bounds were derived for each model. The results presented in this chapter are summarized below:

- By identifying the rotating four-dimensional Einstein–Gauss–Bonnet black hole immersed in PFDM with the supermassive black hole Sgr A*, we use the observed values of its mass, distance, and shadow angular diameter to place bounds on the spin parameter a and the PFDM parameter β. The analysis shows that a finite region of the parameter space remains consistent with the shadow measurements of Sgr A*, indicating that present Event Horizon Telescope observations are still compatible with the existence of dark matter effects in galactic cores.

- We have shown that the shadow observations of supermassive black holes provide stringent constraints on novel nonrotating charged black holes in nonlinear electrodynamics. The analysis reveals that increasing the NED charge leads to a systematic reduction of the photon sphere radius and, consequently, the shadow size, allowing EHT data to place upper bounds on the charge parameter for a wide range of the nonlinear coupling b. While the constraints derived from M87* are stronger due to its higher observational precision, those from Sgr A* are qualitatively consistent.

- We have derived constraint values for the parameters of the four-dimensional EGB black hole in a PYM field using EHT observations of the supermassive black holes Sgr A* and M87*, for $q = 0.6$ and $q = 0.9$. It is observed that, for M87* at $q = 0.6$, both upper and lower bounds can be placed on the charge and spin parameters. In contrast, for Sgr A*, only upper bounds are obtained for the spin and charge parameters, primarily due to the relatively larger uncertainty in its shadow measurements. For $q = 0.9$, the parameter space becomes more constrained: in the a-α plane, only upper limits are obtained for M87*, while for Sgr A* no meaningful constraints can be established within the considered observational accuracy.

Conclusion

The following conclusions are drawn based on the research conducted in this dissertation.

1. For the first time, it has been obtained and analyzed rotating black hole metrics in extended 4D Einstein-Gauss-Bonnet gravity (EGB), demonstrating deviations from classical Kerr metrics.

2. For the first time, the photon orbits, shadow boundaries, and distortion parameters have been investigated for black holes in nonlinear electrodynamics (NED) and extended 4D EGB gravity scenarios. It has been shown that black hole shadows in alternative theories exhibit measurable differences in size, distortion, and photon ring structure compared to general relativity (GR).

3. Parameter estimation plots have been obtained for the 4D EGB black holes through shadow observables (area and oblateness), providing an effective method for connecting black hole properties with observable quantities.

4. It has been found that the presence of NED increases the shadow radius of charged black holes compared to the standard Einstein–Maxwell case, providing an observable signature of NED corrections.

5. It has been established that perfect fluid dark matter (PFDM) surrounding black holes significantly reduces shadow radii, providing an observational signature to constrain dark matter density profiles.

6. For the first time, the constraints on black hole parameters in NED, in extended 4D EGB gravity, have been found using M87* and Sgr A* shadow observations from EHT.

7. Specific observational signatures (shadow asymmetry) have been identified to distinguish between GR and alternative theories with next-generation telescopes (ngEHT).

Bibliography

[1] M. A. Raza, J. Rayimbaev, F. Sarikulov, M. Zubair, B. Ahmedov, and Z. Stuchlik, "Shadow of novel rotating black hole in GR coupled to nonlinear electrodynamics and constraints from EHT results," *Phys. Dark Univ.*, vol. 44, p. 101488, 2024.

[2] M. Zahid, F. Sarikulov, C. Shen, M. Umaraliyev, and J. Rayimbaev, "Shadow and quasinormal modes of novel charged rotating black hole in Born–Infeld theory: Constraints from EHT results," *Phys. Dark Univ.*, vol. 46, p. 101616, 2024.

[3] F. Atamurotov, F. Sarikulov, S. G. Ghosh, and G. Mustafa, "Exploring perfect fluid dark matter with EHT results of Sgr A* through rotating 4D-EGB black holes," *Phys. Dark Univ.*, vol. 46, p. 101625, 2024.

[4] O. Yunusov, J. Rayimbaev, F. Sarikulov, M. Zahid, A. Abdujabbarov, and Z. Stuchlík, "Rotating charged black holes in EMS theory: shadow studies and constraints from EHT observations," *Eur. Phys. J. C*, vol. 84, no. 12, p. 1240, 2024.

[5] M. Zahid, F. Sarikulov, C. Shen, J. Rayimbaev, K. Badalov, and S. Muminov, "Shadow and quasinormal modes of rotating charged black holes in Kalb–Ramond gravity and implications from EHT data," *Chin. J. Phys.*, vol. 91, pp. 45–65, 2024.

[6] M. Zahid, F. Sarikulov, C. Shen, S. Ahmedov, and J. Rayimbaev, "Shadow of rotating black holes surrounded by dark fluid with Chaplygin-like equation of state and constraints from EHT results," *Class. Quant. Grav.*, vol. 41, no. 20, p. 205004, 2024.

[7] S. U. Khan, J. Rayimbaev, F. Sarikulov, and O. Abdurakhmonov, "Optical features of rotating quintessential charged black holes in de-Sitter spacetime," *Chin. J. Phys.*, vol. 90, pp. 690–706, 2024.

[8] M. Zubair, M. A. Raza, F. Sarikulov, and J. Rayimbaev, "4d einstein-gauss-bonnet black hole in power-yang-mills field: a shadow study," *Journal of Cosmology and Astroparticle Physics*, vol. 2023, p. 058, oct 2023.

[9] M. Zahid, J. Rayimbaev, F. Sarikulov, S. U. Khan, and J. Ren, "Shadow of rotating and twisting charged black holes with cloud of strings and quintessence," *Eur. Phys. J. C*, vol. 83, no. 9, p. 855, 2023.

[10] F. Sarikulov, F. Atamurotov, A. Abdujabbarov, and V. Khamidov, "Photon motion and weak gravitational lensing in black-bounce spacetime," *Chin. Phys. C*, vol. 47, no. 11, p. 115101, 2023.

[11] J. Rayimbaev, K. F. Dialektopoulos, F. Sarikulov, and A. Abdujabbarov, "Quasiperiodic oscillations around hairy black holes in Horndeski gravity," *Eur. Phys. J. C*, vol. 83, no. 7, p. 572, 2023.

[12] F. Sarikulov, F. Atamurotov, A. Abdujabbarov, and B. Ahmedov, "Shadow of the Kerr-like black hole," *Eur. Phys. J. C*, vol. 82, no. 9, p. 771, 2022.

[13] F. Atamurotov, F. Sarikulov, V. Khamidov, and A. Abdujabbarov, "Gravitational weak lensing of Schwarzschild-like black hole in presence of plasma," *Eur. Phys. J. Plus*, vol. 137, no. 5, p. 567, 2022.

[14] F. Atamurotov, F. Sarikulov, A. Abdujabbarov, and B. Ahmedov, "Gravitational weak lensing by black hole in Horndeski gravity in presence of plasma," *Eur. Phys. J. Plus*, vol. 137, no. 3, p. 336, 2022.

[15] H. Reissner, "Über die Eigengravitation des elektrischen Feldes nach der Einsteinschen Theorie," *Annalen der Physik*, vol. 355, pp. 106–120, Jan 1916.

[16] G. Nordström, "On the energy of the gravitational field in Einstein's theory," *Proc. Kon. Ned. Akad. Wet.*, vol. 20, pp. 1238–1245, 1918.

[17] J. Bardeen in *Proceedings of GR5* (C. DeWitt and B. DeWitt, eds.), p. 174, Tbilisi, USSR, Gordon and Breach, 1968.

[18] E. Ayón-Beato and A. García, "Regular Black Hole in General Relativity Coupled to Nonlinear Electrodynamics," *Physical Review Letters*, vol. 80, pp. 5056–5059, June 1998.

[19] K. A. Bronnikov, "Regular magnetic black holes and monopoles from nonlinear electrodynamics," *Phys. Rev. D*, vol. 63, p. 044005, Feb. 2001.

[20] C. Bambi and L. Modesto, "Rotating regular black holes," *Physics Letters B*, vol. 721, pp. 329–334, Apr. 2013.

[21] B. Toshmatov, Z. Stuchlík, J. Schee, and B. Ahmedov, "Electromagnetic perturbations of black holes in general relativity coupled to nonlinear electrodynamics," *Physical Review D*, vol. 97, p. 084058, Apr 2018.

[22] I. Dymnikova and E. Galaktionov, "Dynamics of Electromagnetic Fields and Structure of Regular Rotating Electrically Charged Black Holes and Solitons in Nonlinear Electrodynamics Minimally Coupled to Gravity," *Universe*, vol. 5, p. 205, Sept. 2019.

[23] L. Balart, S. Belmar-Herrera, G. Panotopoulos, and Á. Rincón, "Novel charged black hole solutions of Born-Infeld type: General properties, Smarr formula and Quasinormal frequencies," *Annals of Physics*, vol. 454, p. 169329, July 2023.

[24] B. Toshmatov, Z. Stuchlík, B. Ahmedov, and D. Malafarina, "Relaxations of perturbations of spacetimes in general relativity coupled to nonlinear electrodynamics," *prd*, vol. 99, p. 064043, Mar 2019.

[25] M. Born and L. Infeld, "Foundations of the new field theory," *Proc. Roy. Soc. Lond. A*, vol. 144, no. 852, pp. 425–451, 1934.

[26] S. Kruglov, "A model of nonlinear electrodynamics," *Annals of Physics*, vol. 353, pp. 299–306, 2015.

[27] I. Bandos, K. Lechner, D. Sorokin, and P. K. Townsend, "Nonlinear duality-invariant conformal extension of maxwell's equations," *Phys. Rev. D*, vol. 102, p. 121703, Dec 2020.

[28] S. Kruglov, "On generalized modmax model of nonlinear electrodynamics," *Physics Letters B*, vol. 822, p. 136633, 2021.

[29] I. Dymnikova, "Regular electrically charged vacuum structures with de Sitter centre in nonlinear electrodynamics coupled to general relativity," *Classical and Quantum Gravity*, vol. 21, pp. 4417–4428, Sep 2004.

[30] J. Schee and Z. Stuchlík, "Effective Geometry of the Bardeen Spacetimes: Gravitational Lensing and Frequency Mapping of Keplerian Disks," *The Astrophysical Journal*, vol. 874, p. 12, Mar 2019.

[31] Z. Stuchlík and J. Schee, "Shadow of the regular bardeen black holes and comparison of the motion of photons and neutrinos," *The European Physical Journal C*, vol. 79, p. 44, Jan 2019.

[32] C. Lanczos, "A Remarkable property of the Riemann-Christoffel tensor in four dimensions," *Annals Math.*, vol. 39, pp. 842–850, 1938.

[33] D. Lovelock, "The Einstein Tensor and Its Generalizations," *Journal of Mathematical Physics*, vol. 12, pp. 498–501, Mar. 1971.

[34] D. G. Boulware and S. Deser, "String-generated gravity models," *Phys. Rev. lett.*, vol. 55, pp. 2656–2660, Dec. 1985.

[35] D. L. Wiltshire, "Spherically symmetric solutions of Einstein-Maxwell theory with a Gauss-Bonnet term," *Phys. Lett. B*, vol. 169, pp. 36–40, Mar. 1986.

[36] B. Zwiebach, "Curvature squared terms and string theories," *Phys. Lett. B*, vol. 156, pp. 315–317, June 1985.

[37] S. Nojiri, S. D. Odintsov, and V. K. Oikonomou, "Ghost-free Gauss-Bonnet theories of gravity," *Phys. Rev. D*, vol. 99, p. 044050, Feb. 2019.

[38] S. Mignemi and N. R. Stewart, "Charged black holes in effective string theory," *Phys. Rev. D*, vol. 47, pp. 5259–5269, June 1993.

[39] S. Jhingan and S. G. Ghosh, "Inhomogeneous dust collapse in 5D Einstein-Gauss-Bonnet gravity," *Phys. Rev. D*, vol. 81, p. 024010, Jan. 2010.

[40] S. Nojiri and S. D. Odintsov, "Anti-de-Sitter black hole thermodynamics in higher derivative gravity and new confining-deconfining phases in dual CFT," *Phys. Lett. B*, vol. 521, pp. 87–95, Nov. 2001.

[41] S. G. Ghosh, D. V. Singh, and S. D. Maharaj, "Regular black holes in Einstein-Gauss-Bonnet gravity," *Phys. Rev. D*, vol. 97, p. 104050, May 2018.

[42] Y. Tomozawa, "Quantum corrections to gravity," *arXiv e-prints*, p. arXiv:1107.1424, July 2011.

[43] G. Cognola, R. Myrzakulov, L. Sebastiani, and S. Zerbini, "Einstein gravity with Gauss-Bonnet entropic corrections," *Phys. Rev. D*, vol. 88, p. 024006, July 2013.

[44] D. Glavan and C. Lin, "Einstein-Gauss-Bonnet Gravity in Four-Dimensional Spacetime," *Phys. Rev. Lett.*, vol. 124, no. 8, p. 081301, 2020.

[45] H. Lü and Y. Pang, "Horndeski gravity as D $\to$ 4 limit of Gauss-Bonnet," *Phys. Lett. B*, vol. 809, p. 135717, Oct. 2020.

[46] A. Casalino, A. Colléaux, M. Rinaldi, and S. Vicentini, "Regularized Lovelock gravity," *Physics of the Dark Universe*, vol. 31, p. 100770, Jan. 2021.

[47] R. A. Hennigar, D. KubizÅák, R. B. Mann, and C. Pollack, "On taking the D $\to$ 4 limit of Gauss-Bonnet gravity: theory and solutions," *Journal of High Energy Physics*, vol. 2020, p. 27, July 2020.

[48] D. Lovelock, "The Four-Dimensionality of Space and the Einstein Tensor," *Journal of Mathematical Physics*, vol. 13, pp. 874–876, June 1972.

[49] R. A. Konoplya and A. F. Zinhailo, "Quasinormal modes, stability and shadows of a black hole in the 4D Einstein-Gauss-Bonnet gravity," *Eur. Phys. J. C*, vol. 80, p. 1049, Nov. 2020.

[50] P. G. S. Fernandes, "Charged black holes in AdS spaces in 4D Einstein Gauss-Bonnet gravity," *Phys. Lett. B*, vol. 805, p. 135468, June 2020.

[51] D. D. Doneva and S. S. Yazadjiev, "Relativistic stars in 4D Einstein-Gauss-Bonnet gravity," *JCAP*, vol. 2021, p. 024, May 2021.

[52] U. Papnoi and F. Atamurotov, "Rotating charged black hole in 4 D Einstein-Gauss-Bonnet gravity: Photon motion and its shadow," *Physics of the Dark Universe*, vol. 35, p. 100916, Mar. 2022.

[53] F. Atamurotov, S. Shaymatov, P. Sheoran, and S. Siwach, "Charged black hole in 4D Einstein-Gauss-Bonnet gravity: particle motion, plasma effect on weak gravitational lensing and centre-of-mass energy," *JCAP*, vol. 2021, p. 045, Aug. 2021.

[54] R.-G. Cai, L.-M. Cao, and N. Ohta, "Black holes in gravity with conformal anomaly and logarithmic term in black hole entropy," *Journal of High Energy Physics*, vol. 2010, p. 82, Apr. 2010.

[55] R. Kumar and S. G. Ghosh, "Rotating black holes in 4D Einstein-Gauss-Bonnet gravity and its shadow," *JCAP*, vol. 2020, p. 053, July 2020.

[56] S.-b. Chen and J.-l. Jing, "Quasinormal modes of a black hole surrounded by quintessence," *Class. Quant. Grav.*, vol. 22, pp. 4651–4657, 2005.

[57] T. Lacroix and J. Silk, "Constraining the distribution of dark matter at the Galactic Centre using the high-resolution Event Horizon Telescope," *Astron. Astrophys.*, vol. 554, p. A36, 2013.

[58] S. G. Ghosh, "Rotating black hole and quintessence," *Eur. Phys. J. C*, vol. 76, no. 4, p. 222, 2016.

[59] A. Das, A. Saha, and S. Gangopadhyay, "Investigation of circular geodesics in a rotating charged black hole in the presence of perfect fluid dark matter," *Class. Quant. Grav.*, vol. 38, no. 6, p. 065015, 2021.

[60] F. Atamurotov, A. Abdujabbarov, and W.-B. Han, "Effect of plasma on gravitational lensing by a Schwarzschild black hole immersed in perfect fluid dark matter," *Phys. Rev. D*, vol. 104, no. 8, p. 084015, 2021.

[61] F. Atamurotov, U. Papnoi, and K. Jusufi, "Shadow and deflection angle of charged rotating black hole surrounded by perfect fluid dark matter," *Class. Quant. Grav.*, vol. 39, no. 2, p. 025014, 2022.

[62] F. De Paolis, G. Ingrosso, A. A. Nucita, A. Qadir, and A. F. Zakharov, "Estimating the parameters of the Sgr A* black hole," *Gen. Rel. Grav.*, vol. 43, pp. 977–988, 2011.

[63] K. Jusufi and Saurabh, "Black hole shadows in Verlinde's emergent gravity," *Mon. Not. Roy. Astron. Soc.*, vol. 503, no. 1, pp. 1310–1318, 2021.

[64] S. Vagnozzi *et al.*, "Horizon-scale tests of gravity theories and fundamental physics from the Event Horizon Telescope image of Sagittarius A," *Class. Quant. Grav.*, vol. 40, no. 16, p. 165007, 2023.

[65] R. C. Pantig and A. Övgün, "Dehnen halo effect on a black hole in an ultra-faint dwarf galaxy," *JCAP*, vol. 08, no. 08, p. 056, 2022.

[66] M. Tanabashi *et al.*, "Review of Particle Physics," *Phys. Rev. D*, vol. 98, no. 3, p. 030001, 2018.

[67] X. Hou, Z. Xu, and J. Wang, "Rotating Black Hole Shadow in Perfect Fluid Dark Matter," *JCAP*, vol. 12, p. 040, 2018.

[68] S. Haroon, M. Jamil, K. Jusufi, K. Lin, and R. B. Mann, "Shadow and Deflection Angle of Rotating Black Holes in Perfect Fluid Dark Matter with a Cosmological Constant," *Phys. Rev. D*, vol. 99, no. 4, p. 044015, 2019.

[69] A. Das, A. Saha, and S. Gangopadhyay, "Study of circular geodesics and shadow of rotating charged black hole surrounded by perfect fluid dark matter immersed in plasma," *Class. Quant. Grav.*, vol. 39, no. 7, p. 075005, 2022.

[70] B. Narzilloev, J. Rayimbaev, S. Shaymatov, A. Abdujabbarov, B. Ahmedov, and C. Bambi, "Dynamics of test particles around a Bardeen black hole surrounded by perfect fluid dark matter," *Phys. Rev. D*, vol. 102, no. 10, p. 104062, 2020.

[71] Z. Xu, J. Wang, and X. Hou, "Kerr–anti-de Sitter/de Sitter black hole in perfect fluid dark matter background," *Class. Quant. Grav.*, vol. 35, no. 11, p. 115003, 2018.

[72] E. T. Newman and A. I. Janis, "Note on the Kerr Spinning-Particle Metric," *Journal of Mathematical Physics*, vol. 6, pp. 915–917, June 1965.

[73] E. T. Newman, E. Couch, K. Chinnapared, A. Exton, A. Prakash, and R. Torrence, "Metric of a Rotating, Charged Mass," *Journal of Mathematical Physics*, vol. 6, pp. 918–919, June 1965.

[74] D. Hansen and N. Yunes, "Applicability of the newman-janis algorithm to black hole solutions of modified gravity theories," *Phys. Rev. D*, vol. 88, p. 104020, Nov 2013.

[75] M. Azreg-Aïnou, "Generating rotating regular black hole solutions without complexification," *Phys. Rev. D*, vol. 90, p. 064041, Sep 2014.

[76] M. Azreg-Aïnou, "From static to rotating to conformal static solutions: rotating imperfect fluid wormholes with(out) electric or magnetic field," *European Physical Journal C*, vol. 74, p. 2865, May 2014.

[77] M. Fathi, M. Olivares, and J. R. Villanueva, "Ergosphere, photon region structure, and the shadow of a rotating charged weyl black hole," *Galaxies*, vol. 9, no. 2, 2021.

[78] R. K. Walia, S. D. Maharaj, and S. G. Ghosh, "Rotating black holes in Horndeski gravity: thermodynamic and gravitational lensing," *European Physical Journal C*, vol. 82, p. 547, June 2022.

[79] R. P. Kerr, "Gravitational field of a spinning mass as an example of algebraically special metrics," *Phys. Rev. Lett.*, vol. 11, pp. 237–238, 1963.

[80] Y.-L. Wang and X.-H. Ge, "Black holes in 4D Einstein-Maxwell-Gauss-Bonnet gravity coupled with scalar fields," *European Physical Journal C*, vol. 81, p. 361, Apr. 2021.

[81] H. Shah, Z. Ahmad, and H. H. Shah, "Quintessence background for 4D Einstein-Gauss-Bonnet black holes," *Physics Letters B*, vol. 818, p. 136383, July 2021.

[82] A. Ali and K. Saifullah, "Charged black holes in 4D Einstein-Gauss-Bonnet gravity coupled to nonlinear electrodynamics with maximum allowable symmetries," *Annals of Physics*, vol. 437, p. 168726, Feb. 2022.

[83] D. V. Singh, S. G. Ghosh, and S. D. Maharaj, "Clouds of strings in 4 D Einstein-Gauss-Bonnet black holes," *Physics of the Dark Universe*, vol. 30, p. 100730, Dec. 2020.

[84] S. G. Ghosh and S. D. Maharaj, "Noncommutative inspired black holes in regularized 4D Einstein-Gauss-Bonnet theory," *Physics of the Dark Universe*, vol. 31, p. 100793, Jan. 2021.

[85] E. Ayon-Beato, "New regular black hole solution from nonlinear electrodynamics," *Physics Letters B*, vol. 464, pp. 25–29, Oct. 1999.

[86] E. Ayen-Beato and A. Garcia, "Non-Singular Charged Black Hole Solution for Non-Linear Source," *General Relativity and Gravitation*, vol. 31, p. 629, May 1999.

[87] K. Jusufi, "Nonlinear magnetically charged black holes in 4D Einstein-Gauss-Bonnet gravity," *Annals of Physics*, vol. 421, p. 168285, Oct. 2020.

[88] S. G. Ghosh, D. V. Singh, R. Kumar, and S. D. Maharaj, "Phase transition of AdS black holes in 4D EGB gravity coupled to nonlinear electrodynamics," *Annals of Physics*, vol. 424, p. 168347, Jan. 2021.

[89] S. I. Kruglov, "Einstein -Gauss -Bonnet gravity with nonlinear electrodynamics," *Annals of Physics*, vol. 428, p. 168449, May 2021.

[90] A. Kumar, D. Baboolal, and S. G. Ghosh, "Nonsingular Black Holes in 4D Einstein–Gauss–Bonnet Gravity," *Universe*, vol. 8, p. 244, Apr. 2022.

[91] K. Yang, B.-M. Gu, S.-W. Wei, and Y.-X. Liu, "Born-Infeld black holes in 4D Einstein-Gauss-Bonnet gravity," *European Physical Journal C*, vol. 80, p. 662, July 2020.

[92] S. Habib Mazharimousavi and M. Halilsoy, "Einstein Yang Mills black hole solution in higher dimensions by the Wu Yang ansatz," *Physics Letters B*, vol. 659, pp. 471–475, Jan. 2008.

[93] S. Habib Mazharimousavi and M. Halilsoy, "Higher dimensional Yang Mills black holes in third order Lovelock gravity," *Physics Letters B*, vol. 665, pp. 125–130, July 2008.

[94] S. H. Mazharimousavi and M. Halilsoy, "Lovelock black holes with a power-Yang-Mills source," *Physics Letters B*, vol. 681, pp. 190–199, Oct. 2009.

[95] A. Biswas, "Black holes in 4D AdS Einstein Gauss Bonnet gravity with power: Yang Mills field," *General Relativity and Gravitation*, vol. 54, p. 161, Dec. 2022.

[96] H. Mark and S. Fernbach, *Properties of matter under unusual conditions.* 1969.

[97] P. G. S. Fernandes, "Charged black holes in AdS spaces in 4D Einstein Gauss-Bonnet gravity," *Physics Letters B*, vol. 805, p. 135468, June 2020.

[98] B. Carter, "Global Structure of the Kerr Family of Gravitational Fields," *Physical Review*, vol. 174, pp. 1559–1571, Oct. 1968.

[99] J. M. Bardeen, "Timelike and null geodesics in the Kerr metric," in *Les Houches Summer School of Theoretical Physics: Black Holes*, pp. 215–240, 1973.

[100] J. L. Synge, "The Escape of Photons from Gravitationally Intense Stars," *Mon. Not. Roy. Astron. Soc.*, vol. 131, no. 3, pp. 463–466, 1966.

[101] J. P. Luminet, "Image of a spherical black hole with thin accretion disk," *Astron. Astrophys.*, vol. 75, pp. 228–235, 1979.

[102] D. Arora, N. U. Molla, H. Chaudhary, U. Debnath, F. Atamurotov, and G. Mustafa, "Exploring tidal force effects and shadow constraints for Schwarzschild-like black hole in Starobinsky-Bel-Robinson gravity," *Eur. Phys. J. C*, vol. 83, p. 995, Nov. 2023.

[103] A. Yumoto, D. Nitta, T. Chiba, and N. Sugiyama, "Shadows of Multi-Black Holes: Analytic Exploration," *Phys. Rev. D*, vol. 86, p. 103001, 2012.

[104] T. Johannsen and D. Psaltis, "Testing the No-Hair Theorem with Observations of Black Holes in the Electromagnetic Spectrum," *Adv. Space Res.*, vol. 47, pp. 528–532, 2011.

[105] U. Papnoi, F. Atamurotov, S. G. Ghosh, and B. Ahmedov, "Shadow of five-dimensional rotating Myers-Perry black hole," *Phys. Rev. D*, vol. 90, no. 2, p. 024073, 2014.

[106] S. Vagnozzi and L. Visinelli, "Hunting for extra dimensions in the shadow of M87*," *Phys. Rev. D*, vol. 100, no. 2, p. 024020, 2019.

[107] R. Kumar Walia, S. G. Ghosh, and S. D. Maharaj, "Testing Rotating Regular Metrics with EHT Results of Sgr A*," *Astrophys. J.*, vol. 939, no. 2, p. 77, 2022.

[108] K. Hioki and K.-i. Maeda, "Measurement of the Kerr Spin Parameter by Observation of a Compact Object's Shadow," *Phys. Rev. D*, vol. 80, p. 024042, 2009.

[109] T. Johannsen, A. E. Broderick, P. M. Plewa, S. Chatzopoulos, S. S. Doeleman, F. Eisenhauer, V. L. Fish, R. Genzel, O. Gerhard, and M. D. Johnson, "Testing General Relativity with the Shadow Size of Sgr A*," *Phys. Rev. Lett.*, vol. 116, no. 3, p. 031101, 2016.

[110] C. Bambi, K. Freese, S. Vagnozzi, and L. Visinelli, "Testing the rotational nature of the supermassive object M87* from the circularity and size of its first image," *Phys. Rev. D*, vol. 100, no. 4, p. 044057, 2019.

[111] F. Atamurotov, A. Abdujabbarov, and B. Ahmedov, "Shadow of rotating non-Kerr black hole," *Phys. Rev. D*, vol. 88, no. 6, p. 064004, 2013.

[112] R. Kumar and S. G. Ghosh, "Black Hole Parameter Estimation from Its Shadow," *Astrophys. J.*, vol. 892, p. 78, 2020.

[113] M. Afrin and S. G. Ghosh, "Estimating the Cosmological Constant from Shadows of Kerr–de Sitter Black Holes," *Universe*, vol. 8, no. 1, p. 52, 2022.

[114] E. Ghorani, B. Puliçe, F. Atamurotov, J. Rayimbaev, A. Abdujabbarov, and D. Demir, "Probing geometric proca in metric-palatini gravity with black hole shadow and photon motion," *European Physical Journal C*, vol. 83, p. 318, Apr. 2023.

[115] A. A. Abdujabbarov, L. Rezzolla, and B. J. Ahmedov, "A coordinate-independent characterization of a black hole shadow," *Mon. Not. Roy. Astron. Soc.*, vol. 454, no. 3, pp. 2423–2435, 2015.

[116] K. Akiyama *et al.*, "First M87 Event Horizon Telescope Results. I. The Shadow of the Supermassive Black Hole," *Astrophys. J. Lett.*, vol. 875, p. L1, 2019.

[117] T. Johannsen and D. Psaltis, "Testing the No-Hair Theorem with Observations in the Electromagnetic Spectrum: II. Black-Hole Images," *Astrophys. J.*, vol. 718, pp. 446–454, 2010.

[118] H. Falcke, F. Melia, and E. Agol, "Viewing the shadow of the black hole at the galactic center," *Astrophys. J. Lett.*, vol. 528, p. L13, 2000.

[119] K. Akiyama *et al.*, "First M87 Event Horizon Telescope Results. II. Array and Instrumentation," *Astrophys. J. Lett.*, vol. 875, no. 1, p. L2, 2019.

[120] K. Akiyama *et al.*, "First M87 Event Horizon Telescope Results. III. Data Processing and Calibration," *Astrophys. J. Lett.*, vol. 875, no. 1, p. L3, 2019.

[121] K. Akiyama *et al.*, "First M87 Event Horizon Telescope Results. V. Physical Origin of the Asymmetric Ring," *Astrophys. J. Lett.*, vol. 875, no. 1, p. L5, 2019.

[122] K. Akiyama *et al.*, "First M87 Event Horizon Telescope Results. VI. The Shadow and Mass of the Central Black Hole," *Astrophys. J. Lett.*, vol. 875, no. 1, p. L6, 2019.

[123] K. Akiyama *et al.*, "First Sagittarius A* Event Horizon Telescope Results. I. The Shadow of the Supermassive Black Hole in the Center of the Milky Way," *Astrophys. J. Lett.*, vol. 930, no. 2, p. L12, 2022.

[124] K. Akiyama *et al.*, "First Sagittarius A* Event Horizon Telescope Results. IV. Variability, Morphology, and Black Hole Mass," *Astrophys. J. Lett.*, vol. 930, no. 2, p. L15, 2022.

[125] K. Akiyama *et al.*, "First Sagittarius A* Event Horizon Telescope Results. VI. Testing the Black Hole Metric," *Astrophys. J. Lett.*, vol. 930, no. 2, p. L17, 2022.

[126] V. Cardoso and P. Pani, "Testing the nature of dark compact objects: a status report," *Living Rev. Rel.*, vol. 22, no. 1, p. 4, 2019.

[127] M. Afrin, R. Kumar, and S. G. Ghosh, "Parameter estimation of hairy Kerr black holes from its shadow and constraints from M87*," *Mon. Not. Roy. Astron. Soc.*, vol. 504, pp. 5927–5940, 2021.

[128] J. Dexter, E. Agol, P. C. Fragile, and J. C. McKinney, "The Submillimeter Bump in Sgr A* from Relativistic MHD Simulations," *Astrophys. J.*, vol. 717, pp. 1092–1104, 2010.

[129] A. E. Broderick, V. L. Fish, S. S. Doeleman, and A. Loeb, "Evidence for Low Black Hole Spin and Physically Motivated Accretion Models from Millimeter VLBI Observations of Sagittarius A*," *Astrophys. J.*, vol. 735, p. 110, 2011.

[130] K. Akiyama *et al.*, "First Sagittarius A* Event Horizon Telescope Results. V. Testing Astrophysical Models of the Galactic Center Black Hole," *Astrophys. J. Lett.*, vol. 930, no. 2, p. L16, 2022.

[131] J. C. Faggert, F. Özel, and D. Psaltis, "The Unexpected Lack of Asymmetry in the Horizon-scale Image of Sagittarius A*," *Astrophys. J.*, vol. 981, no. 2, p. 209, 2025.